ESR AND RELATED EXPERIMENTS IN SPIN-POLARIZED ATOMIC HYDROGEN

ACADEMISCH PROEFSCHRIFT

ter verkrijging van de graad van
doctor in de Wiskunde en Natuurwetenschappen
aan de Universiteit te Amsterdam,
op gezag van de Rector Magnificus,
Dr. D.W. Bresters,
hoogleraar in de Faculteit
der Wiskunde en Natuurwetenschappen,
in het openbaar te verdedigen
in de Aula der Universiteit
(tijdelijk in de Lutherse Kerk,
ingang Singel 411, hoek Spui)
op woensdag 18 januari 1984 te 13.30 uur

door

Gerrit Hendrik van Yperen

geboren te Vlaardingen

1983
Offsetdrukkerij Kanters B.V.,
Alblasserdam

Promotor : Prof. Dr. I.F. Silvera

Het in dit proefschrift beschreven onderzoek werd uitgevoerd op het "Natuurkundig Laboratorium" van de Universiteit van Amsterdam.
Het onderzoek maakt deel uit van het onderzoekprogramma van de werkgemeenschap Vaste Stof van de "Stichting voor Fundamenteel Onderzoek der Materie" (FOM), en is als zodanig geldelijk gesteund door de "Nederlandse Organisatie voor Zuiver Wetenschappelijk Onderzoek" (ZWO).

Aan Rita

CONTENTS

I INTRODUCTION

1.1. Atomic hydrogen as an interesting quantum fluid 1
1.2. Experimental techniques used for the stabilization of $H\downarrow$ 9
1.3. Progress in the understanding of decay processes in $H\downarrow$ 13
1.4. Motivation of an ESR experiment on atomic hydrogen
Contents of this thesis 18
References of chapter 1 22

II CALCULATIONS OF THE NUCLEAR SPIN RELAXATION TIME IN SPIN-POLARIZED ATOMIC HYDROGEN

2.1. Introduction 24
2.2. The work of Lagendijk;
a description of the correlation function formalism 27
2.3. The work of Siggia and Ruckenstein 44
2.4. The work of Statt and Berlinsky 47
2.5. The work of Statt 50
2.6. The work of Ahn, v.d. Eijnde, Reuver, Verhaar, and Silvera 50
2.7. Summary and discussion
Comparison with experiments 51
References of chapter 2 57

III EXPERIMENTS WITH $H\downarrow$ ON ^{4}HE SURFACES AND ^{3}HE-^{4}HE MIXTURES

3.1. Introduction 58
3.2. Experimental details 64
3.3. Thermometry 66
3.4. Results 73
3.5. Discussion 79
References of chapter 3 84

IIII A STUDY OF DOUBLY POLARIZED ATOMIC HYDROGEN BY ELECTRON SPIN RESONANCE

4.1. Introduction 86
4.2. Theory of ESR transitions in $H\downarrow$ 88
4.3. Apparatus 96
4.4. ESR measurement techniques for $H\downarrow$ 107
4.5. Results 114
4.6. Suggestions for improvements 123
References of chapter 4 124

SUMMARY 126
SAMENVATTING 128
NAWOORD 130

CHAPTER I INTRODUCTION

1.1. Atomic hydrogen as an interesting quantum fluid

The subject of this thesis is the study of spin-polarized atomic hydrogen, commonly referred to as H↓. Hydrogen, the lightest and simplest of all elements, does not normally appear here on earth in the atomic state. Under normal conditions single H-atoms are chemically very reactive, so all hydrogen is strongly bound into chemical compounds, such as H_2O, CH_4, organical compounds etc. Two hydrogen atoms can also bind to form a H_2 molecule; we know H_2 as a gas that liquefies and solidifies at low temperatures like any other normal gas. Considered on the scale of the universe, H is the most abundant element; however the density is extremely low (~ 1 atom per m^3 in interstellar space). Recombination into H_2 molecules does take place but at an incredibly slow rate, since the required collisions are very scarce, and so the interstellar atomic hydrogen literally has a lifetime longer than that of the universe.

One would like to do laboratory scale experiments on samples of atomic hydrogen at useful densities, $\gtrsim 10^{13}$ atoms/cm^3. H_2 is easily dissociated into the atomic state, but under normal conditions such a gas of H-atoms would recombine in a time of order $\lesssim 1$ msec. It was necessary to conceive of conditions such that the recombination would be slowed down by many orders of magnitude. This stabilization of atomic hydrogen was realized for the first time a few years ago by Silvera and Walraven[1]. It involves a number of special experimental techniques which we shall describe in section 1.2 (polarization of electron spins by a strong magnetic field at low temperatures; cooling of gaseous H to liquid helium temperatures; selection of spin states and confinement of the sample by a strong magnetic field gradient; coating of the walls of the sample cell with a superfluid helium film). Before discussing any experimental details, we first want to introduce some notions which make atomic hydrogen so interesting from a theoretical point of view.

Spin-polarized atomic hydrogen is an extreme example of what is called a quantum fluid[2]. A quantum fluid is a fluid state of matter which displays quantum effects on a macroscopic scale. These quantum effects may have an equivalent in classical physics (e.g. phase separation in liquid ^{3}He-^{4}He mixtures) or may not have a classical analog (superfluidity in liquid ^{4}He, superconductivity). The pure quantum effects have a twofold origin: 1) the zero-point kinetic energy, and

2) the statistics (symmetry requirements on wavefunctions).

Macroscopic quantum behavior is found when one deals with particles of light mass and weak pair-interactions. The combination of these two properties makes the zero-point energy very important. The binding energy of a bound state of two particles is much less than the potential depth. In extreme cases there may not even exist a bound state: no stable He_2 pairs exist, although there is a manybody bound state, since helium forms a liquid. Helium does not solidify down to T = 0 K under its saturated vapor pressure. Spin-polarized atomic hydrogen is an even more extreme example in this context: it is predicted that the ground state remains a gas all the way down to T = 0 K[3]. As an example we see in fig. 1.1 two potentials: He-He and H-H for spin-polarized hydrogen. The attractive

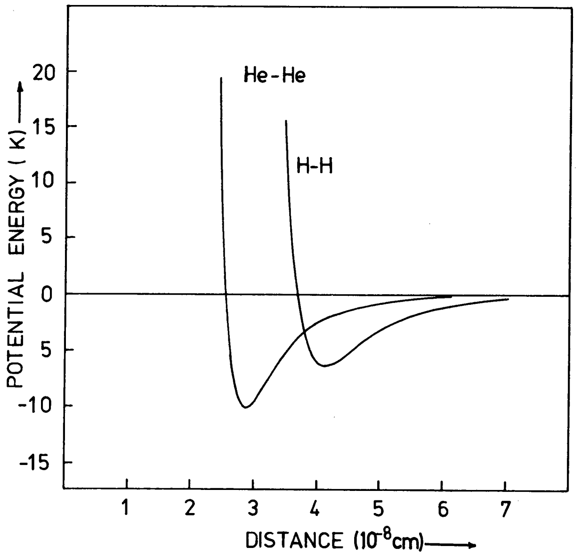

Fig. 1.1. Interatomic potential for spin-polarized atomic hydrogen, compared to the He-He potential.

part of the H-H potential is even weaker than that for He-He; this makes spin-polarized atomic hydrogen the weakest interacting system that exists. Potentials of this type can be fit to the Lennard-Jones form

$$V(r) = 4\varepsilon[(\sigma/r)^{12} - (\sigma/r)^{6}] \tag{1.1}$$

with well depth ε and hard core diameter σ. A quantitative parameter to measure the 'quantumness' of a substance is provided by the parameter

$$\eta \equiv \frac{\hbar^2}{2m\varepsilon\sigma} = (\Lambda/2\pi)^2 \tag{1.2}$$

with Λ the de Boer parameter. This parameter η comes from the de Boer Quantum Theorem of Corresponding States, in which the Hamiltonian $\mathcal{H} = T + W$ is rewritten in a scaled form

$$\mathcal{H} = \varepsilon(\eta t + w) \tag{1.3}$$

with both the kinetic energy t and potential energy w written in the scaled variable $r' = r/\sigma$. η clearly measures the relative importance of the kinetic energy to the potential energy. Some values for η are given in table 1.1, taken from ref. 2. The extreme behavior of H$\downarrow$ will be clear in this classification.

	ε(K)	σ(Å)	η
H$\downarrow$	6.46	3.69	0.547
D$\downarrow$	6.46	3.69	0.274
^{3}He	10.22	2.56	0.241
^{4}He	10.22	2.56	0.182
H_2	37.0	2.92	0.0763
D_2	37.0	2.92	0.0382
Ne	35.6	2.74	0.009
Ar	120.0	3.41	0.00087
Kr	163	3.65	0.00027
Xe	232	3.98	0.0001

Table 1.1.

Values of the Lennard-Jones parameters and the quantum parameter η *for* H$\downarrow$ *compared to various other substances. from ref. 2.*

The interatomic potential for 2 H-atoms is very accurately known from the calculations of Kolos and Wolniewicz[4,5,6]. In the electronic ground state two potentials arise: the $^1\Sigma_g^+$ potential for the case of an antisymmetric (singlet) electronic spin state, and the $^3\Sigma_u^+$ potential for symmetric (triplet) electronic spin states; see fig. 1.2A.

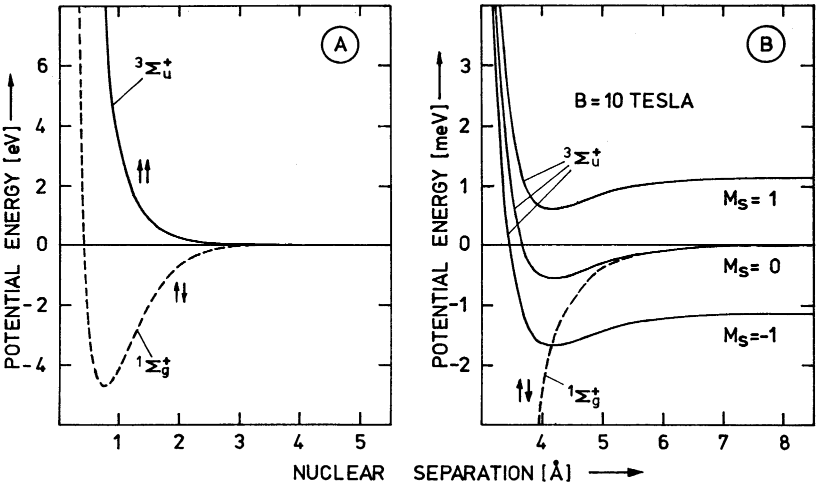

Fig. 1.2.A. Interatomic potentials for a pair of hydrogen atoms in the singlet (- - -) and triplet (———) state.

B. The triplet potential on an expanded scale. A magnetic field lifts the degeneracy and brings the $m_S = -1$ *branch below the singlet potential.*

The singlet potential has a very deep well of ∿ 4.75 eV which gives rise to the formation of the H_2 molecule in its ground state, and many vibrationally and rotationally excited states. The triplet potential however is the one that is given in fig. 1.1, on a widely expanded scale (1 eV is equivalent to ∿ 10^4K). Hydrogen atoms that have their electron spins polarized interact pairwise via the $^3\Sigma_u^+$ potential. The spin polarization is achieved by a strong magnetic field B, which lowers the triplet potential energy for both atoms in the $m_S = -\frac{1}{2}$ state by an amount $-\frac{1}{2}g_e\mu_B B$ (μ_B is the Bohr magneton, g_e the free electron g-factor); see fig. 1.2B. This magnetic field makes spin-polarized atomic hydrogen metastable, since for all internuclear distances $r \gtrsim 5Å$, corresponding to the average internuclear distance at low densities $\lesssim 10^{22}$ atoms/cm^3, the $m_S = -1$ triplet state is energetically more favorable than the singlet state. The material is only metastable, however, since any recombination would liberate an energy of 52000 K per pair of atoms, and the dynamics of collisions, when two atoms come to a very close distance, will be much more important than the static stability argument.

Full electronic spin polarization in H↓ does not exist for the following reason: the H-atom also contains a proton with a nuclear spin ½ and a magnetic moment. There is also a hyperfine interaction between electronic and nuclear spin. Diagonalization of the matrix of the Hamiltonian

$$\mathcal{H} = g_e \mu_B \vec{S}.\vec{B} - g_N \mu_N \vec{I}.\vec{B} + a\vec{I}.\vec{S} \qquad (1.4)$$

(g_e, g_N electronic resp. nuclear g-factor, μ_N nuclear magneton, a strength of hyperfine interaction) gives an energy level diagram with 4 levels (fig. 1.3). In high field the lowest two levels (a and b) have electron spin down, except for the fact that state a has a small admixture ε of electronic spin up state. ε is field dependent ($\propto B^{-1}$ for high fields; $\varepsilon \approx 2.5 \times 10^{-3}$ for 10 Tesla). A collection of H-atoms in states a and b is still called spin-polarized hydrogen, although the hyperfine interaction has disturbed the full electron spin polarization. As a consequence it turns out that for instance two atoms in the a-state interact via a mixture of triplet and singlet potentials:

$$V_{eff}^{(aa)} = V_T + \varepsilon^2 V_S \qquad (1.5)$$

Because of the smallness of ε^2 in high magnetic fields this hardly deviates from the pure triplet potential V_T, and certainly not in the classical accessible range of internuclear distances $r > \sigma$.

Quantum phenomena occur when the average distance between particles ($\propto n^{-1/3}$) becomes comparable to the size of the wave packets describing the quantummechanical motion of the particles: $\lambda = \sqrt{2\pi\hbar^2/mk_BT}$; λ is the thermal de Broglie wavelength. The equality occurs at

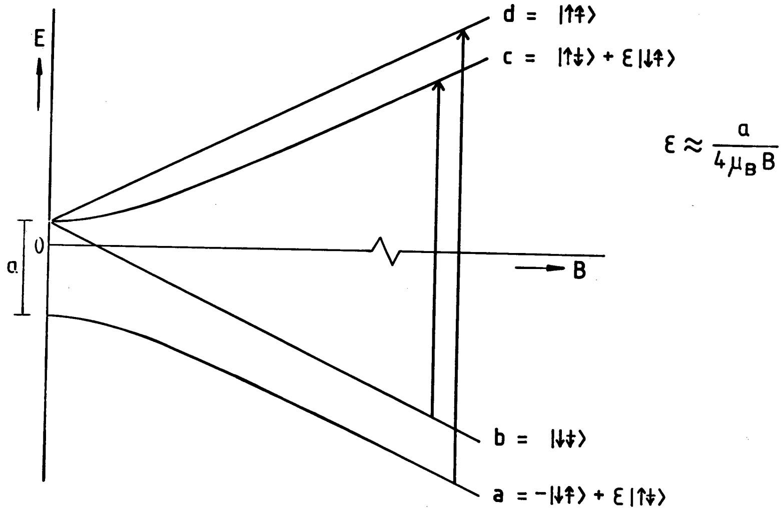

Fig. 1.3. Hyperfine states of the hydrogen atom in a strong magnetic field B. The allowed ESR transitions are shown by the arrows.

$T = 2\pi\hbar^2/(mk_B).n^{2/3}$. The most striking phenomenon that is predicted to occur in H↓ is Bose-Einstein Condensation (BEC). This originates directly from the statistics obeyed by boson particles. Below a critical temperature T_c, of the order of the above T, a macroscopic occupation of the (momentum-) ground state results. This will for instance show up dramatically in the equation of state. For a gas of non-interacting bosons the expression for T_c is

$$T_c = 3.31\,\frac{\hbar^2}{mk_B}\left(\frac{n}{g}\right)^{2/3} \tag{1.6}$$

with n the number density of particles with mass m; g is a spin degeneracy factor and k_B the Boltzmann constant. It is believed that superfluidity in liquid ^{4}He below the λ-transition (T = 2.17 K) is closely related to BEC. However, liquid helium is not an ideal gas, but instead a strongly interacting bose liquid of high density ($n \approx 2 \times 10^{22}$ /cm^3). Taking into account the interactions complicates the theory enormously. One result is that the fraction of particles in the $\vec{k} = 0$ state, which approaches 100 % for temperatures well below T_c in an ideal bose gas, is only ~ 10 % at T = 0 K in liquid ^{4}He. Only very recently this has been verified experimentally in an inelastic neutron scattering experiment[7]. (The experiment is not without criticism however[8].) Spin-polarized atomic hydrogen could have a number of advantages with respect to ^{4}He to study BEC: H↓ has a quantum parameter η which is 3 times larger, so it will resemble more the ideal bose gas. Since the state is gaseous, the density can be controlled externally, and the dependence of T_c on n could be verified. In particular one could work at very low T_c and low n to minimize the effect of interactions. An interesting aspect is also that BEC, which is not a condensation in real space, can be turned into a spatial localization in this special case of bosons carrying a magnetic moment, in an inhomogeneous magnetic field[9]. If H↓ becomes superfluid, it would be the first time to observe superfluidity in a gas.

Until now it has not been possible to suppress recombination into H_2 molecules sufficiently to create the combination of low temperature and high density H↓ needed to observe BEC (e.g. T_c = 100 mK, $n = 1.5 \times 10^{19}/\text{cm}^3$). Compared to the experiments described in this work 2 orders of magnitude are still missing. Considerable progress has been made in the years following the initial stabilization of H↓ in identifying the processes that limit the maximum attainable densities. These advances will be discussed in some detail in section 1.3. Apart from BEC there are also a number of other interesting experiments that can be performed in lower density H↓. The presence of both an electronic and a nuclear spin, and the associated magnetic moments, introduces many interesting phenomena as compared to the spinless ^{4}He. One can measure DC magnetization[10]; one can localize the sample in space by strong magnetic field gradients; magnetic resonance (both ESR and NMR) is possible; hydrodynamic waves can be studied[11]. Of interest is also deuterium (D↓)[12]. D is a fermion, and the exclusion of s-wave scattering in spin-polarized deuterium will have interesting consequences for the low temperature transport coefficients. D↓ is predicted to liquefy. It may also show properties analogous to ^{3}He liquid, where fermion pairing causes superfluidity at very low temperatures.

Apart from the fundamental properties which justify the study of H↓ in itself, there are a number of topics in physics to which the study of H↓ is closely related. A few examples of these topics, which can be regarded as applications of the cryogenic techniques used to stabilize H↓ are:

- The hydrogen MASER as a possible time and frequency standard, which could benefit from low temperature operation and the very reproducible behavior of superfluid He as coating of the walls of the sample chamber[13,14].
- The preparation of polarized proton samples consisting of pure H as targets for high energy proton scattering experiments; and the realization of an effective source of polarized protons to inject in accelerators.
- The preparation of polarized deuterium nuclei for increased efficiency in plasma fusion reactors[15].

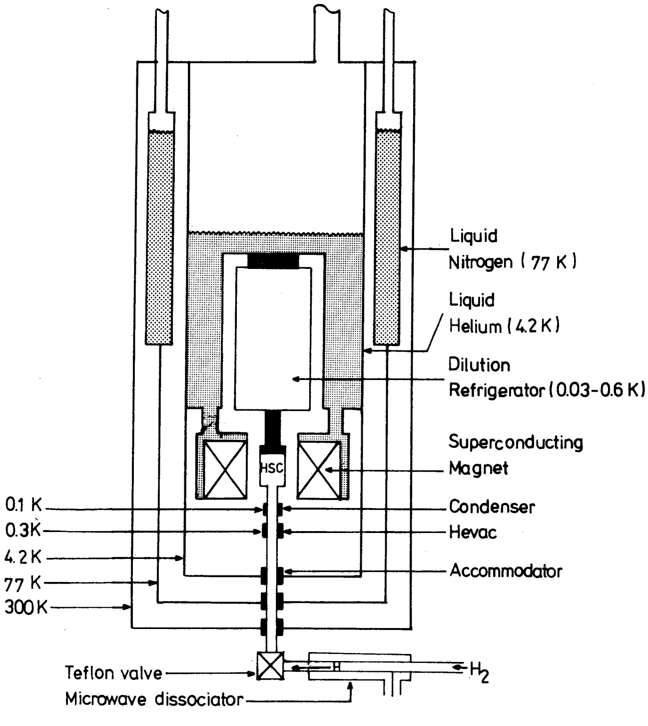

Fig. 1.4.

Diagram of H↓ *stabilization experiment in a* ^3He-^4He *dilution refrigerator*

1.2. *Experimental techniques used for the stabilisation of* H↓[1,16]

A schematic diagram of an H↓ stabilization experiment is given in fig. 1.4. H_2 at a pressure of ~ 1 Torr is dissociated in a room temperature, 2.45 GHz microwave discharge in a quartz tube. The atomic hydrogen can, at room temperature, easily be transported over some distance in tubes that are teflon coated. H atoms do not stick to teflon surfaces, and an atom can make an average of $\sim 2 \times 10^4$ collisions with the wall before it recombines. On metallic surfaces the H atoms stick and after the first wall collision the atom will almost certainly recombine. The gas is introduced in a cryostat in a teflon coated metal pipe, which has sections cooled to liquid N_2 (77 K) and liquid He (4.2 K) temperatures. By wall collisions with the teflon tube the atoms accommodate their thermal energy, and a low temperature gas of H atoms with a Maxwellian velocity distribution is obtained. A flux of $\sim 2 \times 10^{16}$ atoms/sec at $T \approx 8$ K has been observed[16]. The cold gas enters a magnetic field gradient, which serves to polarize the electronic spins. A force $\vec{F} = \mu \vec{\nabla} B$ (with μ the effective magnetic moment; in high field $\mu = \pm \frac{1}{2} g_e \mu_B$) pulls the atoms with spin down (↓, $m_S = -\frac{1}{2}$) towards the highest field region and repels the atoms with spin up. Somewhere in the lower field region the atoms with spin up either recombine, or relax their electron spin to the down state. The force of the magnetic field gradient keeps the spin down atoms effectively trapped in a potential well. A density distribution[9]

$$n(z) = n(0)\, e^{-\mu\, [\, B(z) - B(0)\,]\, / k_B T} \qquad (1.7)$$

is established for a one-dimensional field profile B(z). This is called magnetic confinement of the sample. There is a finite probability for a particle to escape from the potential well; however the timeconstant for this exponential decay process can be made arbitrarily long by making $[\, B(0) - B(z)\,] / T$ large. Because of the Maxwell law $\mathrm{div}\, \vec{B} = 0$ it is not possible to make a steady state field geometry which confines the H↓ in all directions, so the sample must be enclosed by cell walls. At temperatures of 4.2 K and below teflon has completely lost its non-sticking property, so large surface coverages of H atoms would build up and recombination would be fast. The best conceivable surface coating at low temperatures is a film of (superfluid) helium. The ^{4}He surface was known to present a very weak effective interaction potential[17] to a single H atom. It is now proved experimentally that this potential supports just one bound state with a binding energy of ~ 0.9 K. Only for temperatures $\leqslant 0.9$ K surface adsorption effects become important.

The superfluid ^{4}He film required introduces a serious cryogenic problem: the film tends to creep to the warmer parts of the open system, vaporizes and recondenses in the cold end. This heat pipe principle is a very efficient way of transporting heat, and a large heat load is put on the refrigerator that is supposed to cool the sample cell to millikelvin temperatures. To solve this problem a 'film burning' device was incorporated, indicated as HEVAC in fig. 1.5. The idea is to heat the inner tube near its interception so that a temperature gradient is

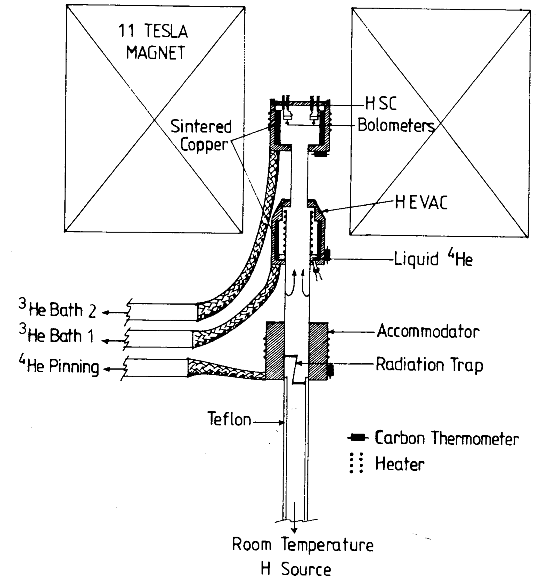

Fig. 1.5. Low temperature section of H↓ *stabilization experiment in a ^{3}He evaporation cryostat. Important detail is the HEVAC (Helium Vapor Compressor).*

set up in the section of tube just below the heater. Somewhere along this gradient the helium film vaporizes, but the vapors recondense on the inside of the outer tube, which is cooled by a refrigerator independent of the one that cools the sample cell. This way the heat load of the fluxing vapors will not limit the desired low temperature of the sample cell. The fluxing vapors are supposed to remain outside the central tube, where the H gas is fed in. However, it was found that one could just as well let the helium vaporize somewhere halfway the natural temperature gradient between the HEVAC and the accommodator (= 4.2 K thermal pinning), and have it recondense in the cold section of the inner tube of the HEVAC. This way it still removes the heat load from the cell, but now the fluxing vapors are in the fill line. This even proved to be useful, since the 4 times more massive ^{4}He atoms drag along the H atoms, and the whole system acts as a small diffusion pump. It compresses the H gas into the cell. The name HEVAC stands for HElium VApor Compressor. It helps to confine the sample to the cell in case magnetic compression alone is not sufficient. A reservoir is still present in the HEVAC to store a bulk amount of ^{4}He, to prevent droplets from falling into the warm parts of the H fill line.

Between the parts that are He coated and the parts where the warm teflon surface is active, there will be parts of exposed metal where immediate recombination occurs. However, molecular hydrogen itself turns out to provide a useful coating for these intermediate temperature regions ($\sim$4.2-2 K). H on H_2 has a bound state with binding energy 35.8 K[18]. This means that the H atoms do not immediately stick to this surface, but the recombination is limited to an acceptable level. Yet there appears to be a loss in flux of about two orders of magnitude when comparing the measured flux from the accommodator to the measured flux of stabilized atoms into the cell, under favorable conditions. It turns out to be important to keep the transition section between the 4.2 K accommodator and the part where the He film is present, as short as possible, together with a cold ($T \lesssim 0.6$ K) HEVAC. These cryogenic requirements are rather difficult to achieve simultaneously. In a later stage a second 'condenser', also called thermal platform, was added with the purpose of condensing possible residual ^{4}He vapors onto a baffle, cooled independently from the HEVAC. This allows the sample cell to cool to temperatures $\lesssim 30$ mK with a superfluid film present.

The experiments described in this thesis were carried out in two ^3He-^4He dilution refrigerators, manufactured by Oxford Instruments. These are high cooling power (300 resp. 500 μW at mixing chamber temperature 100 mK) dilution refrigerators, equipped with sintered silver heat exchangers and capable of maintaining continuously mixing chamber temperatures of 6.5 mK and 4.5 mK respectively. The dewars of the all metal cryostats are completely demountable, while the dilution refrigerator insert remains in position. The lower parts of the cryostat have no liquid N_2 and ^4He, but contain conduction cooled radiation shields instead. These features make the experimental working space in the IVC (Inner Vacuum Chamber) rather easily accessible, and it suits very well the 'bottom loading' geometry for the H used in Amsterdam. The sample cell is connected to the mixing chamber of the dilution unit; the HEVAC is connected to the continuous heat exchanger and the condenser is connected to the dilute stream in between the continuous and the first discrete heat exchanger. This requires heat transport over rather long distances (~ 50 cm) via heavy copper links.

The magnetic fields were produced by two superconducting NbTi coils with persistent mode switches, manufactured by Thor Cryogenics. The general purpose coil is a simple solenoid which provides a max. 12 Tesla field with no particular homogeneity properties. The field profile is quadratic along the z-axis over distances up to ~ 3 cm from the center. The maximum gradient is 2 T/cm. The free bore is 25 mm diameter. For the ESR experiment described in chapter 4 a larger coil, offering 1 part in 10^5 homogeneity over a 1 cm length was used. The free bore of this magnet is 35 mm and the maximum field is 7.5 T. Both coils are mounted in their own helium cans, which are connected to the main helium reservoir of the cryostat. The cans of these magnets can be cooled to 2.17 K by means of a so called λ-point refrigerator[19]. This nice feature allows one to cool the magnet to the λ-point without having to pump down the helium bath of the cryostat.

1.3. Progress in the understanding of decay processes in stabilized H↓

Following the initial succes of the stabilization of atomic hydrogen[1] (and deuterium) a number of experiments have been performed with the aim of increasing the maximum sample density and/or lowering the temperature, with the ultimate goal of observing Bose-Einstein condensation. Considerable progress has been made in this period in the understanding of the decay processes that limit the maximum density. We will now give a brief historical overview of these advances.

In the original stabilization experiment[1] no measurable decay of H↓ was observed for relatively low densities $\sim 10^{14}/\mathrm{cm}^3$ in 7 Tesla and at T = 270 mK during ~ 9 minutes. The use of a 'trigger bolometer' demonstrated the suppression of recombination by the superfluid ^{4}He wall coating. Magnetic confinement was demonstrated by comparing the lifetime of a sample in zero magnetic field. Even in zero field no recombination was observed; the rapid (τ = 1.5 sec) exponential decay was caused by the flow of atoms (thermal leakage) out of the sample cell, retarded by the compression effect of the HEVAC.

A quantitative understanding of the concepts of magnetic compression, HEVAC compression and thermal leakage was obtained from a detailed study[20] of density as function of magnetic field, temperature and filling flux. From the fact that all measurements could well be described with a density distribution

$$n(B) = n(B_0)\ \exp\left[-\mu(B_0-B)/k_BT\right] \qquad (1.8)$$

the conclusion was drawn that H↓ is indeed a gas. Thermal leakage gives rise to a pure exponential decay. At higher densities, up to $\sim 10^{16}/\mathrm{cm}^3$ deviations from pure exponential decay were observed, in the sense of faster initial decay rates. It was not clear whether this should be attributed to recombination or whether it resulted from imperfections in the simple model assumed (a uniform temperature in eq. 1.8) or uncertainties in the density calibration. Observations were reported on low density deuterium. The maximum density was much lower than that for hydrogen. This suggested that at least for D surface recombination became important (the adsorption energy of D was predicted to be larger than that of H[17], thus a higher surface coverage occurs at the same temperature). Magnetic compression should be the same for H and D.

Similar observations were also made at MIT[21]. They used a system with only magnetic compression (no HEVAC) and a more uniform temperature throughout the density distribution. They observed a non identified recombination process.

Silvera and Walraven[22] made a detailed study of the decay times of D↓ samples on ^{4}He surfaces. They assumed a rate equation

$$\frac{dN}{dt} = - V \frac{n_g}{\tau} - V K_V n_g^3 - A K_s n_s^2 \tag{1.9}$$

with $N = Vn_g + An_s$ the total number of particles, distributed among a gas phase with density n_g in a volume V, and an adsorbed surface phase with density n_s on a surface area A. K_V and K_s are rate constants for 3 body (gas phase) and 2 body collision recombination processes. The first term with time constant τ from thermal leakage was known and could be neglected at high field. The second term was unknown but was neglected as well since the decay could be well described by the equation

$$\frac{dN}{dt} = - K_s^{eff} N^2 \tag{1.10}$$

This rate equation was expected to hold when n_s and n_g are proportional; such a proportionality is indeed expected for the low density limit of the adsorption isotherm

$$n_s = n_g \lambda \exp (\varepsilon_a/k_BT) \tag{1.11}$$

(λ is the thermal de Broglie wavelength $\lambda = (2\pi\hbar^2/mk_BT)^{\frac{1}{2}}$, ε_a the adsorption energy). This simple adsorption isotherm follows from the equation of the chemical potential of a 2-D and a 3-D gas. K_s^{eff}, an effective surface recombination rate, is defined by

$$K_s^{eff} \equiv K_s \frac{A}{V^2} \lambda^2 \exp (2\varepsilon_a/k_BT) \tag{1.12}$$

From the dependence of the measured K_s^{eff} on temperature T the adsorption energy could be determined. A large value $\varepsilon_a/k_B = 2.5\pm0.4$ K was found. (This value was later corrected to 2.6±0.4 K because it was realized that one expects a $\sqrt{T}$ temperature dependence for K_s, rather than a temperature independent K_s). Because of the strong exponential temperature dependence of the ratio n_s/n_g (1.11), the surface density grows rapidly below a certain temperature, which is proportional to ε_a. Also the pre-exponential factor, the intrinsic rate constant K_s became known, and it was realized that the present surface coverages were limited to values much lower than those predicted to be stable by the static stability arguments. Some speculative scalings were done for the corresponding situation for H. They indicate that the maximum surface coverage will be much lower than the value which is required to observe Bose-Einstein condensation in the gas[23].

The corresponding measurements for H↓ on ^{4}He required some modification of the cell used in the previous measurement. To make the thermal leakage term in (1.9) negligible compared to the surface recombination term one would either have to go to lower temperatures ($T \lesssim 0.3$ K, inaccessible with the ^{3}He evaporation refrigerator used at that time) or improve upon the magnetic compression by increasing $B(0) - B(z)$. This could be done by moving the HEVAC to a lower field region. Matthey, Walraven and Silvera[24] also introduced the use of a sensitive in-situ capacitive pressure gauge as a non-destructive measuring technique. This way they could measure continuously the comparatively slow decay of H↓ on ^{4}He, which was an enormous time saving over the destructive trigger bolometer technique used so far. The very good resolution with which the decay curves could be measured allowed a fit to be made to the solution of a rate equation like (1.9) with both the thermal leakage and the second order recombination taken into account. A moderate improvement in the magnetic compression, only to avoid the situation that the decay rate due to leakage is completely dominating the effect of recombination, was sufficient to enable a determination of K_s^{eff}. From the temperature dependence again ε_a for H↓ on ^{4}He could be determined, which was found to be $\varepsilon_a/k_B = 0.89\pm0.07$ K.

At the same time measurements by Morrow, Jochemsen, Berlinsky and

Hardy[25] at UBC had also provided a value for ε_a for H on ^{4}He. They used a completely different technique: they performed magnetic resonance (NMR) on low density ($\lesssim 5\times10^{12}/\text{cm}^3$) samples of H in zero field. ε_a was determined by two independent methods: one uses the NMR signal strength as a measure for the density; the second order decay is measured and analyzed as above. The other method depends on a very accurate measurement of the NMR transition frequency, which is influenced by a wall shift. The wall shift depends on τ_s/τ_B, the average time an H particle resides on the surface (τ_s) or in the gas (τ_B). Because $\tau_s/\tau_B = N_s/N_B$, the wall shift depends on the adsorption isotherm:

$$\frac{\tau_s}{\tau_B} = \frac{A}{V}\,\lambda\,\exp\,(\varepsilon_a/k_BT) \tag{1.13}$$

The result $\varepsilon_a/k_B = 1.15\pm0.05$ K is somewhat larger than that of ref. 24, a discrepancy which is still not solved.

The next experiment was to measure ε_a of H↓ on ^{3}He surfaces, since ^{3}He was predicted theoretically to provide a lower binding energy[17]. Some preliminary results were already reported[22,24] but it was necessary to perform an experiment in a ^{3}He-^{4}He dilution refrigerator to obtain temperatures < 0.3 K, to minimize the effect of the higher vapor pressure of ^{3}He. The experiment[26] is described in chapter 3 of this thesis. Pure ^{3}He surface coatings could not be used (apparently the superfluid properties of ^{4}He films were essential for a good surface coating in the HEVAC and cell regions) but instead mixtures of ^{3}He-^{4}He were used. These mixtures phase separate at low temperatures, with ^{3}He floating on top of the film in at least a few monolayers. This surface is believed to be almost identical to a thick pure ^{3}He film. ε_a/k_B was found to be 0.34 ± 0.03 K, indeed better than for H↓ on ^{4}He, but not low enough to realize the desired high gas densities. Due to a low filling flux problem no increases could be recorded in the maximum steady state density. The value of the binding energy can be compared to the result obtained at UBC[27] for H (in zero field) on pure ^{3}He in a closed cell: $\varepsilon_a/k_B = 0.42\ 0.05$ K ; the agreement is reasonable.

A paper by Statt and Berlinsky[28] points out the important consequences of the fact that H↓ consists of atoms in two hyperfine states $a = -|{\downarrow}{\Uparrow}\rangle + \varepsilon|{\uparrow}{\Downarrow}\rangle$ and $b = |{\downarrow}{\Downarrow}\rangle$. Recombination, a transition to the singlet $({\downarrow}{\uparrow})$ molecular state can only occur in collisions between two atoms when at least one atom is in the (admixed) a-state. Recombination in a-a and a-b collisions purges the sample from the a-state, leaving a gas of pure b-state atoms. This would be stable against 2 body recombination, if not however a nuclear relaxation process would allow transitions from the b- to the a-state. Statt and Berlinsky calculated the relaxation rate for dipole-dipole interaction in the gas phase, and found a long relaxation time: of order hours for $n = 10^{16}/\mathrm{cm}^3$ at B = 10 T. This long time scale would determine the decay of a pure b-state sample. The process, originally suggested by W.N. Hardy, is called relaxation bottlenecked recombination[28]; it should allow very high densities of H (now $H{\downarrow}{\Downarrow}$, double polarized hydrogen) to be prepared. Van Yperen et al.[26] carefully studied decay of $H{\downarrow}$ on ^{4}He over long periods and at low temperatures to see the effects of depletion of the a-state and change of the decay time constant to a very long value, but with a negative result. Apparently some other fast nuclear spin relaxation process was overriding the very slow process calculated for bulk (3-D gas) dipolar relaxation. The same process for the adsorbed (2-D gas) was very soon calculated[29]; it could not explain the rapid relaxation. Measurements by Cline, Greytak and Kleppner[30] demonstrated for the first time that long nuclear spin relaxation times do indeed exist; they measured a value which is in agreement with theory[28]. However, at $T \lesssim 250$ mK they observed an extra relaxation process, which they attributed to surface relaxation. Measurements by Sprik et al.[31] in a cell with large surface area to volume ratio reveal clearly both bulk- and surface relaxation. Surface relaxation appears to be ~ 50 times faster than predicted by theory. They also show that the previously found rapid relaxation is caused by macroscopic magnetic impurities in the cell walls. This cell is prepared very clean; yet two processes can be distinguished: intrinsic relaxation by 2 body (H-H) collisions ($\propto n^2$) and impurity relaxation by collision of one H atom with a fixed impurity at the wall ($\propto n$). The latter could be suppressed by screening them with a film of helium of increasing thickness. Presumably all previous experiments have been carried out in 'dirty' cells with rapid relaxation, such that the population of the a- and b-level was always equal. No surface relaxation was observed for H↓↑ on ^{3}He-^{4}He mixtures; this is ascribed to the theoretically predicted anisotropy of the surface relaxation with respect to the orientation of the surface relative to the magnetic field[29]. The surface relaxation rate is zero when the field is perpendicular to the surface, but the effect can easily be averaged out by surface roughness. Superfluid ^{4}He films follow the roughness of the underlying substrate, but bulk amounts of the normal liquid ^{3}He can provide an ideally flat interface.

The maximum density observed so far with these techniques, making use of slow nuclear relaxation, is $n \approx 3 \times 10^{17}/\mathrm{cm}^3$ for H on ^{3}He-^{4}He. Our understanding of the processes and knowledge of their numbers have shown that it is not possible to achieve the high densities needed to observe Bose-Einstein condensation in a steady state situation where the incoming flux of atoms balances the loss by recombination, without having to turn to unrealistically high values for magnetic field or input flux. To overcome this problem, a number of compression experiments are now being carried out, in which a volume filled with H↓ is compressed to densities much higher than those allowed in steady state. Possibly BEC can be studied in the transient behavior after (or during) the compression, on a timescale of seconds.

1.4. Motivation of an ESR experiment on atomic hydrogen
Contents of this thesis

It can easily be shown that in high magnetic field two (magnetic dipole) transitions between the spin states (fig. 1.3) are allowed in which an electron spin is flipped: a → d and b → c. If we neglect the small mixing parameter ε these are pure ESR transitions; they can be induced in the standard magnetic resonance configuration: a small field, perpendicular to the main field and oscillating at frequency $\omega \approx \gamma_e B$. The frequency will be rather high, since the fields used for stabilizing H↓ are high: typically 160 GHz for $B \approx 6$ T. The two transitions a → d and b → c are separated by 1.420 GHz and they should be resolved easily in an experiment. The transition rates are proportional to the difference in population of the upper and lower level. Since the upper levels are not populated in H↓, the relative intensity of the a → d and b → c transition is a direct measure for the ratio of the populations n_a and n_b. (The nuclear spin transition b → a (NMR) at much lower frequencies around 1 GHz can also be studied, but provides only the population difference $n_b - n_a$). ESR is in principle a destructive measurement technique: atoms in states c and d, with electron spin up, will rapidly recombine or will be ejected from the sample cell by the field gradient. It is possible however, with a sensitive detector, to perform ESR at such a low power level ($\sim 10^{-8}$ W) that the loss of sample by ESR measurement is smaller than that of any of the decay processes under study.

Some advantages and special features of the proposed ESR experiment are:

- The population of the hyperfine levels a and b can be measured directly; this allows a direct 'microscopic' study of the recombination and relaxation processes, e.g. the verification of the above mentioned process of relaxation bottlenecked recombination and the measurement of the rate constants K_{aa} and K_{ab} for surface recombination in a-a and a-b collisions.
- It is a technique that measures density; the sensitivity does not fall at low sample temperatures, as is the case with a pressure gauge detector. Combined measurements of pressure and density can give information on the temperature of the gas by application of the ideal gas law $p = nk_BT$.
- In an inhomogeneous magnetic field the ESR lineshape is determined by both the field profile B(z) and the density profile $n_i(z)$ ($i = a,b$). For a known field profile, under certain circumstances the density distribution can be reconstructed from a measured lineshape. This could have an important application in the detection of possible Bose-Einstein condensation in an inhomogeneous magnetic field: the transition is accompanied by a change in the density profile[9,32].
- ESR is very well suited for the study of spin-polarized deuterium (D↓). Deuterium has a nuclear spin I = 1; consequently

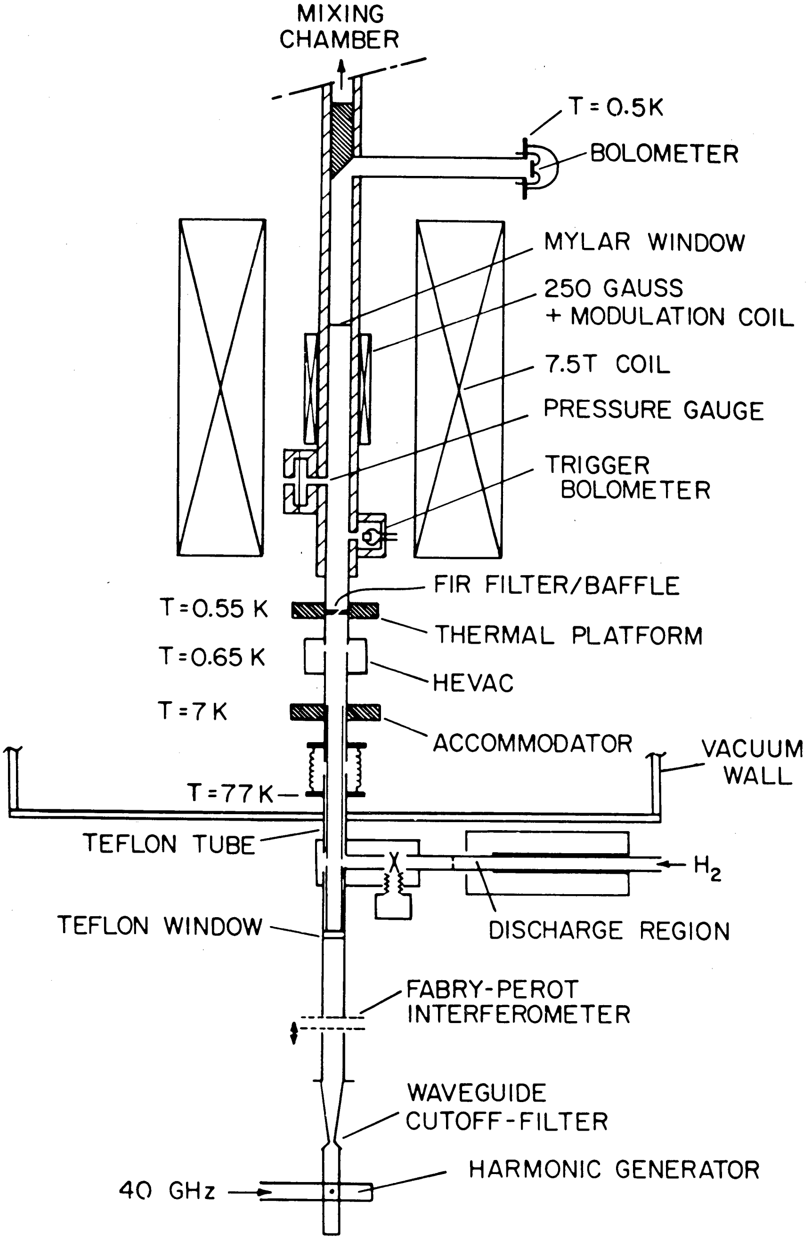

Fig. 1.6. Schematic diagram of ESR experiment on atomic hydrogen.

the hyperfine level diagram is more complicated: D↓ consists of atoms in 3 states. ESR again provides the population of these 3 levels. It can also easily distinguish between H and D in a mixture of the two, because of the different hyperfine splitting.

An ESR experiment on H↓ has been carried out[33]. The technique is basically simple, and is briefly summarized in fig. 1.6. Absorption of microwave radiation is measured in a single pass transmission through the H↓ sample. The fill line for the H gas also serves as a light pipe to transmit the microwave radiation. This experiment is described extensively in chapter 4 of this thesis. The very important role of the nuclear spin relaxation process (b → a) has been discussed already. The theory for calculation of the rate of this process is the subject of chapter 2. Both surface and volume relaxation are calculated in some detail, and an overview of the existing literature is given. In chapter 3 an experiment is described in which the adsorption energy ε_a of H↓ on ^{3}He-^{4}He mixtures is measured. Chapters 3 and 4 represent the main part of the experimental work carried out for my thesis. Apart from this I have participated in two other experiments on spin-polarized atomic hydrogen: an experiment in which ballistic heat pulses in low density H↓ at T = 200 mK were generated and detected (a precursor to soundwave-like experiments)[11], and an experiment in which nuclear spin relaxation times in H↓ were measured (bulk and surface dipolar relaxation, impurity relaxation, both on ^{4}He and ^{3}He-^{4}He)[31]. This work will not explicitly be discussed in my thesis.

References of chapter 1

1. I.F. Silvera and J.T.M. Walraven, Phys. Rev. Lett. 44, 164 (1980).
2. L.H. Nosanow, Journal de Physique, Colloq. 41, C7-1 (1980).
3. C.E. Hecht, Physica 25, 1159 (1959).
4. W. Kolos and L. Wolniewicz, J. Chem. Phys. 43, 2429 (1965).
5. W. Kolos and L. Wolniewicz, Chem. Phys. Lett. 24, 457 (1974).
6. W. Kolos and L. Wolniewicz, J. Mol. Spectr. 54, 303 (1975).
7. V.F. Sears, E.C. Svensson, P. Martel and A.D.B. Woods, Phys. Rev. Lett. 49, 279 (1982).
8. F.W. Wirth, D.A. Ewen, and R.B. Hallock, Phys. Rev. B27, 5530 (1983).
9. J.T.M. Walraven and I.F. Silvera, Phys. Rev. Lett. 44, 168 (1980).
10. J.T.M. Walraven and I.F. Silvera, Physica 107B, 517 (1981).
11. K.T. Salonen, I.F. Silvera, J.T.M. Walraven, and G.H. van Yperen, Phys. Rev. B25, 6002 (1982).
12. I.F. Silvera and J.T.M. Walraven, Phys. Rev. Lett. 45, 1268 (1980).
13. S.B. Crampton, W.D. Phillips, D. Kleppner, Bull. Am. Phys. Soc. 23, 86 (1978).
14. W.N. Hardy, M. Morrow, R. Jochemsen and A.J. Berlinsky, Physica B+C 109 & 110, 1964 (1982).
15. R.M. Kulsrud, H.P. Furth, E.J. Valeo and M. Goldhaber, Phys. Rev. Lett. 49, 1248 (1982).
16. J.T.M. Walraven and I.F. Silvera, Rev. Sci. Instr. 53, 1167 (1982).
17. I.B. Mantz and D.O. Edwards, Phys. Rev. B20, 4518 (1979); R.A. Guyer and M.D. Miller, Phys. Rev. Lett. 42, 1754 (1979).
18. S.B. Crampton, J.J. Krupczak and S.P. Souza, Phys. Rev. B25, 4383 (1982).
19. M.N. Biltcliffe, P.E. Hanley, J.B. McKinnon, and P. Roubeau, Cryogenics 12, 44 (1972).
20. J.T.M. Walraven, I.F. Silvera, and A.P.M. Matthey, Phys. Rev. Lett. 45, 449 (1980).
21. R.W. Cline, D.A. Smith, T.J. Greytak and D. Kleppner, Phys. Rev. Lett. 45, 2117 (1980).
22. I.F. Silvera and J.T.M. Walraven, Phys. Rev. Lett. 45, 1268 (1980).
23. I.F. Silvera and V.V. Goldman, Phys. Rev. Lett. 45, 915 (1980).

24. A.P.M. Matthey, J.T.M. Walraven, and I.F. Silvera, Phys. Rev. Lett. 46, 668 (1981).
25. M. Morrow, R. Jochemsen, A.J. Berlinsky and W.N. Hardy, Phys. Rev. Lett. 46, 195 (1981); 47, 455 (1981).
26. G.H. van Yperen, A.P.M. Matthey, J.T.M. Walraven and I.F. Silvera, Phys. Rev. Lett. 47, 800 (1981).
27. R. Jochemsen, M. Morrow, A.J. Berlinsky, and W.N. Hardy, Phys. Rev. Lett. 47, 852 (1981).
28. B.W. Statt and A.J. Berlinsky, Phys. Rev. Lett. 45, 2105 (1980).
29. A. Lagendijk, Phys. Rev. B25, 2054 (1982).
30. R.W. Cline, T.J. Greytak, and D. Kleppner, Phys. Rev. Lett. 47, 1195 (1981).
31. R. Sprik, J.T.M. Walraven, G.H. van Yperen and I.F. Silvera, Phys. Rev. Lett. 49, 153 (1982).
32. V.V. Goldman, I.F. Silvera and A.J. Leggett, Phys. Rev. B24, 2870 (1981).
33. G.H. van Yperen, I.F. Silvera, J.T.M. Walraven, J. Berkhout and J.G. Brisson, Phys. Rev. Lett. 50, 53 (1983).

CHAPTER II CALCULATIONS OF THE NUCLEAR SPIN RELAXATION TIME IN SPIN-POLARIZED ATOMIC HYDROGEN

2.1. Introduction

In the earlier experiments on electron spin-polarized atomic hydrogen no explicit attention was given to the fact that atoms can be in either of the two hyperfine states $a = -|\downarrow\Uparrow\rangle + \varepsilon|\uparrow\Downarrow\rangle$ and $b = |\downarrow\Downarrow\rangle$. The presence of a nuclear spin and hyperfine coupling, which are responsible for the splitting between the two levels (~54 mK in 10 Tesla) complicate the situation, and make atomic hydrogen an even more interesting system than what it already is as a weakly interacting Bose fluid. Siggia and Ruckenstein[1,2] have published two papers in which they consider Bose condensation in two separate hyperfine components. Magnetic resonance experiments NMR and/or ESR would be the appropriate tool for studying these very special effects. However, the densities of $H\downarrow$ and temperatures necessary to observe these effects are at the moment still quite remote. On the other hand, the existence of $H\downarrow$ in two states a and b does have important consequences even in basic experiments where recombination is studied. It was realized early that the hyperfine interaction is responsible for recombination to the molecular state. In a simple picture proposed by Silvera[3] the rate of recombination is proportional to the square of a matrix element, $|\langle f|\mathcal{H}_{int}|i\rangle|^2$, where $|i\rangle$ and $|f\rangle$ are the initial 2-atom states and the molecular state respectively, and the interaction Hamiltonian given by

$$\mathcal{H}_{int} = \tfrac{1}{2} \sum_{ij}{}' V(r_{ij}) + \tfrac{1}{2} \sum_{ij}{}' J(r_{ij}) \vec{S}_i . \vec{S}_j$$

The states $|i\rangle$ and $|f\rangle$ are factorized in spatial and (electronic) spin parts. For an initial state $|i\rangle = |b\rangle|b\rangle$ the atoms interact via the pure triplet interaction, and the projection of the triplet spin state onto the molecular singlet state is zero. This means that collisions between two b-state atoms cannot give rise to recombination, but collisions where at least one a-state atom is involved, can. The hyperfine interaction introduces a small admixture ε of electronic spin up in the a-state, which mixes some singlet character in the 2-atom initial states. The exchange part $\vec{S}_i . \vec{S}_j$ of the above interaction conserves total spin angular momentum ($\vec{S}_1 \cdot \vec{S}_2 = \frac{1}{2} [(\vec{S}_1 + \vec{S}_2)^2 - S_1^2 - S_2^2]$) so it is indeed sufficient to project the initial states directly onto the final state. This model has been put on firm grounds by Greben, Thomas and Berlinsky[4] for the case of 3 body collisions with ^{4}He as a third body; the same qualitative results are believed to hold for surface recombination. It thus seems that a sample, prepared to consist of atoms in the pure b-state only, would not recombine ! However, during collisions a suitable spin-dependent interaction can cause transitions between the b- and a-level; in the absence of recombination these collisions would bring the population of the b- and a-levels in thermal equilibrium. This is a nuclear spin relaxation process (T_1) since, under neglect of the mixing parameter ε , the transition from $b = |\downarrow\Downarrow\rangle$ to $a \approx -|\downarrow\Uparrow\rangle$ involves a nuclear spin flip only. The timescale for decay of a sample initially in the b-state is thus set by a nuclear T_1; this time can be much longer than the characteristic time for recombination in b-a collisions. These ideas were first exposed in an article by Statt and Berlinsky[5] who showed that T_1 could be of order several hours for conditions that were at that time already being realized in experiments. They gave a detailed calculation of the spin-lattice relaxation time, the 'lattice' being a gas of hydrogen atoms moving in free space and interacting via a realistic potential. The reason that this very long T_1 did not manifest itself in the first experiments by very long sample lifetimes is twofold: first part of the H atoms are bound to the surface of the helium film covering the cell walls, where they move as a two dimensional gas. Since the 'lattice' motions in 2-D are different from 3-D, the surface relaxation rate could well be faster than the 3-D (bulk) rate. Since there is a constant rapid exchange of particles between the surface and the gas, this surface rate translates into an effective bulk rate, which is observed. Second, collisions between H atoms and ferro- and paramagnetic impurities at the surface can provide an additional relaxation mechanism which can shortcircuit the intrinsic process. This situation is analogous to studies of nuclear relaxation in ^{3}He gas[6,7], where great care in preparing clean sample cells had to be taken, and where also bulk and surface effects could be separated.

Subsequently a number of papers have appeared that calculate the surface ralaxation rate in H↓ . The purpose of the present chapter of this thesis is to give a short review of the publications that have appeared so far on 3-D and/or 2-D nuclear relaxation in H↓, and to supply some introductory material to these papers, some of which are written very concise and are therefore difficult to understand without the necessary background knowledge. Although the results are to a large extent equivalent, the correspondence between the various papers is not so easily to recognize since at least 3 different formalisms are employed:

Scattering: [5,14,15-18] The relative motion of 2 colliding atoms is described in detail, and cross sections are calculated for transitions between spin states. Kinetic gas theory then provides the relaxation rate.

Correlation functions: [8] This approach uses the correlation functions of transition matrix elements which are randomly varying in time because of the relative motion of two atoms. This motion does not have to be restricted to the well-defined scattering situation, but can also be diffusion-like. The first and well known theory of this class is the BPP theory named after the authors Bloembergen, Purcell and Pound.

Linear response theory: [2,12] This formalism calculates the time development of the macroscopic magnetization in response to a step function in the static magnetic field. This also applies to a small departure from thermal equilibrium in the population of spin levels, that occurs in a fluctuation. When applied to the H↓ system this theory is largely parallel to BPP theory; the same type of correlation functions for the translational 'lattice' modes are used.

We have chosen to describe first in some detail the calculations of Lagendijk[8] which seem to be the quickest route to a result for both

3-D and 2-D. After that we will briefly discuss other work. Finally a short compilation of the various results will be given and a comparison with experimental results will be made.

2.2. *The work of Lagendijk;* *a description of the correlation function formalism*

Lagendijk's[8] calculation is of the correlation function type. One can make use of the results of BPP theory up to the point where the type of lattice motions has to be specified. The correlation functions have to be calculated for the case of a dilute, almost ideal gas in 2-D or 3-D, or diffusional motion in more dense gases. The derivation of an expression for T_1^{-1} in terms of the spectral densities of random correlation functions is described in the book of Abragam[9]. The physical picture is the following: consider atom 1 with two spin states in a large magnetic field. A transition between these two levels can be induced by a weak magnetic field, transverse to the static field and oscillating at the Larmor frequency. This field can be produced by the magnetic moment on a neighboring atom, 2, which is moving by, so that the magnetic field felt by atom 1 is very rapidly varying in time. A spectral decomposition of this time dependent field will show that it can contain a component which is oscillating just at the proper frequency needed to induce a transition in atom 1.

Let us briefly review the derivation of Abragam: consider a system described by a Hamiltonian $\hbar\,\mathcal{H}$:

$$\mathcal{H} = \mathcal{H}_S + \mathcal{H}_{SL} + \mathcal{H}_L \qquad (2.1)$$

with $\mathcal{H}_S$ describing only the spin system with levels $|\alpha\rangle, |\beta\rangle, \ldots$ and $\mathcal{H}_L$ describing the 'lattice', i.e. the motion of the particles, and $\mathcal{H}_{SL}$ a weak coupling of the spin system to the lattice. Weak coupling means that the lattice induces transitions in the spin system, but the lattice is assumed to be a bath of infinite heat capacity so that the spin transitions do not influence the state of the bath. The transition probability W is calculated with 1st order time dependent perturbation theory to be:

$$W_{\alpha\leftarrow\beta} = J_{\alpha\beta}(\omega_{\alpha\beta}) \tag{2.2}$$

J being the Fourier transform of the correlation function $G_{\alpha\beta}(\tau)$ of the matrix element $\langle\alpha|\mathcal{H}_{SL}(t)|\beta\rangle$ with $\mathcal{H}_{SL}(t) = e^{i\mathcal{H}_L t}\mathcal{H}_{SL}e^{-i\mathcal{H}_L t}$. The coupling Hamiltonian can be expanded as

$$\mathcal{H}_{SL}(t) = \sum_q F^{(q)}(t)\, A^{(q)} \tag{2.3}$$

with $A^{(q)}$ operators that act on the spin variables and $F^{(q)}(t)$ random functions of the relative position of the particles. Next a density operator, σ , for the spin system is introduced, and a master equation describing the population changes in the spin system. It is convenient to work in an interaction representation which removes the spin part of the Hamiltonian: $\sigma^{\star} = e^{i\mathcal{H}_S t}\sigma e^{-i\mathcal{H}_S t}$. The master equation then reads

$$\frac{d\sigma^{\star}}{dt} = -\tfrac{1}{2}\sum_{qp} J_q(\omega_p^{(q)})\,[A_p^{(-q)},[A_p^{(q)},\sigma^{\star}]] \tag{2.4}$$

Here J_q is the Fourier transform of the correlation function of the corresponding $F^{(q)}$ and

$$A^{(q)}(t) = e^{i\mathcal{H}_S t}A^{(q)}e^{-i\mathcal{H}_S t} = \sum_p A_p^{(q)} e^{i\omega_p^{(q)} t} \tag{2.5}$$

(a second index p is needed here in case the spin system contains two different spin species, and $\hbar\omega_p^{(q)}$ is the energy difference of a transition that may involve a combined spin flip of both type of spins). The longitudinal magnetization $M_z \equiv \gamma\hbar N\langle I_z\rangle$ is an example of an operator whose expectation value can be calculated as $M_z = \gamma\hbar N\,\mathrm{Tr}\{\sigma^{\star}(t)I_z\}$. Of interest is the rate of change of M_z (or I_z); with eq. (2.4) one finds

$$\frac{d}{dt}\langle I_z\rangle = -\{\mathrm{Tr}\,A\,\sigma^{\star} - \mathrm{Tr}\,A\,\sigma_{eq}\} \qquad \text{with} \tag{2.6}$$

$$A \equiv \tfrac{1}{2}\gamma\hbar N \sum_{qp} J_q(\omega_p^{(q)})\,[A_p^{(q)},[A_p^{(-q)},I_z]] \tag{2.7}$$

The subscript 'eq' denotes the state of thermal equilibrium at a finite lattice temperature T_L. When the coupling $\mathcal{H}_{SL}$ is specified, e.g. the equivalent of the classical dipole-dipole interaction, the commutators in eq. (2.7) can be evaluated, and this leads to a formula of the type

$$\frac{d}{dt}\langle I_z\rangle = -T_1^{-1}\,[\langle I_z\rangle - \langle I_z\rangle_{eq}] \tag{2.8}$$

with T_1^{-1} the desired relaxation rate. For our case we need equation (88) of Abragam[9], for the case of unlike spins with $\langle S_z\rangle$ fixed:

$$\frac{1}{T_1^{II}} = \left(\frac{\mu_0}{4\pi}\right)^2 \gamma_I^2\gamma_S^2\hbar^2 S(S+1)N\left[\frac{1}{12}J^{(0)}(\omega_I-\omega_S)+\frac{3}{2}J^{(1)}(\omega_I)+\frac{3}{4}J^{(2)}(\omega_I+\omega_S)\right] \tag{2.9}$$

How does this apply to nuclear relaxation in spin-polarized atomic hydrogen ? The coupling Hamiltonian $\mathcal{H}_{SL} = \mathcal{H}_{dd}$, the dipole-dipole interaction, contains 3 terms since each atom has one electron (spin $\vec{S}$, γ_e) and one proton (spin $\vec{I}$, γ_p):

$$\begin{aligned}\hbar\mathcal{H}_{dd} = {} & \left(\frac{\mu_0}{4\pi}\right)\frac{\gamma_e^2\hbar^2}{r^3}\,[\vec{S}_1\cdot\vec{S}_2 - 3(\vec{S}_1\cdot\hat{r})(\vec{S}_2\cdot\hat{r})] \\ & - \left(\frac{\mu_0}{4\pi}\right)\frac{\gamma_e\gamma_p\hbar^2}{r^3}\,[\vec{S}_1\cdot\vec{I}_2 - 3(\vec{S}_1\cdot\hat{r})(\vec{I}_2\cdot\hat{r})] \\ & - \left(\frac{\mu_0}{4\pi}\right)\frac{\gamma_p\gamma_e\hbar^2}{r^3}\,[\vec{I}_1\cdot\vec{S}_2 - 3(\vec{I}_1\cdot\hat{r})(\vec{S}_2\cdot\hat{r})]\end{aligned} \tag{2.10}$$

Here we ignore the weak nuclear dipole-dipole interaction. The two hyperfine states a and b can be considered as the energy levels of a fictitious spin ½ system. To this fictitious spin one has to assign an effective gyromagnetic ratio γ_{eff} such that the energy difference $\gamma_{eff}\hbar B$ comes out to be the right $E_b - E_a$. From the energy level expressions eq. (4.5) one finds

$$\gamma_{eff} = \gamma_p\left(1 + \varepsilon\frac{g_e\mu_B}{g_N\mu_N}\right) = \gamma_p\left(1 + \varepsilon\frac{\gamma_e}{\gamma_p}\right)$$

with the 'enhancement factor' $(1 + \varepsilon\,\gamma_e/\gamma_p)$, which is due to the hyperfine interaction, having a value of 2.66 in a 10 Tesla field. The dipole-dipole interaction we now want to imagine as the interaction between an electron spin and an effective nuclear spin, the electron spin always remaining down ($m_S = -\frac{1}{2}$). We want to find an effective form for $\mathcal{H}_{dd}$ such that this gives the same matrix elements for transitions $|bb\rangle \leftrightarrow |ba\rangle$ and $|aa\rangle \leftrightarrow |ba\rangle$ as the true $\mathcal{H}_{dd}$ of eq. (2.10). The standard decomposition of $\mathcal{H}_{dd}$ for two unlike spins in the sense of (2.3) is:

$$\mathcal{H}_{dd} = -\left(\frac{\mu_0}{4\pi}\right) \frac{\gamma_I \gamma_S \hbar}{r^3} \left(A + B + C + D + E + F \right) \quad \text{with}$$

$$\begin{aligned}
A &= \phantom{-\tfrac{1}{4}} (1-3\cos^2\theta) && [I_z S_z] \\
B &= -\frac{1}{4} (1-3\cos^2\theta) && [I^+ S^- + I^- S^+] \\
C &= -\frac{3}{2} \sin\theta \cos\theta \, e^{-i\phi} && [\underline{I^+ S_z} + I_z S^+] \\
D &= -\frac{3}{2} \sin\theta \cos\theta \, e^{i\phi} && [\underline{I^- S_z} + I_z S^-] \\
E &= -\frac{3}{4} \sin^2\theta \quad e^{-2i\phi} && [I^+ S^+] \\
F &= -\frac{3}{4} \sin^2\theta \quad e^{2i\phi} && [I^- S^-]
\end{aligned} \tag{2.11}$$

and r, θ, ϕ being the spherical coordinates of the interatomic vector $\vec{r}$. Our effective $\mathcal{H}_{dd}$ takes the form

$$\begin{aligned}
\mathcal{H}_{dd,eff} &= -\left(\frac{\mu_0}{4\pi}\right) \frac{\gamma_e \gamma_p (1+\varepsilon\gamma_e/\gamma_p)\hbar}{r^3} \frac{3}{2} \sin\theta\cos\theta \, S_z \left[e^{-i\phi} I^+_{eff} + e^{i\phi} I^-_{eff} \right] \\
&= -\left(\frac{\mu_0}{4\pi}\right) \frac{\gamma_e \gamma_p (1+\varepsilon\gamma_e/\gamma_p)\hbar}{r^3} \sqrt{\left(\frac{6\pi}{5}\right)} \, S_z \left[Y_2^{1\star}(\hat{r}) I^+_{eff} - Y_2^{-1\star}(\hat{r}) I^-_{eff} \right]
\end{aligned} \tag{2.12}$$

so it contains only the underlined parts of C and D, and the $F^{(q)}(t)$ from eq. (2.3) are proportional to spherical harmonics $Y_2^m(\hat{r}(t))$. Calculation of the matrix elements for $|bb\rangle \leftrightarrow |ba\rangle$ and $|aa\rangle \leftrightarrow |ba\rangle$ is trivial now; they are all of the form

$$\mp \left(\frac{\mu_0}{4\pi}\right) \frac{\gamma_e \gamma_p (1+\varepsilon\gamma_e/\gamma_p)\hbar}{r^3} \sqrt{\left(\frac{6\pi}{5}\right)} \, \frac{1}{2} Y_2^{\pm 1\star} \tag{2.13}$$

This is to be compared with the matrix elements of eq. (2.10) which will be calculated when discussing the work of Statt and Berlinsky[5] in section 2.4. The matrix elements are identical in so far as we neglect terms that are higher than 1st order in one of the small parameters ε or γ_p/γ_e.

The transition $|bb\rangle \leftrightarrow |aa\rangle$, which means the simultaneous flip of 2 effective nuclear spins is impossible in the effective $\mathcal{H}_{dd}$ picture; in the full $\mathcal{H}_{dd}$ the matrix element turns out to be proportional to ε^2.

Lagendijk uses the definitions

$$F_m(t) = \ll \frac{Y_2^{m\star}(\hat{r})}{r^3} \frac{Y_2^m(\hat{r}(t))}{r(t)^3} \gg \qquad \text{and} \qquad (2.14)$$

$$F_m(\omega) = \int_{-\infty}^{\infty} e^{i\omega t} F_m(t)\, dt \qquad \text{with} \qquad (2.15)$$

$$\ll \text{Operator} \gg \equiv \text{Tr}\{e^{-\beta\hbar\mathcal{H}_L} \text{Operator}\}/\text{Tr}\{e^{-\beta\hbar\mathcal{H}_L}\} \qquad (2.16)$$

the ensemble average. The correspondence with Abragam is: $J^{(q)}(\omega) \longrightarrow \frac{8\pi}{15} F_m(-\omega)$. From eq. (2.9) we then have:

$$T_1^{-1} = \left(\frac{\mu_0}{4\pi}\right)^2 \frac{9\pi}{15} \gamma_e^2 \gamma_p^2 (1+\varepsilon\gamma_e/\gamma_p)^2 \hbar^2 N F_1(-\omega_I) \qquad (2.17)$$

(We have left out the transitions with $\omega_I \pm \omega_S$ because these involve an electron spin flip. The high energy needed for this is not available from the bath at low temperature.) Actually in Abragam's semi-classical derivation there is no distinction between $J(-\omega)$ and $J(\omega)$ because of the 'high temperature' approximation $\hbar\omega_I \ll k_B T_L$. In general we find $F_m(\omega) = F_m(-\omega) \exp(\hbar\omega/k_B T)$, $+\omega$ $(-\omega)$ corresponding to transition probabilities for transitions where the spin system loses (gains) energy, and T_1^{-1} is proportional to $F_1(-\omega) + F_1(\omega)$. In the experiments it is however the relaxation rate constant for $b \rightarrow a$ that is measured, rather than T_1^{-1} . Because of recombination all a-state atoms recombine, and there is *no approach of thermal equilibrium*. So we will calculate $F_1(\omega)$. Often however the spectral density is constant at low frequency and we can replace this by $F_1(0)$.

As the simplest model for the description of the lattice motions Lagendijk assumes that the particles are completely free, but cannot approach each other to a distance closer than a hard sphere diameter d, d = 3.67 Å . This is because two H atoms with their electron spins fully aligned interact via the triplet potential, and d is the classical turning point for zero kinetic energy. In low density only binary collisions occur. This treatment is called an excluded volume calculation, not to be confused with hard sphere scattering: in the former radial wavefunctions of non-interacting particles are used ($j_1(kr)$, spherical Bessel functions), which are truncated at a finite distance d from the origin. For the surface relaxation the particles are treated as an ideal 2-D gas; no motion in the z-direction is allowed. The same excluded volume principle as in 3-D is applied.

The calculation of the correlation functions proceeds as follows: (first in 3-D) : as basisfunctions are used

$$\frac{1}{V} e^{i\vec{K}\cdot\vec{R}} e^{i\vec{k}\cdot\vec{r}} = |\vec{K},\vec{k}\rangle \tag{2.18}$$

These are free particle wavefunctions, normalized in a volume V, in relative and center of mass coordinates. The correlation function to be calculated is

$$F_m(t) = \left\langle\!\!\left\langle \frac{Y_2^{m\star}(\hat{r})}{r^3} \frac{Y_2^m(\hat{r}(t))}{r(t)^3} \right\rangle\!\!\right\rangle$$

$$= \frac{1}{Z} \mathrm{Tr} \left\{ e^{-\beta\hbar\mathcal{H}_L} \frac{Y_2^{m\star}(\hat{r})}{r^3} e^{-i\hbar\mathcal{H}_L t} \frac{Y_2^m(\hat{r})}{r^3} e^{i\hbar\mathcal{H}_L t} \right\} \tag{2.19}$$

with $Z = \mathrm{Tr}\left\{ e^{-\beta\hbar\mathcal{H}_L} \right\}$. The identity operator $\mathrm{Tr}\, |\rangle\langle| = \frac{V^2}{(2\pi)^6} \int d\vec{K}_2 \int d\vec{k}_2$ is inserted between each of the operators in eq. (2.19), and

$$Z\, F_m(t) = \frac{V^4}{(2\pi)^{12}} \int d\vec{K}_1 \int d\vec{K}_2 \int d\vec{k}_1 \int d\vec{k}_2\, P\, Q\, R\, Q^\star R^\star \tag{2.20}$$

with
$$P = \langle \vec{K}_1 \vec{k}_1 | e^{-\beta\hbar\mathcal{H}_L} | \vec{K}_1 \vec{k}_1 \rangle = e^{-\frac{\beta\hbar^2 K_1^2}{4m}} e^{-\frac{\beta\hbar^2 k_1^2}{m}}$$

$$Q = \langle \vec{K}_1 \vec{k}_1 | \frac{Y_2^{m\star}(\hat{r})}{r^3} | \vec{K}_2 \vec{k}_2 \rangle$$

$$= \frac{1}{V^2} \int d\vec{R} \int d\vec{r}\; e^{i(\vec{K}_2 - \vec{K}_1)\cdot\vec{R}} e^{i(\vec{k}_2 - \vec{k}_1)\cdot\vec{r}} \frac{Y_2^{m\star}(\hat{r})}{r^3}$$

$$R = \langle \vec{K}_2 \vec{k}_2 | e^{-i\hbar\mathcal{H}_L t} | \vec{K}_2 \vec{k}_2 \rangle$$

(m is the mass of the hydrogen atom.)

One can subsequently integrate over $\vec{R}$ in $\mathcal{Q}$, integrate over $\vec{K}_2$, integrate over $\vec{R}$ in $\mathcal{Q}^\star$ and integrate over $\vec{K}_1$ (this removes the center of mass variables). By transforming to a new set of $\vec{k}$ - variables:

$$\vec{\delta} = \vec{k}_2 - \vec{k}_1 \ , \quad \vec{\sigma} = \vec{k}_1 + \vec{k}_2 \ , \quad \vec{\sigma}\cdot\vec{\delta} = k_2^2 - k_1^2 \ , \quad \vec{\sigma} - \vec{\delta} = 2\vec{k}_1 \tag{2.21}$$

one arrives at

$$Z \ F_m(t) = \frac{V \, m^{3/2}}{2^{3/2} (2\pi)^{15/2} \hbar^3 \beta^{3/2}} \ \times \tag{2.22}$$

$$\times \int d\vec{\delta} \int d\vec{\sigma} \left| \int d\vec{r} \ e^{i\vec{\delta}\cdot\vec{r}} \ \frac{Y_2^{m\star}(\hat{r})}{r^3} \right|^2 e^{-\frac{it\hbar\vec{\sigma}\cdot\vec{\delta}}{m}} \ e^{-\frac{\beta\hbar^2(\vec{\sigma}-\vec{\delta})^2}{4m}}$$

The standard expansion of a plane wave in spherical waves is

$$e^{i\vec{\delta}\cdot\vec{r}} = 4\pi \sum_{\ell,n} i^\ell j_\ell(\delta r) \ Y_\ell^{n\star}(\hat{\delta}) \ Y_\ell^n(\hat{r}) \tag{2.23}$$

(j_ℓ spherical Bessel function), and one has

$$\int d\vec{r} \ e^{i\vec{\delta}\cdot\vec{r}} \ \frac{Y_2^m(\hat{r})}{r^3} = -4\pi \ Y_2^{m\star}(\hat{\delta}) \int_d^\infty dr \ \frac{j_2(\delta r)}{r} \tag{2.24}$$

This follows from the orthonormality of the Y_ℓ^m under integration over both θ and ϕ , a full 4π solid angle integration. Next one writes $\vec{\sigma}\cdot\vec{\delta} = \sigma\delta \cos\theta$ and the Fourier transform is performed (eq. (2.15)). This introduces a delta-function $\delta\left(\omega - \frac{\hbar\sigma\delta\cos\theta}{m}\right)$ with θ one of the angles that constitute the integration over $\hat{\sigma}$. ($\omega = 0$ means $k_1^2 = k_2^2$ or $\vec{\sigma}\cdot\vec{\delta} = 0$, thus an elastic collision). Subsequently the integration over $\hat{\sigma}$ and σ can be performed and one finally obtains the result

$$Z \ F_m(\omega) = \frac{V \, m^{7/2}}{2^2 \pi^{7/2} \hbar^6 \beta^{5/2}} \int_0^\infty d\delta \ \delta \ e^{-\frac{\beta\hbar^2}{4m}\left[\frac{m^2\omega^2}{\hbar^2\delta^2} + \delta^2 - \frac{2m\omega}{\hbar}\right]} \left[\int_d^\infty dr \ \frac{j_2(\delta r)}{r} \right]^2 \tag{2.25}$$

The integral of j_2 is known and equal to

$$\int_d^\infty dr \ \frac{j_2(\delta r)}{r} = \sqrt{\frac{\pi}{2}} \ (\delta d)^{-3/2} \ J_{3/2}(\delta d)$$

(the result expressed in terms of the half-integer Bessel function $J_{3/2}$). The partition sum Z is:

$$Z = \frac{V^2}{(2\pi)^6} \int d\vec{K}_1 \int d\vec{k}_1 \, \langle \vec{K}_1 \vec{k}_1 | e^{-\beta\hbar\mathcal{H}_L} | \vec{K}_1 \vec{k}_1 \rangle = \frac{V^2 m^3}{(2\pi)^3 \beta^3 \hbar^6} \tag{2.26}$$

and as a result one has:

$$F_m(\omega) = \sqrt{(\pi m \beta)} \, \frac{1}{d^3 V} \, e^{\frac{\beta\hbar\omega}{2}} \int_0^\infty d\delta \, \frac{J^2_{3/2}(\delta d)}{\delta^2} \, e^{-\frac{\beta m \omega^2}{4\delta^2}} \, e^{-\frac{\beta\hbar^2\delta^2}{4m}} \tag{2.27}$$

One recognizes that $F_m(\omega)/F_m(-\omega) = e^{\beta\hbar\omega}$, meaning that at very low temperatures $(k_B T \lesssim \hbar\omega)$ the translational motion cannot deliver the energy needed to raise the spin system in energy by $\hbar\omega$. The integration over δ in eq. (2.27), in fact a thermal average, is in general quite complicated and can only be evaluated numerically, unless one puts $\omega = 0$ and $\beta \to 0$ or $\beta \to \infty$. Consider the low temperature limit $\beta \to \infty$; use the expansion

$$J_{3/2}(x) \approx (x/2)^{3/2} \left\{ \frac{1}{\Gamma(5/2)} - \frac{(x/2)^2}{\Gamma(7/2)} + \dots \right\} \tag{2.28}$$

which is valid for small x ; Γ is the gamma function. So

$$F_m(0) = \frac{4\, m^{3/2}}{9\pi^{1/2}\hbar^2\beta^{1/2} V} \left\{ 1 - \frac{4md^2}{5\beta\hbar^2} + \dots \right\} \tag{2.29}$$

which is apparently valid for $T \ll \frac{\hbar^2}{k_B m d^2} = 3.5$ K. Note that d does *not* enter in the final result to first order. F_m is independent of m; we need $m = 1$. With eq. (2.17) the final answer is: $(\beta \to \infty)$

$$T_1^{-1} = \left(\frac{\mu_0}{4\pi}\right)^2 \frac{4}{15} \sqrt{\pi} \, \gamma_e^2 \gamma_p^2 \, (1+\varepsilon\gamma_e/\gamma_p)^2 \, m^{3/2} \, n \, \sqrt{k_B T} \tag{2.30}$$

with $n = N/V$. For $B = 10$ T, $n = 10^{22}/\text{m}^3 = 10^{16}/\text{cm}^3$ the number is

$$T_1^{-1} = 1.89 \times 10^{-4} \sqrt{T} \quad [\text{sec}^{-1}] \; .$$

Relaxation times of order hours are thus predicted at low temperatures.

Whether or not it is justified to put $\omega = 0$ will have to be clarified in a numerical calculation. In fig. 2.1A the quantity

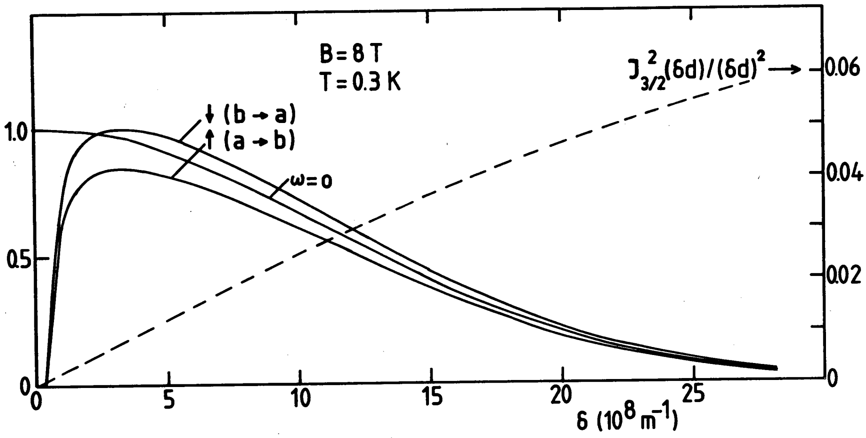

Fig. 2.1.A. The functions $e^{\pm\frac{\beta\hbar\omega}{2}}\, e^{-\frac{\beta\hbar^2\delta^2}{4m}}\, e^{-\frac{\beta m\omega^2}{4\delta^2}}$ *, ± for relaxation down (↓, b → a) and up (↑) , and in the approximation* $\omega=0$ *;* $T = 0.3$ *K On the right scale can be read the function* $J^2_{3/2}(\delta d)/(\delta d)^2$*, the other part of the integrand in eq. (2.27).*

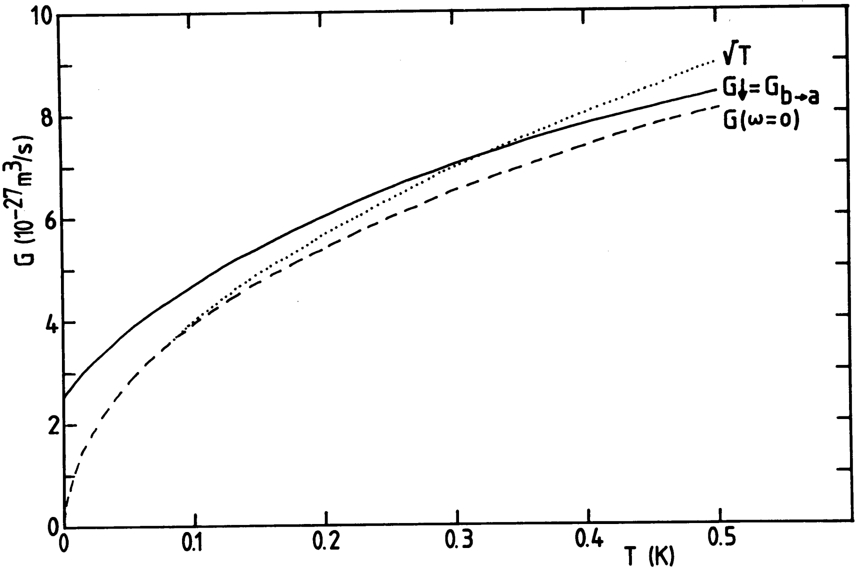

Fig. 2.1.B. $G\downarrow$ *(eq. (2.27),* $\omega > 0$*) compared to* $G(\omega = 0)$ *(eq. (2.29) and the low temperature* $\sqrt{T}$ *limit for* $G(\omega = 0)$ *(eq. (2.30). All rates are* PWBA *excluded volume, not yet symmetrized for bosons.*

$\exp[\pm \frac{\beta\hbar\omega}{2}]\exp[-\frac{\beta m\omega^2}{4\delta^2}-\frac{\beta\hbar^2\delta^2}{4m}]$ is plotted for T = 0.3 K, together with $J^2_{3/2}(\delta d)/(\delta d)^2$. The relaxation rates are proportional to the integral of the product of these two. This gives some impression of the effect of the $\omega = 0$ approximation: it shows what the thermal averaging (= integration over δ) can mean for a difference in the relaxation rate up or down. The maximum value for the curve '↑' (up) goes to zero as $\exp(-\hbar\omega/k_BT)$ as $T\to 0$, and the maximum of curve '↓' (down) remains 1. In fig. 2.1B the result of a numerical integration of eq. (2.27) is given.

At this point the rate constants G (G↓ and G↑) need to be introduced, defined by equations

$$\frac{dn_b}{dt} = - G{\downarrow}(n_b^2+n_bn_a) + G{\uparrow}(n_a^2+n_bn_a) = - n\,G{\downarrow}n_b + n\,G{\uparrow}n_a$$
$$\frac{dn_a}{dt} = + G{\downarrow}(n_b^2+n_bn_a) - G{\uparrow}(n_a^2+n_bn_a) = - \frac{dn_b}{dt} \qquad (2.31)$$

When only relaxation is studied, the relevant quantity is $T_1^{-1} \equiv n\,(G{\downarrow}+G{\uparrow})$, which describes the rate of change of a population difference towards its equilibrium value: $\frac{d}{dt}(n_b-n_a) = T_1^{-1}(n_b-n_a)_{eq.}$. In experiments with relaxation bottlenecked recombination, the rate equations (2.31) have to be extended with recombination terms:

$$\frac{dn_b}{dt} = - K_{ab}\,n_an_b \qquad\qquad - n\,G{\downarrow}n_b + n\,G{\uparrow}n_a$$
$$\frac{dn_a}{dt} = - K_{ab}\,n_an_b - 2\,K_{aa}\,n_a^2 + n\,G{\downarrow}n_b - n\,G{\uparrow}n_a \qquad (2.31^a)$$

When $K_{aa}, K_{ab} \gg G{\downarrow}$ a situation with $n_a \ll n_b$ develops; $(n_b-n_a)_{eq.}$ is never reached, and instead one observes

$$\frac{dn_b}{dt} \approx - 2\,G{\downarrow}\,n_b^2$$

The relevant quantity is thus G↓ , which is the one plotted in fig. 2.1B. For reference it is compared to $1/(2n)\;T_1^{-1}(\omega=0)$, the quantity commonly used so far in comparing theory with experimental data. The most important result of fig. 2.1B is that as T approaches zero, the relaxation rate remains finite, whereas the $\omega=0$ approximation gives a vanishing T_1^{-1} . Also we see that even at temperatures as 'high' as 0.5 K there is a considerable difference between these two. We realize that the often quoted $\sqrt{T}$ behavior for the relaxation rate is valid neither at low temperatures (because of the $\omega \neq 0$ correction just discussed) nor at higher temperatures (because of the expansion in powers of $md^2/(\beta\hbar^2)$ in eq. (2.29).

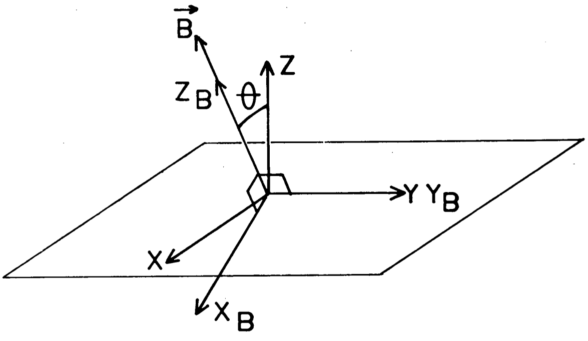

Fig. 2.2. Choice of the coordinate system XYZ *, with* Z *normal to the surface, and* $X_BY_BZ_B$ *with* $Z_B \,//\, \vec{B}$ *, the magnetic field.*

Next we turn to the same calculation in two dimensions. In 3-D the plane waves were expanded in spherical waves, and the completely isotropic motions in 3-D permitted us to choose a coordinate system with the Z-axis parallel to $\vec{B}$, the magnetic field. The Y_ℓ^n from the plane wave expansion and the $Y_2^{\pm 1}$ from the dipole-dipole interaction are thus all defined in the same coordinate system. One integrates over both θ and ϕ, and can make use of the orthnormality relations for the Y_ℓ^m. In 2-D the plane wave expansion would naturally assume a Z-axis normal to the surface plane in which the atoms are moving, and the integration is over ϕ only. The $Y_2^{\pm 1}$ from the dipole-dipole interaction is still defined in a system with Z-axis $//\,\vec{B}$, which in general makes an angle Θ with the surface normal (fig. 2.2). The rotation operator that transforms the system XYZ into $X_BY\ Z_B$ is $D\ (0,\Theta,0)$ and $Y_2^{\pm 1}$ in the new (B) system can be written as a linear combination of Y_2^m in the old (surface) system (see ref. 10 for the notation of the rotation matrix d) :

$$Y_2^n(\theta_B,\phi_B) = \sum_{m=-2}^{2} Y_2^m(\theta,\phi)\; d^2_{mn}(\Theta) \tag{2.32}$$

When calculating the correlation function (eq. (2.19) for m=1) one transforms to the surface system. Upon integration over ϕ the crossterms disappear because of the orthogonality of $e^{im\phi}$ and $e^{im'\phi}$. Since $Y_2^1 = 0$ for $\theta = \frac{1}{2}\pi$ ($\hat{r}$ is in the XY-plane) :

$$F_1(t) = F_0(t)\,[\,d^2_{01}(\Theta)\,]^2 + F_{-2}(t)\,[\,d^2_{21}(\Theta)\,]^2 + F_{-2}(t)\,[\,d^2_{-21}(\Theta)\,]^2$$

$$= \frac{3}{8}\sin^2(2\Theta)\;F_0(t) + \frac{1}{2}\,(1 - \cos^4(\Theta)\;F_2(t) \tag{2.33}$$

Regardless of what $F_0(t)$ and $F_2(t)$ will be, one can already conclude that the total relaxation rate is highly anisotropic with respect to the angle Θ : the contribution of F_0 vanishes for $\Theta=0,\frac{1}{2}\pi$ and the contribution of F_2 vanishes for $\Theta=0$. Furthermore we can expect that $F_0(\omega=0)$ is much larger than $F_2(\omega=0)$ from the following argument: $F_2(t)$ involves $Y_2^2(\frac{1}{2}\pi,\phi)/r^3 = \sqrt{(15/32\pi)}\;e^{2i\phi}/r^3$, thus the correlation of both the direction (ϕ) and the magnitude ($1/r^3$) of the interatomic vector $\vec{r}$, whereas $F_0(t)$ involves $Y_2^0(\frac{1}{2}\pi,\phi)/r^3 = -\sqrt{(5/16\pi)}\;1/r^3$, thus the correlation of $1/r^3$ only. Because of the much faster decay of $F_2(t)$, the spectral density at low frequencies is lower than that of F_0. One already recognizes that, in order to get a T_1^s as long as possible, one must orient most of the surface perpendicular to the field, and the surface that cannot be perpendicular should be parallel to the field. (We use the superscript ^{s} to distinguish the relaxation rate on the surface from the one in the bulk gas). To calculate $F_m(t)$ for m=0,2 one proceeds with the expression equivalent to eq. (2.22) :

$$Z\;F_m(t) = \frac{A\,m}{2^3(2\pi)^5\hbar^2\beta}\;\times \tag{2.34}$$

$$\times\;\int d\vec{\delta}\;\int d\vec{\sigma}\;\left|\int d\vec{r}\;e^{i\vec{\delta}\cdot\vec{r}}\;\frac{Y_2^{m\star}(\hat{r})}{r^3}\right|^2 e^{-\frac{it\hbar\vec{\sigma}\cdot\vec{\delta}}{m}\;-\;\frac{\beta\hbar^2(\vec{\sigma}-\vec{\delta})^2}{4m}}$$

All integrals are 2-D now, and the surface area A replaces the volume.

In the expansion of $e^{i\vec{\delta}\cdot\vec{r}}$ (eq. (2.23)) all terms with $\ell \geqslant m$, n=m give nonzero contributions to the integral $\int d\vec{r}\; j_\ell(\delta r)\; Y_\ell^n(\hat{r})\; Y_2^{m\star}(\hat{r}) \;/\; r^3$ as opposed to the 3-D case where only $\ell=2$ contributes. The assumption is made that only the lowest nonzero contribution is important, which assumption is easily checked by calculating some of the next higher order terms. By pursueing the same integration procedure as in 3-D one finds the equivalents of eq. (2.25) :

$$Z\;F_0(\omega) = \frac{5A\,m^{5/2}}{2^5\pi^{3/2}\hbar^4\beta^{3/2}} \int_0^\infty d\delta\; e^{-\frac{\beta\hbar^2}{4m}\left[\frac{m^2\omega^2}{\hbar^2\delta^2} + \delta^2 - \frac{2m\omega}{\hbar}\right]} \left[\int_d^\infty dr\,\frac{j_0(\delta r)}{r^2}\right]^2$$

$$Z\;F_2(\omega) = \frac{15^3 A\,m^{5/2}}{2^{12}\pi^{3/2}\hbar^4\beta^{3/2}} \int_0^\infty d\delta\; e^{-\frac{\beta\hbar^2}{4m}\left[\frac{m^2\omega^2}{\hbar^2\delta^2} + \delta^2 - \frac{2m\omega}{\hbar}\right]} \left[\int_d^\infty dr\,\frac{j_2(\delta r)}{r^2}\right]^2$$

and the partition function Z is calculated to be (2.35^{a,b})

$$Z = \frac{A^2}{(2\pi)^4} \int d\vec{K}_1 \int d\vec{k}_1\; e^{-\beta\left[\frac{\hbar^2 K_1^2}{4m} + \frac{\hbar^2 k_1^2}{m}\right]} = \frac{A^2 m^2}{(2\pi)^2\beta^2\hbar^4} \qquad (2.36)$$

The integrals $\int_d^\infty dr\,\frac{j_m(\delta r)}{r^2}$, m=0,2 , often written in a dimensionless variable $(r' = r/d)$: $\frac{1}{d}\int_1^\infty dr'\,\frac{j_m(\delta d r')}{r'^2}$, unfortunately cannot be integrated analytically, so one has to make a series expansion in the (small) parameter δd. This will work for $k_B T \ll \hbar^2/(4\,m\,d^2)$. When one limits to the case $\omega=0$ integrals of the type

$$\int_0^\infty \delta^n\; e^{-\frac{\beta\hbar^2}{4m}\delta^2}\; d\delta$$

for various powers n have to be calculated, and the expansion is essentially a temperature expansion in the small dimensionless quantity $\alpha \equiv \sqrt{(m\,d^2/\beta\hbar^2)} = 0.5286\,\sqrt{T}$. The result is:

$$F_0(\omega=0) = \frac{N}{A}\,\hbar\,d^{-4}(k_B T)^{-1}\,[\,1.963\,\alpha^2 - 3.480\,\alpha^3 + 3.731\,\alpha^4 + \,\dots\,]$$

$$F_2(\omega=0) = \frac{N}{A}\,\hbar\,d^{-4}(k_B T)^{-1}\,[\,0.798\,\alpha^4 - 1.223\,\alpha^5 + 0.552\,\alpha^6 + \,\dots\,] \qquad (2.37)$$

(there is a minor numerical difference with Lagendijk's result[8]). Note that, contrary to the 3-D case, the leading term in the temperature expansion does not make F_0 independent of the hard sphere diameter d: $F_0 \propto 1/d^2$. This sensitivity for the hard sphere parameter indicates that a large contribution to the correlation function comes from the relative distances close to the minimum value. F_2 is to first order independent of d. As expected, $F_2 \ll F_1$.

Let us compare the intrinsic relaxation rates in 2-D and 3-D :

$$\frac{F_0(\omega=0)_{2\text{-D}}}{F_1(\omega=0)_{3\text{-D}}} \approx 8\,\frac{N/A}{N/V}\,\frac{1}{d\alpha} = 8\,\frac{\bar{r}}{d\alpha} \qquad (2.38)$$

This follows from eqns. (2.37) and (2.29). $\bar{r}$ is the average interatomic distance which we take to be equal in 2-D and 3-D for the purpose of comparison. We ignore the anisotropy in 2-D and take the largest possible value. Since $\bar{r}/d \gg 1$ (otherwise the binary collision description would not be applicable) and $\alpha \ll 1$ we see that the intrinsic surface rate is much faster than the bulk rate. This is because there is less phase space available, so the correlation function exhibits a slower decay.

In calculating F_0 we have only considered the $\ell=0$ $m=0$ term, but neglected the higher order terms $\ell=2,4,6...$ $m=0$. As an example, the $\ell=2$ $m=0$ term would replace j_0 by j_2 in eq. (2.35^a) and give a different numerical factor in front; from (2.35^b) however we know that this only contributes in powers α^4 and higher, i.e. the third term in the expansion for F_0. It will thus be a small effect.

One could relax the $\omega=0$ restriction in a way similar to the 3-D case. Since the Bessel functions cannot be integrated analitically such a calculation would be somewhat more complicated. Moreover, there is another refinement of the theory that one should make, namely the use of properly symmetrized spatial wave functions as basis set. It does not seem to make much sense to drop the $\omega=0$ restriction unless one can do it in combination with the symmetrization procedure. This combined improvement will be made in 3-D and turns out to be very worthwile; for 2-D it is very complicated so we will maintain the $\omega=0$ approximation there. Instead of $e^{i\vec{K}\cdot\vec{R}}\, e^{i\vec{k}\cdot\vec{r}}$ (eq. (2.18)) one should in fact use from the very beginning :

$$\frac{1}{\sqrt{2}}\, e^{i\vec{K}\cdot\vec{R}}\, [\, e^{i\vec{k}\cdot\vec{r}} \pm e^{-i\vec{k}\cdot\vec{r}}\,]$$

with + or - chosen such that the total wavefunction, including spin parts, has the required symmetry for bosons or fermions (in our case $I = S = 1$ and the + sign applies for bosons). This symmetrization was not done in Lagendijk's original calculations. Without describing the details of the calculation, we mention the results only :

- In 3-D an 'exchange'-contribution to F_1, which has to be added to eq. (2.27), is found:

$$F_1^{ex}(\omega=0) = -\frac{\hbar^2}{8}\sqrt{(\beta^3/\pi m)}\,\frac{1}{d^3V}\, e^{\frac{\beta\hbar\omega}{2}} \times$$

$$\times \int_0^\infty \delta^2 d\delta \int_0^\infty \sigma^2 d\sigma\, \frac{J_{3/2}(\delta d)\; J_{3/2}(\sigma d)}{\delta^{5/2}\quad \sigma^{5/2}}\, \pi\, [\, 1 - \frac{3m^2\omega^2}{\hbar^2\sigma^2\delta^2}\,]\, e^{-\frac{\beta\hbar^2}{4m}[\sigma^2 - \delta^2]} \times$$

$$\times\, \Theta\, (\, |\frac{m\omega}{\hbar\sigma\delta}| - 1\,) \tag{2.39}$$

  (Θ is the unit step-function). For $\omega=0$ the exchange contribution is negative, making the net relaxation rate slower for bosons. For low temperatures the exchange contribution is - 1/2 times the direct contribution; for high temperatures the exchange term vanishes, giving eq. (2.27) the correct high temperature limit corresponding to a classical hard sphere calculation[11]. For $\omega \neq 0$ the exchange term can change sign, depending on the temperature. The final result is given in fig. 2.4, together with experimental results. It will be discussed in section 2.7 of this chapter. Both the $\omega \neq 0$ and the symmetrization procedure have an appreciable effect as $T \to 0$.
- In 2-D the exchange contributions are calculated only for $\omega=0$. For F_0 it turns out that the first two terms in an expansion in α are exactly equal to the ones in eq. (2.37). (This has interesting consequences for application to fermions, e.g. ^{3}He in binary collisions: the leading term in F_0 becomes $\propto \alpha^4$, making F_0 much smaller and of magnitude comparable to F_2.) The total, symmetrized result for bosons (H$\downarrow$) is:

$$F_0(\omega=0) = \frac{N}{A}\hbar d^{-4}(k_BT)^{-1}\,[\,3.927\,\alpha^2 - 6.960\,\alpha^3 + 6.582\,\alpha^4 + \ldots]$$
$$F_2(\omega=0) = \frac{N}{A}\hbar d^{-4}(k_BT)^{-1}\,[\,0.290\,\alpha^4 - 0.6116\,\alpha^5 + 0.3682\,\alpha^6 + ..] \qquad (2.37')$$

Lagendijk also calculates the correlation functions for diffusional motion. For 3-D this is described in Abragam[9] ; for H↓ one has to calculate eq. (2.14) with

$$P(\vec{r}(t),\vec{r},t) = (8\pi Dt)^{-1}\, e^{-\frac{(\vec{r}(t)-\vec{r})^2}{8Dt}} \qquad (2.40)$$

P being the probability of finding a particle (which was at $\vec{r}$ at time t=0), at position $\vec{r}(t)$ at time t. Eq. (2.40) is the solution of the classical diffusion equation

$$\frac{\partial}{\partial t}\,\Psi(\vec{r},t) = D\,\Psi \qquad (2.41)$$

where D is the diffusion constant. To proceed one Fourier transforms eq. (2.40) in $\vec{k}$ - space :

$$e^{-\frac{(\vec{r}(t)-\vec{r})^2}{8Dt}} = \left(\frac{4Dt}{2\pi}\right)^{3/2} \int d\vec{k}\; e^{-2Dtk^2}\; e^{i\vec{k}\cdot(\vec{r}(t)-\vec{r})} \qquad (2.42)$$

and the plane waves $e^{i\vec{k}\cdot\vec{r}}$ are expanded in spherical waves as in eq. (2.23). One finds

$$F_m(t) = \frac{1}{V}\frac{2}{\pi}\int d\vec{k}\; Y_2^{m\star}(\hat{k})\; Y_2^{m}(\hat{k})\;[\int_d^{\infty} dr\, \frac{j_2(kr)}{r}\,]^2\; e^{-2Dk^2t} \qquad (2.43)$$

As in the binary collision problem, the integral of the Bessel function is known. One can Fourier transform to the frequency domain, and

$$F_m(\omega) = \frac{1}{V}\frac{2}{\pi}\frac{1}{Dd}\int_0^{\infty} du\, \frac{1}{1+\frac{\omega^2 d^2}{4D^2u^2}}\,\frac{1}{u^3}\, J^2_{3/2}(u) \qquad (2.44)$$

($u \equiv kd$) and in the limit $\omega \to 0$:

$$F_m(\omega=0) = \frac{2}{15}\,\frac{1}{V}\,\frac{1}{Dd} \qquad (2.45)$$

When translating this to the *surface relaxation* problem, one first notes that the same partition of eq. (2.33) applies here as well. As in the binary collision treatment, the orthogonality relations for integration of the $Y_\ell^m(r)$ over both θ and ϕ do not apply, and one has to make the same assumption about the lowest non-zero ℓ-contribution. In the equivalent of eq. (2.43) the corresponding Bessel function integral is again *not* known; instead the most explicit expressions one can write down are

$$F_0(\omega) = 0.625\,\frac{N}{A}\,\frac{1}{Dd^2}\int_0^1 dk\,\frac{k^3}{k^4+\frac{\omega^2 d^4}{4D^2}}\left[\int_1^\infty du\,\frac{j_0(ku)}{u^2}\right]^2 \qquad (2.46^a)$$

$$F_2(\omega) = 3.296\,\frac{N}{A}\,\frac{1}{Dd^2}\int_0^1 dk\,\frac{k^3}{k^4+\frac{\omega^2 d^4}{4D^2}}\left[\int_1^\infty du\,\frac{j_2(ku)}{u^2}\right]^2 \qquad (2.46^b)$$

k in eqns. (2.46) is in fact $k'=kd$; the upper limit in the original k - integration has to be set at $1/d$ instead of ∞ (as implicitly assumed in 3-D), for the integrals can be divergent. The integrals in the square brackets have to be expanded in powers of k, and then the k - integration must be performed numerically. For F_2 the $\omega=0$ limit appears to be appropriate, so that a simpler integral can be calculated; not so however for F_0 where it results in a divergence. Lagendijk[8] finds a limiting expression for $\omega\to 0$.

For the diffusion constant one has to turn to kinetic gas theory. A simple treatment for hard spheres gives in 3-D :

$$D = \frac{1}{2}\,\bar{v}\,l = \frac{1}{2}\sqrt{(8k_BT/\pi m)}\,\frac{1}{\sqrt{2}n\pi d^2} \qquad (2.47)$$

with $\bar{v}$ the average velocity and l the mean free path. The same treatment in 2-D gives :

$$D = \frac{2}{\pi}\,\bar{v}\,l = \frac{2}{\pi}\sqrt{(\pi k_BT/2m)}\,\frac{1}{\sqrt{2}nd} \qquad (2.48)$$

where the 'cross length' d is the equivalent of the cross section πd^2

in 3-D. (Lagendijk uses $D = \frac{1}{3}\bar{v}\,\bar{l}$, the diffusion constant in 2-D in the first Enskog approximation.)

Because the diffusion constant depends on the density, the relaxation rate becomes proportional to n^2 ; since the binary collision rates are proportional to n there will be a cross-over at sufficiently high surface densities.

2.3. The work of Siggia and Ruckenstein[2,12]

In the first reference[2] the result of a bulk T_1^{-1} calculation is given without derivation. From the second reference we know that it is based on the same assumptions as Lagendijk's : no interatomic potential used, but an excluded volume in the relative coordinate integral. They also use the effective nuclear spin ½ concept. Two limiting cases are considered: $k_BT \gg$ or $\ll H_z$, H_z being the energy difference between the b- and a-level. The 'high' temperature expression gives the same result as Lagendijk (eq.(2.30) but without a temperature expansion :

$$T_1^{-1} = \left(\frac{\mu_0}{4\pi}\right)^2 \frac{64}{15} \sqrt{\pi}\, \mu_e^2\, \mu_\perp^2\, m^{3/2}\, n\, \hbar^{-4}\, \beta^{-1/2} \tag{2.49}$$

with $\mu_e = \frac{1}{2}\gamma_e\hbar$ and $\mu_\perp = \mu_p + \varepsilon\mu_e = \frac{1}{2}\gamma_p\hbar(1+\varepsilon\gamma_e/\gamma_p)$. An $\omega \neq 0$ result for very low temperature is also given : $(nT_1(\omega\neq 0))^{-1} = G\!\downarrow$ approaches a temperature independent value as $T \to 0$. Apparently the derivation is for non-symmetrized wavefunctions !

From the paper on surface relaxation[12] we learn more about the formalism used. Imagine the macroscopic nuclear magnetization has established the equilibrium value at some value of the static magnetic field. Then at t=0 a step is made in the field and the evolution of the magnetization towards the new equilibrium value is calculated. Strictly speaking this, linearized, response applies only to small departures of thermal equilibrium. The highly polarized ($n_b \gg n_a$) atomic hydrogen samples, corresponding to a very low negative spin-temperature, do not fall in this class. However the authors comment that they have found exponential decay of M_z with the same T_1 in these highly non-equilibrium states.

We will not describe the linear response formalism here; a good reference on this subject is the book of Wolf[13], ch. 5. Wolf's expression 5.75

$$T_1^{-1} = -\frac{1}{\hbar^2 \mathrm{Tr}(\mu_z^2)} \int_0^\infty dt\ \overline{\mathrm{Tr}\left\{[\mathcal{H}_{SL}^{\star}(t),\mu_z]\ [\mathcal{H}_{SL},\mu_z]\right\}} \qquad (2.50)$$

is equivalent to Ruckenstein and Siggia's eq. (1). (The bar denotes ensemble averaging, i.e. summation over all lattice states: $\bar{A} = 1/Z\ e^{-\beta\mathcal{H}_L} A$; the trace operation is over the spin states ($\mathcal{H}_S$) and $\mathcal{H}_{SL}^{\star}(t) = e^{i/\hbar(\mathcal{H}_S+\mathcal{H}_{SL})t}\mathcal{H}_{SL}e^{-i/\hbar(\mathcal{H}_S+\mathcal{H}_{SL})t}$, the $\star$ on $\mathcal{H}_{SL}^{\star}(t)$ denoting interaction representation.) We have (cf. eq. (2.12)) :

$$\mathcal{H}_{SL} = -\left(\frac{\mu_0}{4\pi}\right)\frac{3}{2}\gamma_e\gamma_\perp\hbar^2\sqrt{(8\pi/15)}\ \left[\frac{Y_2^{1\bigstar}(\hat{r})}{r^3}\ I^+S_z + \frac{Y_2^{-1\bigstar}(\hat{r})}{r^3}\ I^-S_z\right]$$

($\gamma_\perp \equiv \gamma_p(1+\varepsilon\gamma_e/\gamma_p)$ and $\mu_z = \gamma_\perp\hbar I_z$). Let us demonstrate that the above expression (2.50) for T_1^{-1} is equivalent to eq. (2.17), i.e. to the formalism of Abragam. First calculate the commutator

$$[\mathcal{H}_{SL}^{\star}(t),\mu_z] = -\left(\frac{\mu_0}{4\pi}\right) e^{i\omega t}\ \frac{3}{2}\gamma_e\gamma_\perp^2\hbar^3\ \sqrt{(8\pi/15)}\ \frac{Y_2^{1\bigstar}(\hat{r})}{r^3}\ [I^+S_z,I_z]\ + \text{h.c.} \qquad (2.51)$$

($\omega = \gamma_\perp B$). Then

$$[\mathcal{H}_{SL}^{\star}(t),\mu_z]\ [\mathcal{H}_{SL},\mu_z] = -\left(\frac{\mu_0}{4\pi}\right)^2 e^{i\omega t}\ \frac{9}{4}\ \gamma_e^2\gamma_\perp^4\hbar^6\ \frac{8\pi}{15}\ \frac{Y_2^{1\bigstar}(\hat{r}(t))}{r^3(t)}\ \frac{Y_2^1(\hat{r})}{r^3}\ \times$$

$$\times\ I^+I^-S_z^2\ + \text{h.c.} \qquad (2.52)$$

Now take the ensemble average and integrate over t :

$$\int_0^\infty dt\ \overline{\mathrm{Tr}[\ \ ]\ [\ \ ]} = -\left(\frac{\mu_0}{4\pi}\right)^2 <S_z>^2\ \frac{9}{4}\ \gamma_e^2\gamma_\perp^4\ \hbar^6\ \ \frac{8\pi}{15}\ F_1^{\bigstar}(\omega) \qquad (2.53)$$

where $F_1^{\bigstar}(\omega) = F_1(-\omega)$ by definition of eqns. (2.14) and (2.15). Since $<S_z>^2 = \frac{1}{4}$ and $\mathrm{Tr}\{\mu_z^2\} = \frac{1}{2}\hbar^2\gamma_\perp^2$ and by multiplying by N for a collection of spins, we find :

$$T_1^{-1} = \left(\frac{\mu_0}{4\pi}\right)^2 \frac{9}{15}\ \pi\ \gamma_e^2\gamma_p^2(1+\varepsilon\gamma_e/\gamma_p)^2\ \hbar^2\ N\ F_1(-\omega) \qquad (2.54)$$

which is identical to eq. (2.17). Second quantization operators are used to evaluate the correlation functions, apparently with the purpose of taking the identical particle aspects into account.

Concerning the surface relaxation, as opposed to a pure 2-D treatment, the atoms now have some freedom to move in the perpendicular z-direction. As wavefunctions are taken

$$\phi_0(z)\ e^{i\vec{k}\cdot\vec{\rho}} \qquad (\vec{k},\vec{\rho}\ \text{2-D vectors})$$

with $\phi_0(z)$ the single particle bound state wavefunction of a hydrogen atom in the H-He surface potential well. This introduces an averaging in the (3-D) interatomic vector $\vec{r}$ of the dipolar interaction, since the atoms are oscillating extremely fast in the surface potential. This averaging is of particular importance for the m=0 relaxation rate, which in the pure 2-D treatment was seen to have a leading term proportional to $1/d^2$ in a temperature expansion. The sensitivity for the hard sphere parameter d demonstrates that a large contribution to the rate comes from the very short distances $r \approx d$ (the m=2 rate is to first order independent of d, and there averaging of $\vec{r}$ in the dipolar interaction is unimportant). In a crude treatment the averaging of $1/r^3$ can be taken into account by defining a form factor F(d) which replaces $1/d^2$ in a pure 2-D calculation. For the average z-distance between two atoms, both of which are in the same $\phi_0(z)$ state, they estimate $\delta \approx 4.9$ Å for H on ^{4}He, which is even larger than the distance of closest approach $d = 3.67$ Å in the XY-plane ! So it has an important effect: $F(d) = 1/d^2\ (1 + \delta^2/d^2)^{-3} \approx 0.05/d^2$, and it reduces the relaxation rate by a factor 20.

Of course, the same partition (eq. (2.33)) in an m=0 and m=2 component with Θ anisotropy is found. After concluding that $(T_1^s)^{-1} = 0$ for $\Theta = 0$, they next turn to second order perturbation theory to calculate a possible finite relaxation rate for this orientation. It is concluded that even for very high surface densities, $n \approx 10^{13}/\text{cm}^2$, the Θ-anisotropy is only slightly affected.

2.4. *The work of Statt and Berlinsky*[5]

These authors have chosen to describe the relative motion of two hydrogen atoms as a scattering process with a realistic potential. An effective cross section σ_{eff} is calculated for the processes $|bb\rangle \rightarrow |ba\rangle$, $|aa\rangle \rightarrow |ba\rangle$ and vice versa. The cross sections turn out to be equal for all transitions (in the 'high temperature limit' = elastic scattering). σ_{eff} does depend on the relative kinetic energy of the incoming particles, and an average over the Maxwell distribution of velocities must be performed. This results in the expression

$$T_1^{-1} = \frac{1}{2}\, n\, \bar{v}_{rel}\, \beta^2 \int_0^\infty e^{-\beta E}\, \sigma_{eff}(E)\, E\, dE \qquad (2.55)$$

which is a well known expression from the collision theory of rate processes. (The factor ½ is connected with the exact definition of σ_{eff}, where identical particle aspects come into play.)

The calculation of σ_{eff} is done within the DWBA (Distorted Wave Born Approximation). This means that from the total Hamiltonian of two interacting H atoms, a small part $\mathcal{H}_1$ (in this case the dipole-dipole interaction, which causes the spin transitions) is split off. The relative motion for the two atoms is then calculated exactly for the remainder of the Hamiltonian, and matrix elements of $\mathcal{H}_1$ between incident and scattered states are calculated for the wavefunctions just found. Solving the scattering problem means solving the radial equation. Roughly speaking one would use the triplet potential as the central interaction for spin-polarized atomic hydrogen. Because of the hyperfine interaction and the mixed spin-states this is in general not correct, and Statt and Berlinsky take a closer look at this. Matrix elements of the dipolar interaction $\langle h_3 h_4 | \mathcal{H}_{dd} | h_1 h_2 \rangle$ with h a hyperfine level index, a or b, need to be calculated. The spin wavefunctions must be anti-symmetrized with respect to exchange of protons and electrons. One way to do this is to decompose the $|h_1 h_2\rangle$ states in the 16 states $|SNIM\rangle$, the coupled representation for both $\vec{S} = \vec{S}_1 + \vec{S}_2$, $N = m_S$ and $\vec{I} = \vec{I}_1 + \vec{I}_2$, $M = m_I$. Relevant for the moment are :

$$
\begin{aligned}
|bb\rangle &= |1{-}1{-}\rangle && (2.56)\\
|ba\rangle &= -\tfrac{1}{\sqrt{2}}\,|1{-}10\rangle + \tfrac{1}{\sqrt{2}}\,|1{-}00\rangle + \tfrac{\varepsilon}{\sqrt{2}}\,|101{-}\rangle - \tfrac{\varepsilon}{\sqrt{2}}\,|001{-}\rangle\\
|ab\rangle &= -\tfrac{1}{\sqrt{2}}\,|1{-}10\rangle - \tfrac{1}{\sqrt{2}}\,|1{-}00\rangle + \tfrac{\varepsilon}{\sqrt{2}}\,|101{-}\rangle + \tfrac{\varepsilon}{\sqrt{2}}\,|001{-}\rangle\\
|aa\rangle &= |1{-}11\rangle + \varepsilon\,|0000\rangle - \varepsilon\,|1010\rangle + \varepsilon^2\,|111{-}\rangle
\end{aligned}
$$

(- stands for -1). The dipolar interaction is already given in eq. (2.10) ; each of the three terms can be split in terms A - F in the sense of eq. (2.11). The 16 x 16 matrix of $\mathcal{H}_{dd}$ operating on the states $|SNIM\rangle$ should now be worked out for all these components, and after that the matrix elements $|bb\rangle \leftrightarrow |aa\rangle$, $|bb\rangle \leftrightarrow |ba\rangle$, $|bb\rangle \leftrightarrow |ab\rangle$, $|ba\rangle \leftrightarrow |aa\rangle$ and $|ab\rangle \leftrightarrow |aa\rangle$ are calculated with eq. (2.56). Such a matrix element will in general contain contributions with both S = 0 and S = 1 in $|SNIM\rangle$. To simplify the situation all contributing terms will be ordered in an expansion such that only terms proportional to $\gamma_e\gamma_p$ or $\varepsilon\gamma_e^2$ are retained. All terms that contain higher powers of one of the small parameters ε ($\approx 2.5\mathrm{x}10^{-3}$ in a 10 T field) or γ_p/γ_e (= 1/658) will be neglected. It turns out that the only significant terms of $\mathcal{H}_{dd}$ (eq. (2.10)) in this sense are:

$$
\sqrt{(6\pi/5)}\;\frac{Y_2^{1\star}(\hat{r})}{r^3}\;\{-\gamma_e\gamma_p(S_{1z}I_2^+ + I_1^+S_{2z}) + \gamma_e^2(S_1^+S_{2z} + S_{1z}S_2^+)\} + \text{h.c.} \qquad (2.57)
$$

$$
\equiv -\sqrt{(12\pi/5)}\;\frac{Y_2^{1\star}(\hat{r})}{r^3}\;\gamma_e\gamma_p\{T_{ep}^+ - \frac{\gamma_e}{\gamma_p}\,T_{ee}^+\} \qquad \text{h.c.}
$$

(note that Statt and Berlinsky use the definition $S^+ = \frac{1}{\sqrt{2}}\,(S_x + iS_y)$ which is non-standard). The 16 x 16 matrix for the relevant parts (2.57) is worked out in fig. 2.3 ; it can easily be checked that all non-zero matrix elements have I = 1 and S = 1 , so the triplet potential should be used everywhere in the scattering problem. The transition $|bb\rangle \leftrightarrow |aa\rangle$ can only be made by the term $S_1^+I_2^+ + I_1^+S_2^+$ or h.c. ; the matrix element is

$$
\langle aa|\gamma_e\gamma_p(S_1^+I_2^+ + I_1^+S_2^+)|bb\rangle = -\varepsilon\,\gamma_e\gamma_p
$$

$$\frac{1}{2\sqrt{2}} \times \begin{array}{c|cccccccccccccccc}
\text{SNIM} & 0000 & 0011 & 0010 & 001- & 1100 & 1111 & 1110 & 111- & 1000 & 1011 & 1010 & 101- & 1-00 & 1-11 & 1-10 & 1-1- \\
\hline
0000 & & & & & & & & & & 1 & & -1 & & & & \\
0011 & & & & & & & & & 1 & & & & & & & \\
0010 & & & & & & & & & & & & & & & & \\
001- & & & & & & & & & -1 & & & & & & & \\
1100 & & & & & & & & & -\gamma & & & & & & & \\
1111 & & & & & & & 1 & & & -\gamma & & & & & & \\
1110 & & & & & & 1 & & 1 & & & -\gamma & & & & & \\
111- & & & & & & & 1 & & & & & -\gamma & & & & \\
1000 & & 1 & & -1 & -\gamma & & & & & & & & \gamma & & & \\
1011 & 1 & & & & & -\gamma & & & & & & & & \gamma & & \\
1010 & & & & & & & -\gamma & & & & & & & & \gamma & \\
101- & -1 & & & & & & & -\gamma & & & & & & & & \gamma \\
1-00 & & & & & & & & & \gamma & & & & & & & \\
1-11 & & & & & & & & & & \gamma & & & & & & \\
1-10 & & & & & & & & & & & \gamma & & & & & \\
1-1- & & & & & & & & & & & & \gamma & & & &
\end{array}$$

Fig. 2.3 The matrix elements $\langle \overset{''''}{\text{SNIM}} \mid T_{ep}^{+} + T_{ep}^{-} - \gamma T_{ee}^{+} - \gamma T_{ee}^{-} \mid \text{SNIM} \rangle$.

$\gamma \equiv \gamma_e/\gamma_p$. *All elements are to be multiplied by* $\frac{1}{2\sqrt{2}}$.

and can therefore be neglected. One half of this matrix element is contributed by the transition $\mid 0000\rangle \rightarrow \mid 1-1-\rangle$, and is one of those matrix elements that involve the singlet potential. (Contrary to what Statt and Berlinsky state, there are more: for example $\gamma_e\gamma_p\langle 0000 \mid T_{ep}^{+} \mid 101-\rangle$, which occurs in $\mid ab\rangle \rightarrow \mid aa\rangle$ and has a magnitude $- 1/(2\sqrt{2})\ \varepsilon^2\gamma_e\gamma_p$.) Finally the relevant spin matrix elements are

$$\langle aa \mid T_{ep}^{+} - \gamma T_{ee}^{+} \mid ab\rangle = \frac{1}{2\sqrt{2}}\,(1 + \varepsilon\gamma)$$

$$\langle bb \mid T_{ep}^{-} - \gamma T_{ee}^{-} \mid ab\rangle = \frac{1}{2\sqrt{2}}\,(1 + \varepsilon\gamma)$$

thus equal for both transitions, and

$$\langle\ \mid \mathcal{H}_{dd} \mid\ \rangle = \frac{1}{2\sqrt{2}}\,(1 + \varepsilon\frac{\gamma_e}{\gamma_p})\gamma_e\gamma_p\ \sqrt{(12\pi/5)}\ \frac{Y_2^{\pm 1 *}(\hat{r})}{r^3} \qquad (2.58)$$

which is identical to eq. (2.13) as announced before.

We conclude this section by mentioning the final result: for low temperature a $T_1^{-1} \propto \sqrt{T}$ behavior is found. Analogous to what was found in fig. 2.2 we can expect that this is invalid for the whole temperature range $T \lesssim 0.5$ K, since the collisions were treated as elastic ($\omega=0$). The absolute rate agrees with the result of Lagendijk (PWBA : Plain Wave Born Approximation, with excluded volume) after proper symmetrization of the basis set for the latter. In the theory of Statt and Berlinsky the correct symmetrization is done by taking only terms with ℓ even in a partial wave decomposition. The influence of the real triplet potential only shows up in a slightly different temperature dependence at temperatures $\gtrsim 0.3$ K.

2.5. *The work of Statt*[14]

This is a calculation for 2-D ; it uses a scattering description in the DWBA formalism. The freedom of the particles to move in the z-direction is taken into account by treating the scattering as a 3-D problem; however it is still assumed that the wavefunction can be separated in a radial and a z-dependent part, with $\phi_0(z)$ approximated by simple model functions. This treatment is more satisfactory than the one by Ruckenstein and Siggia[12]; however we shall not discuss it here.

2.6. *The work of Ahn, v.d. Eijnde, Reuver, Verhaar, and Silvera*[15,16,17,18]

These authors have certainly undertaken the most ambitious project of this series. The calculations are of the scattering type, with a real potential. Concerning the bulk (3-D) relaxation[16,17] a so called coupled channels calculation is performed, which serves to check the relatively simple DWBA scattering treatment of ref.5, and in particular some of the approximations which were made there. They also give a very detailed account of identical particle aspects. The 3-D calculations prove the validity of the approximations made by Statt and Berlinsky[5], with of course one important exception: application of the (ω=0) 'High Temperature Limit' (HTL). Their final result, taken from ref.17 is included in fig. 2.4.

The 2-D calculations[15,16] are also in DWBA scattering with triplet potential, and are followed later[18] by coupled channels calculations. The motion of atoms in the z-direction is taken into account by a careful averaging of the dipolar interaction over a $\phi_0(z)$ wavefunction. They find that the crude treatment in ref. 12 is somewhat exaggerating the effect: for the triplet potential they find a reduction by a factor 3.5 with respect to a pure 2-D model, instead of 20 as is found with the 'form factor' F(d). In a later stage[18] an improvement was introduced upon this, which uses 2-particle wavefunctions instead of the $\phi_0(z)$ single particle bound state wavefunctions. A discussion of all this is beyond the scope of this thesis.

2.7. *Summary and Discussion*
Comparison with experiments

The results of all calculations for binary collisions in 3-D agree very well, when the so called 'High Temperature Limit' (ω=0) is dropped, and the proper symmetrization for wavefunctions is carried out. See fig. 2.4 for the results, calculated for B=8 Tesla, in which also the experimental data of Sprik, Walraven, van Yperen and Silvera[19] are plotted. The agreement between theory and experiment is reasonably well, except for the two lowest temperature points $T < 100$ mK. These however could well contain a contribution from surface relaxation. Surface relaxation was believed to be suppressed in these measurements by making use of the anisotropy properties, but it is not known down to which level.

In fig. 2.4 are also included the curves which would apply for fermions, and classical distinguishable particles. Here we have the first *experimental proof that hydrogen atoms behave as composite bosons in collisions !* This very elegant demonstration comes in a way which is completely independent of the interatomic potential: for the temperature range T = 0.1 - 0.3 K the result of a PWBA excluded volume calculation almost exactly coincides with the real potential result, indicating that the real (triplet) potential is of no importance here. The same theory[17] also describes reasonably well the measurements of MIT[20] and Cornell[21]. A direct comparison between all three sets of measurements is complicated

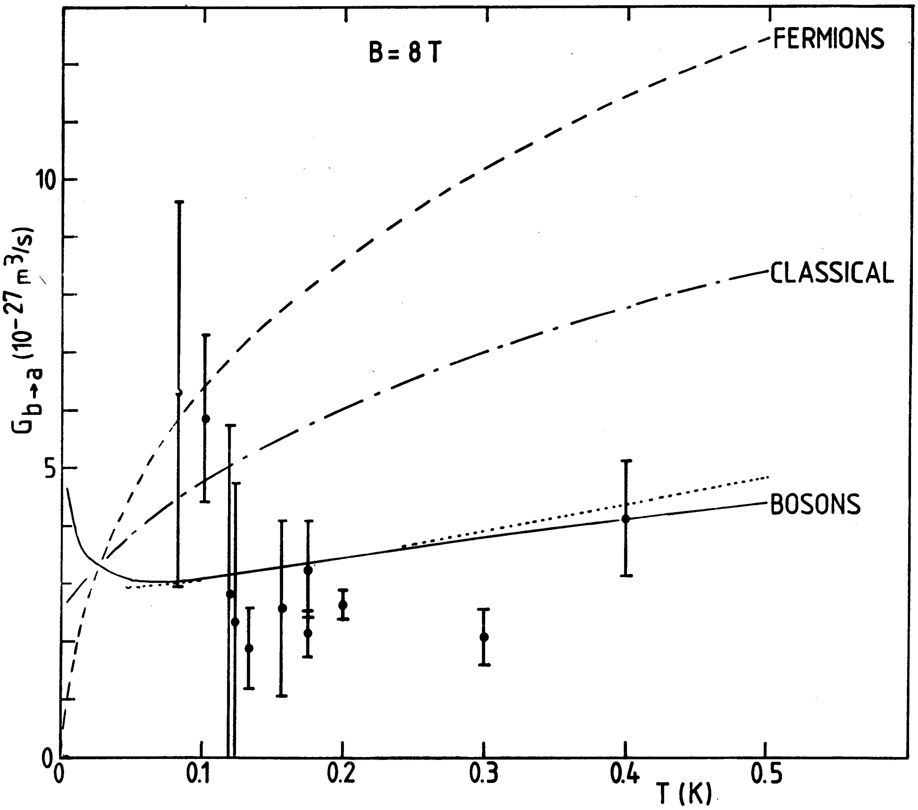

Fig. 2.4. Bulk relaxation rate $G_{b\to a}$ *for* $B = 8$ *T.*

———— *PWBA excluded volume calculation, symmetrized for bosons,* $\omega \neq 0$ *(this thesis)*

– – – – – *same as above, symmetrized for fermions*

—•—•—• *same as above, for 'classical' distinguishable particles*

••••••••• *DWBA triplet potential (ref. 17).*

The experimental data are taken from ref. 19.

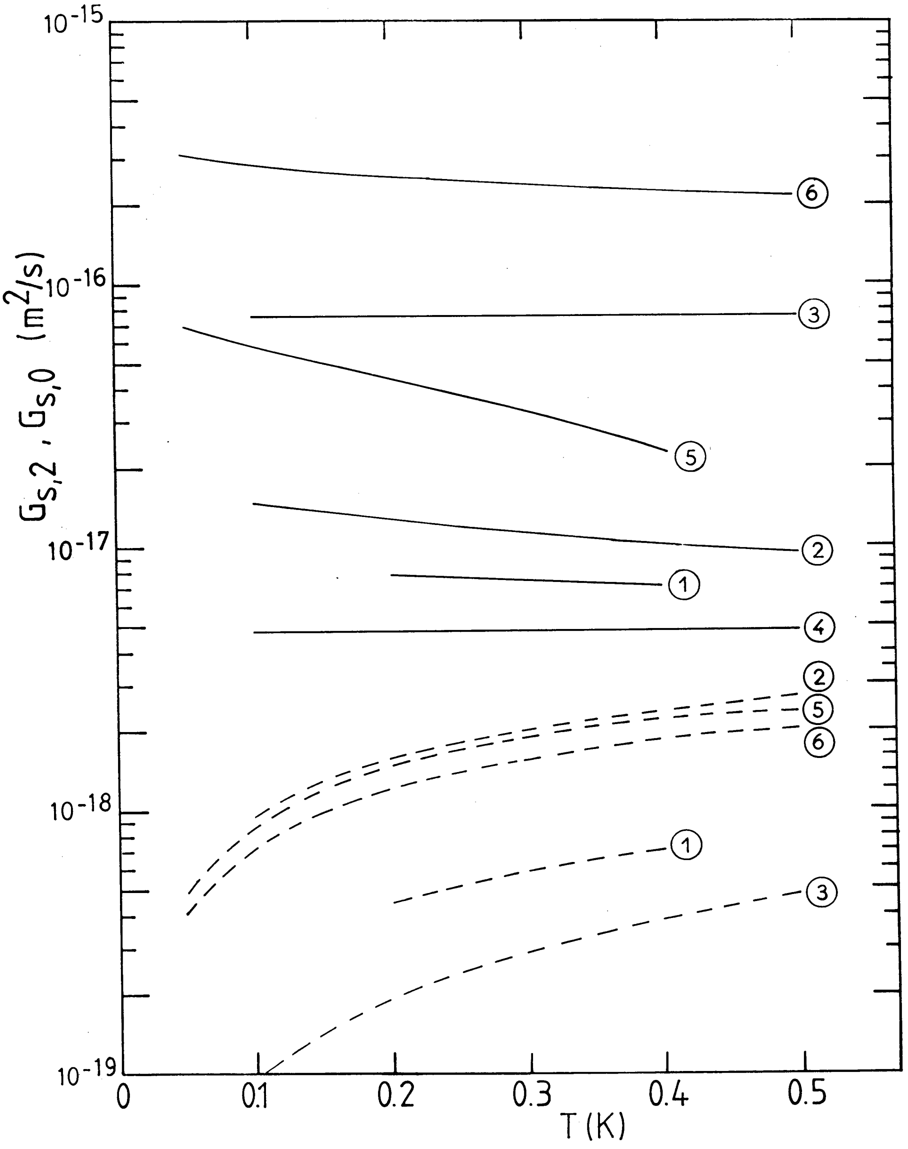

Fig. 2.5. Surface relaxation rates $G_s = G_{s,0}\sin^2 2\Theta + G_{s,2}(1 - \cos^4\Theta)$.

$G_{s,0}$ ——— , $G_{s,2}$ - - - .

① *ref. 15,* ② *ref. 14,* ③ *ref. 12 (^{4}He surface, pure 2-D model)*

④ *ref. 12 (probability distribution in z-direction),* ⑤ *ref. 8*

⑥ *this work (ref. 8, symmetrized for bosons).*

since the $(1+\varepsilon\gamma_e/\gamma_p)^2 = (1+16.68/B)^2$ field dependence no longer applies exactly when the $\omega=0$ limit is invalid.

Fig. 2.5 is a compilation of the results $G_s = (2nT_1^s)^{-1}$ for surface relaxation, all for B = 8 T, $\omega=0$ and a ^{4}He surface. There appears to be a considerable spread in these results, which is partly due to the different models used. Not only the absolute magnitudes, but also the temperature dependences are different. A detailed comparison of the T-dependence is not very meaningful at this stage, however, since the exponential temperature dependence in the effective[19] (measured) rate will obscure the intrinsic T-dependence:

$$G_{s,eff} = G_s\ (A/V)\ \lambda^2\ \exp(2\varepsilon_a/k_BT) \qquad (2.59)$$

with λ the thermal de Broglie wavelength and ε_a the adsorption energy (see also sec. 3.1). The area/volume ratio A/V can also be temperature dependent, if the magnetic field is not homogeneous throughout the cell, and there is a density distribution. Moreover, on (machined) surfaces one has to assume some model for the roughness, which averages out the strongly anisotropic surface relaxation rate. From the data of ref. 19 it follows that the observed rate on ^{4}He surfaces is about 50 times faster than theory[15]. On ^{3}He surfaces the surface relaxation rate is believed to be suppressed to an effective value lower than the bulk rate; it cannot be claimed however that it is suppressed to a level which is below the theoretical value.

We stress that the measured effective rates for H↓ on ^{4}He in three different experiments[19,20,21] agree reasonably well, although the geometry is quite different. When converting effective rates into intrinsic rates one should use a consistent value for the adsorption energy ε_a. Since there is still no perfect agreement on the value of ε_a, one might find a wide range of values for the intrinsic rates because of the exponential dependence on ε_a (eq. (2.59)).

The origin of the large discrepancy between experiment and theory is still unknown. It is sought in a better description of what happens exactly when two hydrogen atoms collide on the He surface (also possibly related to the interaction with the helium surface itself).

We would like to mention that we cannot totally exclude the possibility that the decay of doubly polarized H samples is in fact caused by direct recombination in some 2-body surface process, not yet understood, which depolarizes the electron spins. To check for a possibly false interpretation of the experiments, it is useful to measure the magnetic field dependence of the decay rate. This has been done in ref. 19; the data are cosistent with a $(1+\varepsilon\gamma_e/\gamma_p)^2 = (1+16.68/B)^2$ field dependence. However the interpretation of the data is somewhat complicated by the fact that A/V in eq. (2.59) is also field dependent; this number has to be calculated from the density distribution and changes by a factor 2 in the relevant field range. The data are not necessarily incompatible with another field dependence. The Θ - anisotropy (eq. (2.33)) is a signature by which the observed decay could be identified as surface relaxation. It is difficult to measure because it requires a surface which is flat on atomic scale. The measurements with $\Theta=0$ on ^{3}He surfaces seem to give support to the interpretation of the experimental data as surface relaxation bottlenecked recombination.

In the past there has been a lot of confusion about factors of 2 differences between various theories for dipolar relaxation in H↓. It seems appropriate to summarize the present conclusions on this subject here. These conclusions will be stated here without proof, since this would require an explanation which goes much more in depth than can be treated in this chapter. We will *not* be concerned here with the exact temperature dependence, but will examine various results in the $\omega=0$ and $T\to 0$ limit (this is of course not realistic, but still legitimate for tracing factors of 2 error that are related to normalization, symmetrization of wavefunctions etc.).

Let us first discuss bulk relaxation. The rate in ref. 2 and the unpublished result of Lagendijk mentioned in ref. 8 were both too large by a factor 2, because the wavefunctions were not symmetrized for bosons. This is settled now, as described in the present chapter. There may have been compensating errors in ref. 5 ; the final result is correct anyway.

Next we turn to surface relaxation. The variety of treatments of the finite extent of the wavefunction in the z-direction makes it almost impossible to trace errors of factors 2, so for the present purpose we will only consider the work of those authors who include a pure 2-D treatment as a special limiting case. Ref. 8 and ref. 12 both present excluded volume calculations. They agree in the $\omega = 0$ $T \to 0$ limit (see fig. 2.5, curves 5 and 3). In this thesis it is shown that the result of ref. 8 should be multipled by 4 (curve 6). (One factor 2 stems from symmetrization; besides there was another independent error.) This seems to introduce a discrepancy; however a careful inspection of a recent paper by Ruckenstein[§] shows that the rate in the (inappropriate) $\omega = 0$ $T \to 0$ limit is also 4 times faster than his previous result (ref. 12). This re-establishes the agreement. The statement of the authors of ref. 17, that the surface rate of ref. 12 should be divided by 2 must therefore be incorrect; it should be multiplied by 4.

In ref. 15 and 16 the result of a pure 2-D, excluded volume calculation is mentioned, by comparing it with $2\frac{1}{2}$-D, real potential. The ratio is about 16. The authors of ref. 15 admit that their excluded volume calculation was wrong; the ratio should be about 46. This also restores the agreement between all three known excluded volume calculations.

The $2\frac{1}{2}$-D triplet potential result of ref. 15 is not affected by this this: the same result, but now derived by relaxing the $\omega = 0$ limit (ref. 18) stands as the most realistic calculation for finite temperatures. We repeat that all conclusions about factors apply in the $\omega = 0$ $T \to 0$ limit; comparison of results at finite T can be misleading.

We also mention the correct procedure to compare a calculated T_1 with a measured $G\downarrow$: if T_1 is calculated for $\beta h \omega \ll 1$ then $G\downarrow = G\uparrow$ and $G\downarrow = 1/(2nT_1(\omega = 0))$; if T_1 is calculated for $\beta h \omega \gg 1$ then $G\downarrow \gg G\uparrow$ and $G\downarrow = 1/(nT_1(\omega))$.

[§] A.E. Ruckenstein: Magnetic relaxation rates in spin polarized hydrogen (preprint).

References of chapter 2

1. E.D. Siggia and A.E. Ruckenstein, Phys. Rev. Lett. 44, 1423 (1980).
2. E.D. Siggia and A.E. Ruckenstein, Phys. Rev. B23, 3580 (1981).
3. I.F. Silvera and J.T.M. Walraven in: *Recent Developments in Condensed Matter Physics*, J.T. de Vreese, ed. (Plenum Publ. Co., New York 1981) p. 29.
4. J.M. Greben, A.W. Thomas and A.J. Berlinsky, Can. J. of Physics 59, 945 (1981).
5. B.W. Statt and A.J. Berlinsky, Phys. Rev. Lett. 45, 2105 (1980).
6. R. Chapman, Phys. Rev. A12, 2333 (1975).
7. R. Chapman and M. Bloom, Can. J. of Physics 54, 861 (1976).
8. A. Lagendijk, Phys. Rev. B25, 2054 (1982), and private communication.
9. A. Abragam, *The principles of nuclear magnetism*, (Oxford University Press, 1961) ch. VIII· pp 268-295.
10. D.M. Brink and G.R. Satchler, *Angular Momentum*, (Oxford University Press, 1968) ch. II §§ 2.4-2.5.
11. F.M. Chen and R.F. Snider, J. Chem. Phys. 46, 3937 (1967).
12. A.E. Ruckenstein and E.D. Siggia, Phys. Rev. B25, 6031 (1982).
13. D. Wolf, *Spin-temperature and nuclear-spin relaxation in matter*, (Clarendon Press, Oxford 1979) ch. 5.
14. B.W. Statt, Phys. Rev. B25, 6035 (1982).
15. R.M.C. Ahn, J.P.H.W. v.d. Eijnde, C.J. Reuver, and B.J. Verhaar, and I.F. Silvera, Phys. Rev. B26, 452 (1982).
16. R.M.C. Ahn, Masters thesis, Technical University Eindhoven, Netherlands (1982).
17. R.M.C. Ahn, J.P.H.W. v.d. Eijnde, and B.J. Verhaar, Phys. Rev. B27, 5424 (1983).
18. J.P.H.W. v.d. Eijnde, C.J. Reuver, and B.J. Verhaar, prepint (1983).
19. R. Sprik, J.T.M. Walraven, G.H. van Yperen and I.F. Silvera, Phys. Rev. Lett. 49, 153 (1982).
20. R.W. Cline, T.J. Greytak, and D. Kleppner, Phys. Rev. Lett. 47, 1195 (1981).
21. B. Yurke, J.S. Denker, B.R. Johnson, N. Bigelow, L.P. Lévy, D.M. Lee, and J.H. Freed, Phys. Rev. Lett. 50, 1137 (1983).

CHAPTER III EXPERIMENTS WITH $H\downarrow$ ON ^{4}HE SURFACES AND ^{3}HE-^{4}HE MIXTURES

3.1. Introduction

In recent experiments[1] it has been shown that atomic hydrogen can be stabilized against recombination by polarizing the electron spins ($H\downarrow$) at low temperature ($\lesssim 0.5$ K) and large magnetic field ($B \approx 8$ T) and by coating the walls of the sample cell with a film of superfluid helium (^{4}He). Some aspects of this experiment have already been discussed briefly in section 1.2 of this thesis.

Helium is considered to be the best conceivable surface coating material to suppress adsorption of H atoms on the walls and subsequent recombination, caused by collisions between two hydrogen atoms adsorbed on the surface. The favorable properties of helium are: a low bulk density and low polarizability, which give rise to a weak Van der Waals attraction between an H atom and the helium surface, $\propto 1/z^3$ (z is the distance above the surface), and the surface profile: a smooth transition of the bulk density to zero over ~5 Å. Together these two properties create an effective interaction potential which has a shallow minimum of only a few degrees K (fig. 3.1). Theoretical calculations are

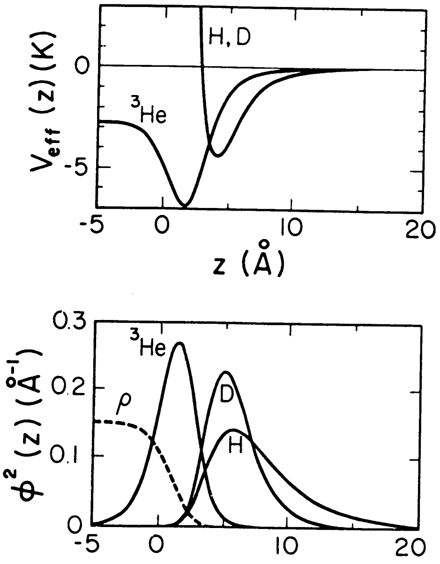

Fig. 3.1.

upper graph: effective interaction potential $V_{eff}(z)$ for a H atom on a ^{4}He surface.

lower graph: probability density functions $\phi^2(z)$ for the surface bound states of H, D and ^{3}He on ^{4}He with surface profile $\rho(z)$. (from ref. 4) available for these effective interaction potentials[2,3], and also for the existence of one (or more) possible surface bound states. The calculations are very subtle; they predict a binding energy (or adsorption energy) ε_a for H on ^{4}He of 0.1 K (Guyer and Miller[3]) and $\geqslant 0.6$ K (Mantz and Edwards[2]). As a consequence experimental determinations are very important, not only intrinsically, but also as a guide to theory.

The practical consequences of the surface bound state can be explained as follows. If there is a bound state, then there will be a non-zero average surface coverage, n_s. This is not a fixed group of atoms, but there will be a continuous exchange of H atoms between the bulk gas and the surface. This rapid exchange (typically on nanosecond timescale) leads to an equilibrium between the bulk or volume density, n_V, and the surface coverage. The equation describing this equilibrium can be derived by requiring that the chemical potential μ is equal for the bulk (3-D) and surface (2-D) phase. For an ideal Bose gas in the low density limit[4] ($n_V\lambda^3 \ll 1$, $n_s\lambda^2 \ll 1$; $\lambda = \sqrt{2\pi\hbar^2/mk_BT}$ is the thermal wavelength) we have:

$$\begin{aligned} \mu_{3D} &= k_BT \ln (n_V\lambda^3) \\ \mu_{2D} &= -\varepsilon_a + k_BT \ln (1-\exp(-n_s\lambda^2)) \\ &\approx -\varepsilon_a + k_BT \ln (n_s\lambda^2) \end{aligned} \tag{3.1}$$

The adsorption isotherm for the limit of low densities takes the form

$$n_s = n_V \lambda \exp (\varepsilon_a/k_BT) \tag{3.2}$$

This remains valid until H-H interaction effects become important[4,5]; this happens first in 2-D. At a fixed density n_V, n_s is seen to depend strongly on temperature because of the exponential function in eq. (3.2). In an experimental situation we usually have most atoms in the bulk: $N = Vn_V + An_s \approx Vn_V$ (N is total number of atoms). Recombination has been shown to occur at the surface, in binary collisions between H atoms. We have $\dot{n}_s = -K_sn_s^2 - \frac{V}{A}\dot{n}_V$ (the first term describes 2nd order decay due to recombination; the second term is the net exchange between surface and bulk). Since $\dot{n}_s \ll \frac{V}{A} \dot{n}_V$ (this is equivalent to the assumption that most atoms are in the bulk), we have a rate equation for n_V :

$$\dot{n}_V = -(\tfrac{A}{V})\ K_s n_s^2 = -(\tfrac{A}{V})\ K_s\ \lambda^2\ \exp(2\varepsilon_a/k_B T)\ n_V^2 \qquad (3.3)$$

So the decay of the bulk density, which is what can be observed in an experiment, is also described by a 2nd order rate equation

$$\dot{n}_V = -\ K_s^{eff}\ n_V^2\ , \text{ with } K_s^{eff} \text{ defined by}$$

$$K_s^{eff} = K_s\ (\tfrac{A}{V})\ \lambda^2\ \exp(2\varepsilon_a/k_B T) \qquad (3.4)$$

(this definition differs by a factor 1/V from eq. (1.12), because we now write rate equations in n instead of N). The strong dependence of K_s^{eff} on temperature offers an interesting method to determine the adsorption energy ε_a, which is employed in this experiment. On the other hand surface recombination determines the maximum densities that can be achieved in steady state in the bulk: the rate of surface recombination ($\dot{n}_s$) is compensated by the filling rate ($\dot{n}_V = \Phi/V$, Φ is the flux in atoms/sec). Combined with (3.2) we have:

$$n_{V,max} = \sqrt{\Phi/AK_s}\ \ \lambda^{-1}\ \exp(-\varepsilon_a/k_B T) \qquad (3.5)$$

The smaller ε_a, the easier it is to produce high densities of H↓, until 3-body effects in the bulk may become restrictive.

ε_a for H on ^{4}He has been measured by Morrow et al.[6] (unpolarized H in zero magnetic field, $\varepsilon_a/k_B = 1.15 \pm 0.05$ K) and by Matthey et al.[7] (H↓ on ^{4}He in strong fields, $\varepsilon_a/k_B = 0.89 \pm 0.07$ K). (These values do not agree perfectly. Independently determined values have become available since [8,9,10].) The rate constant K_s depends strongly on the magnetic field. Let us take for the moment the values of ref. 7: for a flux of 10^{15} at/sec we find at T = 0.4 K, B = 8 T: $n_{V,max} = 4.3\text{x}10^{16}/\text{cm}^3$, and correspondingly lower at lower temperature. These are indeed about the highest densities observed in steady state on ^{4}He. This is still far

away from the conditions needed to observe the Bose-Einstein transition in the gas: e.g. $T_c = 0.1$ K, $n_V = 1.5\times10^{19}/\mathrm{cm}^3$. Of course moderate improvements can be made by increasing Φ (but this increases the steady state recombination and the accompanying heat load), or decrease the area A, or decrease K_s (which is proportional to $1/B^2$, ref. 7) but because of the exponent in eq. (3.5) a reduction of ε_a would be most promising. ^{3}He as a surface coating material could serve this purpose. Although no detailed calculations for H on ^{3}He are published, ^{3}He is expected to give a lower adsorption energy for the following reasons:
1) the bulk density is lower than that of ^{4}He, and
2) the surface profile extends over a broader range.
Some preliminary experiments with ^{3}He have been carried out: Silvera and Walraven[11] used pure ^{3}He to coat the cell walls, but could not stabilize any measurable amount of H↓; they concluded that the superfluid properties of the ^{4}He film are essential, especially for good surface coverage of the critical region between HEVAC and accommodator. They also used ^{3}He-^{4}He mixtures, which were found effective. Matthey et al.[7] used ^{4}He diluted up to a very small amount (0.2 %) of ^{3}He and observed a decrease in the effective recombination rate constant K_s^{eff}. This can be attributed to a decrease of the adsorption energy ε_a/k_B : 0.89 K → 0.59 K. Single ^{3}He atoms are known to have a surface bound state on ^{4}He, analogous to H [2,3]. At low enough temperatures one expects that the first ^{3}He atoms admitted to a film of ^{4}He will occupy these surface states, until at least a monolayer coverage is reached. This explains the large effect of only such small ^{3}He concentrations. Of course it is to be expected that a further decrease of ε_a can be realized if a thicker film of ^{3}He on top of the necessary ^{4}He superfluid underlayer can be prepared. The limitations to the amount of ^{3}He that could be used were set by the temperature: at T = 0.42 K the saturated vapor pressure of pure ^{3}He equals the pressure of a density of H↓: $n_{H\downarrow} = 10^{15}/\mathrm{cm}^3$ (43×10^{-3} Torr). This means that measurement of the decay of H↓ density, which is done by a pressure gauge, is strongly affected by small fluctuations in temperature. Temperatures lower than the minimum of 0.34 K in ref. 7 are necessary to do experiments with more ^{3}He, both to suppress the effect of ^{3}He vapor pressure, as well to control K_s^{eff} to a

timescale which is convenient to observe the decay in case ε_a is indeed reduced.

Another item which could not be studied seriously in the experiment of ref. 7 is the mechanism of relaxation bottlenecked recombination, proposed by Hardy, Statt and Berlinsky[12]. H↓ consists of atoms in two hyperfine states (fig. 1.3) $a = -|{\downarrow}⤉\rangle + \varepsilon|{\uparrow}⤈\rangle$ and $b = |{\downarrow}⤈\rangle$. In high field $\varepsilon \approx a/4\mu_B B$ is a small mixing parameter, introduced by the hyperfine interaction a, giving the probability amplitude of measuring electron spin up (↑) in the a-state. The admixture ε controls the recombination rate to the molecular (spin singlet) state, as has been shown by the field dependence measurements of ref. 7. As a consequence, when we consider binary collisions between H atoms, a-a and a-b collisions can lead to recombination, but b-b collisions cannot. If the nuclear spin relaxation time T_1, giving the rate of transitions a↔b is long, a gas of initially equal amounts of atoms in states a and b will not decay to zero density, but a finite amount of atoms, all in the b-state will remain (e.g. 1/4 of the initial total density in the simplified hypothetical case that the rates of recombination in a-a and a-b collisions, K_{aa} and K_{ab}, are equal). Further decay of the sample is controlled by the nuclear T_1. Statt and Berlinsky[12] calculate T_1 for dipole-dipole relaxation in bulk, 2-body collisions, and find a very long T_1 : 4.5 hr at $B = 10$ T, $n = 10^{16}/\mathrm{cm}^3$, $T = 0.5$ K and only weakly temperature dependent. This process would in principle enable the stabilization of much higher densities of H↓ in the b-state alone. The reality of this interesting mechanism could not be demonstrated so far for two reasons:

1) because of insufficient magnetic compression (eq. (1.7)) thermal leakage causes a decay of the finite amount of b-state atoms that are supposed to decay on timescale set by the long T_1;
2) because of the finite runtime (2 hr) of the single shot ^{3}He evaporation cryostat it was difficult to record a decay over sufficiently large dynamic range to observe the decay to a limiting value of say 1/4 of the initial density instead of zero.

To overcome these problems an experiment was prepared in a ^{3}He-^{4}He dilution refrigerator, allowing lower temperatures (down to at least

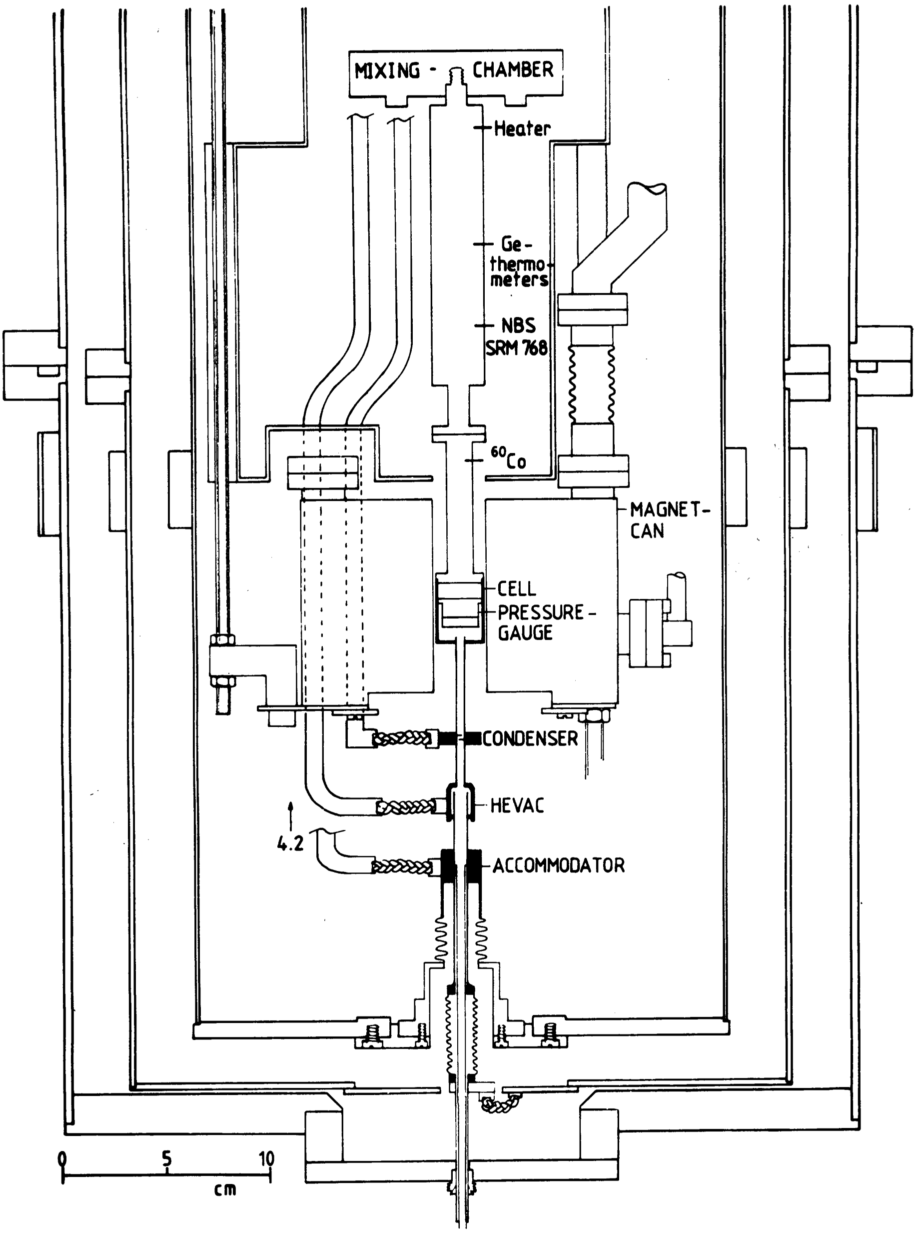

Fig. 3.2. H↓ stabilization cell and loading system.

30 mK), thus enabling a wider range of ^{3}He concentrations to be used, and allowing a better suppression of thermal leakage, together with arbitrarily long run times. This experiment will be described in the coming section 3.2.

3.2. Experimental details

The incorporation of the experiment in a ^{3}He-^{4}He dilution refrigerator is schematically indicated in fig. 1.4; the heart of the experiment is shown in fig. 3.2, which is drawn to scale. Thin walled german silver tube (o.d. 6 mm, wall thickness 0.15 mm) is used to provide thermal isolation between the various temperature stages of the fill line up to the HEVAC; stainless steel (o.d. 4 mm, wall thickness 0.20 mm) was used between HEVAC and condenser, and condenser and cell. The condenser contains a copper baffle to condense any residual vapor that has not been condensed in the HEVAC. It also acts as a trap for room temperature radiation. The '77 K' pinning is connected to the conduction cooled tail of the liquid N_2 tank; it operates at 100 K. The 4.2 K pinning is connected via a heavy copper pole and a flexible copper braid to the liquid helium in the magnet container. It operates at 4.8 K. The HEVAC is connected to the dilute stream in the continuous (spiral) heat exchanger of the dilution unit. The thermal contact is via a ~40 cm long, 1 cm^2 cross sectional area copper pole in series with a 0.2 cm^2, 8 cm long flexible copper braid. When the system was loaded with the standard amount of 28×10^{-6} mol ^{4}He, the HEVAC operated at $T = 0.725$ K. On the basis of extrapolation of cooling power measurements it is found that the refluxing He vapors cause a heat load of 0.4 mW on the HEVAC. The copper link can easily transport this heat load without excessive temperature drop; however there appears to be a Kapitza resistance problem at the connection of the pole to the heat exchanger: a temperature difference of ~ 400 mK between the dilute mixture and the copper was found. The contact is a 2 cm^2 soft soldered joint on the outside of the brass tube of the heat exchanger. In later experiments this has been improved by increasing the area of contact. The condenser or thermal platform was connected via a similar link to the dilution refrigerator's Cold Plate; this is a radiation screen connected with copper sinter to the dilute stream in between the continuous heat exchanger and the first discrete heat exchanger. It operates at T = 350 mK and puts a heat load of 0.45 mW on the cold plate. The cell is connected to the mixing chamber of the dilution refrigerator. It can cool to temperatures as low as 30 mK with a thick film of ^{4}He in the system, thanks to the operation of HEVAC and condenser. The condenser is located in the field profile of the max. 12 T magnet at 33 % of the central field; the HEVAC (bottom) at 7.5 %.

The cell contains a sensitive capacitive pressure transducer, which is essentially the same as the one used by Matthey et al.[7], except that there is no superleak connecting the reference vacuum and the sample chamber (fig. 3.3). The pressure gauge was recalibrated, after some

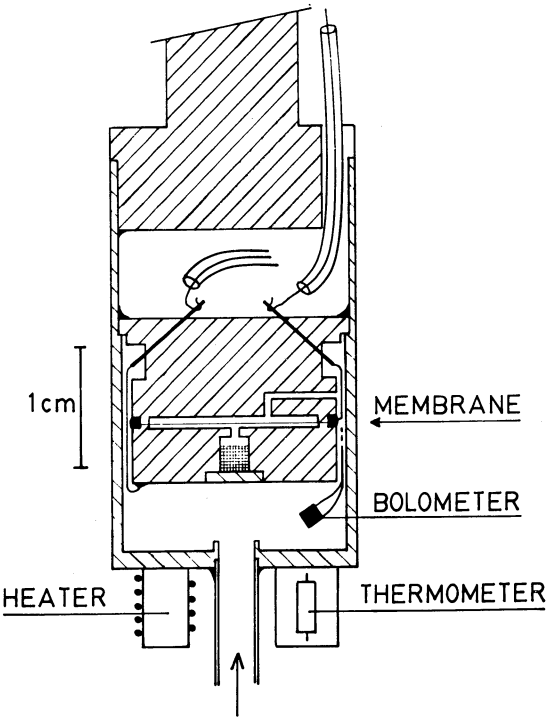

Fig. 3.3.

The hydrogen stabilization cell, showing in detail the capacitive pressure transducer.

changes were made to it, in a test set-up at 1.5 K. The line connecting the cold pressure gauge to the (room temperature) Barocel[13] pressure standard had a well defined geometry (straight tube of uniform diameter 5.7 mm) to allow for an accurate correction of the thermomolecular effect[14]. The sensitivity was $\Delta C/p = 6.70$ [pF/Torr] + 1.40 p [pF/Torr^2] and the zero capacitance 52.6 pF. The capacitance readout was done by a General Radio bridge type 1615-A, driven by 10 V_{eff}, 1 kHz oscillator voltage. The resolution in a 1 Hz bandwidth corresponded to a pressure of 10^{-6} Torr. In the cell is also mounted a trigger bolometer[1] used to destroy the H↓ sample, to define a zero on the pressure scale. The cell has a volume of 1.7 cm^3 and a surface area of 32 cm^2.

Because of the importance of accurate sample temperature determinations in this experiment we will devote a separate section to thermometry.

3.3. Thermometry

Thermometry was done with carbon resistors. We use 1/8 W 200 Ω Matsushita resistors[15]. Some pre-treatment and selection was done to obtain a set of thermometers with a reasonably similar low temperature R(T) characteristic and good thermal cycling behavior. All resistors from a lot of 200 were measured and divided in groups with 1 Ω intervals. They were cycled between room temperature and + 120° C a few times; this typically increases the resistance by 2 Ω. After that all resistors were cycled between room temperature and liquid N_2 temperature some 10 - 20 times; this again increased the resistance by 2 Ω. The difference between room temperature and 77 K should be 15 - 16 Ω. All resistors from the group now R = 204 ± 0.5 Ω turned out to be stable when the room temperature value was monitored for a few weeks. Some from the other groups with higher or lower R were drifting, down or up, by as much as 1 Ω. After mounting in a copper block (fig. 3.4) the thermometers were cycled a few times in liquid helium and tested for reproducibility of the 4.2 K value, which turned out to be better than 0.1 Ω at $R_{4.2} \approx 400\,\Omega$.

The mounting shown in fig. 3.4 is designed to provide a thermal anchoring of the electrical wiring, and at the same time to provide

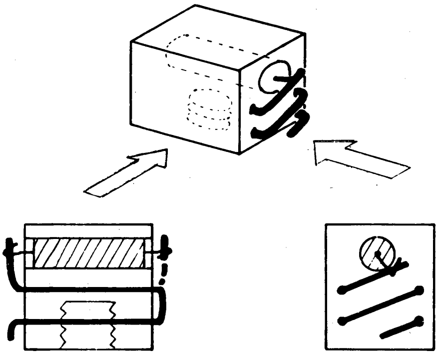

Fig. 3.4. A 200 Ω Matsushita resistor mounted in a copper block for use as a thermometer. Note the thermal anchoring of the leads very close to the resistor body.

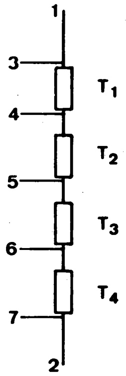

Fig. 3.5.A. A 'string' of 4 thermometers, for 4-terminal resistance measurements.
1, 2 current leads
3-7 voltage leads.

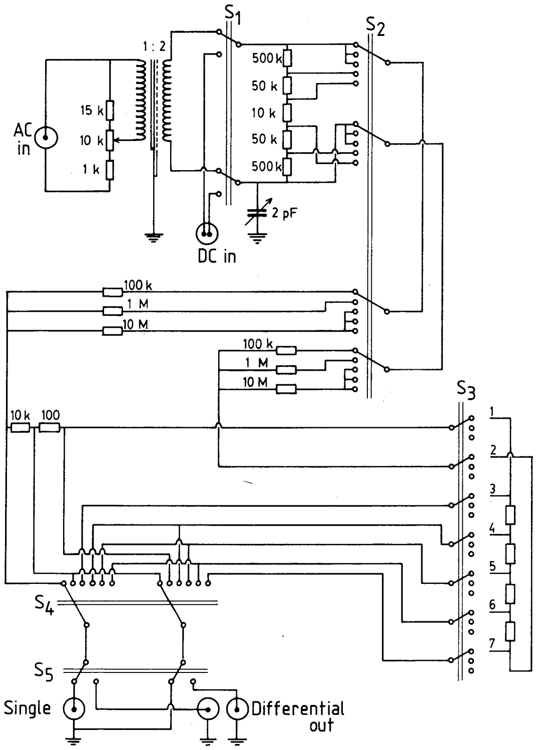

Fig. 3.5.B.

Circuit employed for 4-terminal resistance measurements on thermometer thermometer strings.

S_1 : AC/DC current
S_2 : range $10^{-9} - 10^{-5}$ A
S_3 : string selector
S_4 : thermometer selector calibration positions
S_5 : output Single Ended/ Differential.

thermal contact with the resistor body through its own leads. Copper wire with a thin enamel insulation is glued with cyano-acrylate glue in tight fitting holes, 1 mm diam. One end serves as the connection for the wiring, and the other end as a permanent connection to the resistor. On both ends Woods metal is used as low temperature solder, to prevent excessive heating. The resistor, from which the color code rings are ground off to allow for a better fit in its hole, is pressed in lightly with Apiezon N grease to improve thermal contact at higher temperatures. The copper block has a tapped hole (M3); the outside dimensions including wires do not exceed 10 x 6 x 8.5 mm^3.

The resistance measurements were done by the 4 lead method to eliminate the resistance of connecting wires. Usually up to 4 thermometers were connected in a 'string' with common current wires (fig. 3.5A). To economize on voltage wires, the current wires connecting the different thermometers were made with essentially zero resistance, either by short sections of copper wire, or by superconducting wire. The circuit of fig. 3.5B, completely enclosed in an aluminum box for screening of r.f. interference, gives the possibility of selecting currents 10^{-5}, 10^{-6}, 10^{-7}, 10^{-8}, 10^{-9} A. The current can be adjusted by measuring the voltage across one of two precision resistors, 100 Ω and 10 kΩ, internally connected in series with the string of thermometers. A lock-in amplifier is used as a voltage meter. Usually AC measurements at f = 22 Hz were done. Higher frequency could not be used, as the rather large capacitance between wires causes phase shifts between I and V. The wiring in this large cryostat is necessarily rather long. We use self-made 'flatcable' of copper wire, diam. 0.12 mm (exclusive of insulation) glued together with GE 7031 varnish. To reduce capacitive crosstalk effects, we separate the wires by including cotton thread of the same diameter in between, and we twist the current wires (by standard number 1 and 2 in a string) before including them in the flatcable (fig. 3.6). A total length of ~2.5 m is used from the top of the cryostat to the thermometers. The flatcable construction allows a compact way of anchoring a total of 30 wires to 4.2 K, 1.2 K and still-temperature. Short sections (2 cm) of 0.1 mm manganin wire were included between the 1.2 K pinning and still-temperature, and between still-temperature and

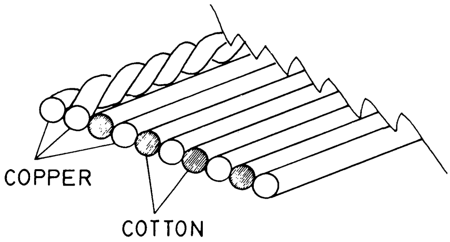

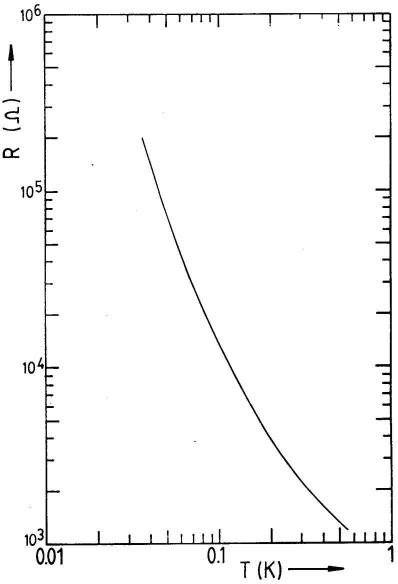

Fig. 3.6. ↑ *'Flatcable' of 0.12 mm copper wires, interspaced with cotton and impregnated with GE 7031 varnish.*

Fig. 3.7. → *R(T) curve for cell thermometer (200 Ω Matsushita).*

thermometers to reduce the heat load, but to keep the total resistance of the leads otherwise as low as possible.

A typical R(T) curve is shown in fig. 3.7. Typical values of maximum current allowed, to avoid self heating of the thermometers, are 10^{-9} A for $T < 100$ mK, 10^{-8} A for $T < 400$ mK and 10^{-7} A for $T > 400$ mK. The R(T) curve does not show any 'flattening' effect at the lowest temperature; thermometers of the same design but of lower nominal value (68 Ω), and measured with the same circuitry, show this effect only below $T \approx 20$ mK.

The calibration of the cell thermometer is transferred from two germanium resistors, that were calibrated in the same run. We have used as our standards:

1) ^{3}He vapor pressure thermometry,
2) Nuclear orientation thermometry (N.O.),
3) An NBS SRM 768 superconducting fixed point device.

Both germanium thermometers, the NBS device and the N.O. thermometer were mounted on the copper pole connecting the cell to the mixing chamber (fig. 3.2); the cell thermometer itself is outside on the bottom of the cell. Heating was always done above the highest thermometer to avoid thermal gradients.

^{3}He vapor pressure

Either the in-situ capacitive pressure gauge can be used, which has a linear $\Delta C/p$ response up to pressures $\sim 50 \times 10^{-3}$ Torr, or the room temperature Barocel pressure standard, in which case a correction for the thermomolecular effect[14] has to be made. Ultimately the in-situ pressure gauge is calibrated against the Barocel again, and its small signal sensitivity 6.70 pF/Torr is an extrapolation from higher pressures, where the thermomolecular pressure difference can be accurately calculated in a well defined geometry. We use the cold pressure gauge for the range 3×10^{-5} Torr (T = 213 mK) to 2.93×10^{-2} Torr (T = 402 mK). At $p = 2.39 \times 10^{-2}$ Torr we compare to the Barocel and find a thermomolecular pressure difference Δp_{th} of 1.63×10^{-2} Torr. This correction is assumed to be constant for the rest of a series of measurements with the Barocel in the range $p = 8.54 \times 10^{-2}$ Torr (460 mK) to 4.41×10^{-1} Torr (581 mK). We prefer the experimentally determined Δp_{th} instead of calculated values for the geometry of the H↓ experiment. This way the scales of the cold and the room temperature pressure gauges smoothly merge into each other. A calculation[14] shows that Δp_{th} would vary only weakly from $23 - 28 \times 10^{-3}$ Torr in the range $80 - 450 \times 10^{-3}$ Torr. Care was taken to verify that the vapor pressure was saturated. A small pool of liquid ^{3}He can be formed at the bottom of the cell. The thermal platform was heated to a temperature safely above that of the cell, to prevent condensation of ^{3}He on a 'cold spot' in the connecting line. The 1962 ^{3}He vapor pressure scale was used[16].

Nuclear Orientation Thermometry[17]

This type of thermometry, which becomes sensitive only below 100 mK, uses the anisotropy in gamma ray emission from ^{60}Co in an hcp ferromagnetic crystal of ^{59}Co at low temperatures where the nuclear spins align. Both the 1.17 and the 1.33 MeV peak in the γ-spectrum are counted with a 2"x2" NaI(Tl) scintillation detector and a multichannel analyzer. The data ara analyzed assuming a value for the hyperfine field $H_{hf} = -21.860$ T and hyperfine level splitting $\Delta / k_B = 6.0041$ mK[18]. A solid angle correction factor for our detector size and distance was applied. An isotropic count rate of ~95 c/s was found; because of Poisson statistics and the decreasing sensitivity at temperatures > 10 mK, 10 minute counting intervals give only moderate accuracy: typically $\Delta T = \pm 2.5$ mK at 36 mK and ±4 mK at 42.5 mK.

NBS SRM 768 Superconducting fixed point device[19]

This device contains 5 samples, of which we use 3, which make transitions to the superconducting state at temperatures roughly 100 mK, 160 mK and 200 mK (each unit is individually calibrated by NBS). The transition is measured by means of a change in mutual inductance between two coils, caused by the Meisner effect. Important is the strength of the magnetic field, which has two effects:

1) suppression of the transition temperature T_c to a lower value, and
2) the supercooling effect: a delayed transition to the superconducting state on lowering the temperature.

See fig. 3.8 and table 3.1. Both effects ΔT_c, ΔT_s are linear in magnetic field strength as long as $\Delta T_c, \Delta T_s \ll T_c(0)$. ΔT_s is directly visible as hysteresis; the correction ΔT_c can only be made when the

material	$T_c(B=0)$ [mK]	$\Delta T_c/B$ [mK/μT]	$\Delta T_s/B$ [mK/μT]
$AuIn_2$	204.75	0.08	0.48
$AuAl_2$	160.30	0.13	0.03
Ir	98.80	0.08	0.02

Table 3.1. Data for correction of transition temperatures in a magnetic field, taken from ref. 19.

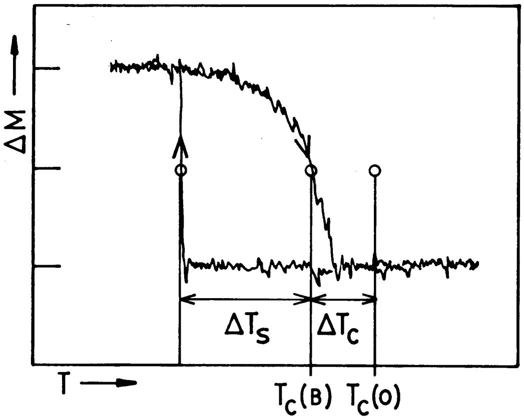

Fig. 3.8.

Registration of a transition to the superconducting state of a sample in the NBS fixed point device. Vertical is change in mutual inductance in arbitrary units. See text for explanation of ΔT_c, ΔT_s.

magnetic field is known. There is one sample ($AuIn_2$) that has a much larger ΔT_s than ΔT_c, from which one can measure the field B and apply the correction ΔT_c to the other transitions with help of table 3.1, and assuming the field to be homogeneous. To reduce the magnetic field two cylinders of mu-metal were placed around the NBS device, the outer of 'Telshield' and the inner of 'Cryoperm'. We found a residual field of 5.5 μT, i.e. about 1/10 of the earth's magnetic field. This is much larger than the value $\lesssim 1$ μT recommended by NBS for highest accuracy; on the other hand the corrections ΔT_c in our case remain below 1 mK which is more than adequate for our purpose.

At 204.3 mK for the NBS device, the temperature according to the ^{3}He scale was 206 ± 6 mK, so there is good agreement.

The data of ^{3}He vapor pressure and the NBS fixed point device were transferred to two germanium resistors. The data can be fit to a low order polynomial form $\log R = \sum_{i=1}^{n} a_i (\log T)^i$. The maximum relative difference between actual and fitted temperature was typically ~ 1 %, and the average of this quantity much better. A computer program was available to calculate the fits and to print tables for regularly spaced temperature intervals. The cell thermometer was calibrated against these two germanium resistors in the same run; the data from the NBS device and N.O. thermometry were directly transferred to the cell thermometer.

We believe our thermometry to be absolutely accurate to within +/- 3 mK in the range T = 200-300 mK, and +/- 1 % above 300 mK. In the range 100-160-200 mK we are essentially interpolating between these three NBS fixed points. The 'flexibility' of various fits through these points, with the imposed boundary condition of smooth transition to the $T < 100$ mK and $T > 200$ mK curves, indicates that in this interpolation region as well an accuracy of about +/- 3 mK is achieved.

We also need a calibration in high fields, B = 8 T. ^{3}He vapor pressure thermometry can be used again for T = 200-580 mK. For the lower temperatures we use a field cycling technique: a fixed amount of heating is applied to arrive at a steady state temperature in cell and mixing chamber. Then the B-field is turned on; after the heating effect of eddy currents has disappeared the resistance of the thermometer is read, and the field is reduced to zero again to check for reproducibility. This procedure, which takes up to ~ 1 hour for a complete cycle, yields reproducible results to within 1 mK. 200 Ω Matsushita's were found to have only a very weak (longitudinal) field dependence: $\Delta R/R = -10$ % for B: $0 \rightarrow 8$ T, T = 100 mK (corresponding to an apparent $\Delta T = +5.5$ mK). $\Delta R/R$ goes smoothly through zero at $T \approx 300$ mK, and $\Delta R/R = +5$ % at T = 500 mK (apparent $\Delta T = +30$ mK).

3.4. Results

Experiments were carried out to study the decay of H↓ as a function of temperature and ^{3}He-^{4}He composition. From these decay curves one can determine the adsorption energy of hydrogen on the surface. We also report on the first attempts to measure a long nuclear relaxation time, with a negative result. At this point it may be useful to mention in advance that this negative result was caused by an impurity effect (section 3.5). In later experiments[9] more insight has been gained in the criteria which the design of a stabilization cell should meet to avoid this impurity effect.

An example of a decay curve is shown in fig. 3.9. Readout of the pressure gauge was stored in a Nicolet 1174 signal averager, used as a digital recorder, and transmitted to a PDP 11 computer for further data

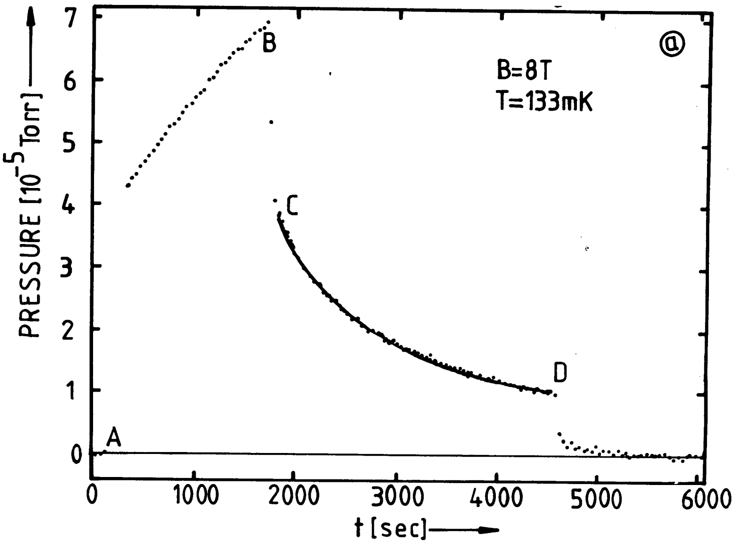

Fig. 3.9. Decay of H$\downarrow$ *on a* ^3He-^4He *(2:1) surface, measured with a pressure gauge.*

processing. The cell coating was prepared by admitting one standard 'shot' (28 μmol) ^{4}He to the system and twice this amount of ^{3}He. The filling flux of atoms is ~ 3×10^{12}/sec at T = 200 mK. This is about 1-2 orders of magnitude smaller than in the system used in ref. 7; the difference is attributed to the much higher present operating temperature of the HEVAC: 725 mK compared to ~ 500 mK. At A (fig. 3.9) the filling starts, after taking some baseline data; to save storage space the time base is held up at A to register only part of the filling curve. The filling is done at T = 200 mK in order to increase the starting density for decay at T = 133 mK. At C the observation of decay starts; the temperature is actively controlled. At D the sample is destroyed with the trigger bolometer. The discontinuity B-C corresponds to a (133/200) pressure ratio for the ideal H$\downarrow$ gas, plus a contribution from ^{3}He vapor pressure at 200 mK. The difference in zero of the pressure gauge at T = 200 mK and T = 133 mK was found to be

1.2×10^{-5} Torr, which corresponds to the saturated vapor pressure of pure ^{3}He at T = 200 mK.

To check for agreement with the earlier experiments on ^{4}He [7] we first did a measurement on pure ^{4}He (1 standard shot) at T = 330 mK, B = 8 T. We make a fit to a solution of the rate equation for combined 1st and 2nd order decay:

$$\frac{dn_V}{dt} = -\tau^{-1} n_V - K_s^{eff}\, n_V^2 \qquad (3.6)$$

and find $K_s^{eff}\sqrt{T} = 2.66\times10^{-19}$ cm^3/sec ± 18 %. This is somewhat smaller than the fit of ref. 7, but within a factor of two. It does not seem unreasonable, considering the spread in the measurements and the possibility of systematic differences. Presently we are not so much interested in an accurate absolute determination of K_s^{eff}, as well as in its temperature dependence to determine ε_a via eq. (3.4). No significant 1st order term (thermal leakage) was found, as expected: according to ref. 20

$$\tau = \frac{4V}{K\bar{v}O} \cdot c_M \quad ; \quad c_M = \exp(\tfrac{1}{2} g_e \mu_B \Delta B / k_B T) \qquad (3.7)$$

with V the volume of the cell, O the cross sectional area of the tube between cell and HEVAC; K the Clausing factor for this tube; $\bar{v}$ the average H atom velocity and c_M the magnetic compression factor. For our geometry $\tau = 1.6 \times c_M$ [sec] = 5.7×10^6 [sec]. The decay rate, $\tau^{-1} = 1.7\times10^{-7}$/sec, is to be compared with the initial decay rate due to second order recombination: $\frac{1}{n}\frac{dn}{dt} = -K_s^{eff}\, n = 4.6\times10^{-4}$/sec for an initial density $n = 10^{15}$/cm^3. Thermal leakage is thus completely negligible at $T \leqslant 330$ mK, B = 8 T.

As already explained in the introduction of this chapter, and demonstrated experimentally[7], small amounts of ^{3}He added to a film of ^{4}He have a large effect in reducing the adsorption energy ε_a. We wanted to investigate this further and added a large amount (2 standard shots) of ^{3}He to the ^{4}He which was already in the cell. Useful decay measurements were obtained in the range T = 113-196 mK at B = 8 T. The

1) The most rigorous one is to speed up the (surface) recombination by going to a temperature as low as possible, and to watch for decay to some finite density level instead of zero. Because the H↓ pressure at these low temperatures would be very difficult to measure, we chose the following procedure:
   The cell is loaded with pure ^{4}He. We fill at T = 400 mK to a density $5\text{x}10^{15}/\text{cm}^3$. Then we quickly cool the cell to T = 200 mK, and stabilize this temperature for 100 sec. Then we return quickly to T = 400 mK to observe how much H↓ is left by using the trigger bolometer. According to the data for K_s^{eff} and ε_a for H↓ on ^{4}He from ref. 7, extrapolated to T = 200 mK, the density should decay to $\sim 1/20$ of the initial $5\text{x}10^{15}/\text{cm}^3$ in 100 sec. To within experimental error we indeed observed 1/20 of the initial density; no more !
2) More generally one should see deviations from pure 2nd order decay. From ref. 12 we have the following rate equations:

$$\frac{dn_a}{dt} = -\ 2K_{aa}\ n_a^2 - K_{ab}\ n_a n_b - T_1^{-1}\ (n_a - n_b)$$

$$\frac{dn_b}{dt} = \qquad\qquad - K_{ab}\ n_a n_b + T_1^{-1}\ (n_a - n_b) \qquad (3.8)$$

   K_{aa}, K_{ab} are effective surface recombination rates. In general $K_{aa} \neq K_{ab}$. The rate equation for the total density $d(n_a+n_b)/dt$ can *only* be pure 2nd order $(\propto (n_a+n_b)^2)$ when the ratio n_a/n_b remains constant during the decay, which is the case either when $K_{aa} = 0$, or when T_1^{-1} is large (rapid relaxation; in that case $n_a/n_b = 1$). In particular one would expect that the rate of decay depends not only on the total density $n = n_a+n_b$, but also on the concentration ratio n_a/n_b, which depends on the previous (recombination) history of the sample. In these experiments we never observed 'historic' effects of this kind; all decays in this experiment both on pure ^{4}He and on ^{3}He-^{4}He mixtures could be described by pure 2nd order decay.

These measurements have been repeated later under various conditions. First we note the possible complication of ^{3}He impurities. ^{3}He atoms have a (small) magnetic moment and might be responsible for nuclear spin relaxation in H↓. At low enough temperatures ^{3}He impurities in small concentrations will build up at the surface of a ^{4}He film: they occupy the surface bound state (fig. 3.1). In our geometry 0.1 % impurity in the ^{4}He gas would be sufficient to provide a monolayer coverage of ^{3}He in the whole cell ! We have used isotopically purified ^{4}He, prepared by pumping superfluid helium through a Vycor glass superleak. We cannot establish the small ^{3}He concentration, but from the literature we infer a concentration $\sim 10^{-9}$, compared to natural helium $\sim 10^{-7}$. It had no effect on the rapid relaxation rates. Next we have coated the cell with a uniform layer of molecular hydrogen (H_2) or neon, several hundred Å thick, by slowly condensing these gases at suitable temperatures in the region of the HEVAC up to the cell. The purpose of these coatings was to bury possible microscopic magnetic impurities under a passive layer. All results were negative, possibly due to difficulties in applying a homogeneous coverage caused by temperature gradients.

From experiment 1) above we can conclude that either $K_{aa} \ll K_{ab}$ (if at $t = 0$ $n_a = n_b$ this does not have to be incompatible with a very long T_1 !), or that T_1 is very short. In the second explanation we can set an upper bound on T_1 with the following argument:
Under assumptions $n_a(0) = n_b(0)$, $K_{aa} = K_{ab}$, recombination first leads to an 'intermediate' state with $n_a = 0$, $n_b = \frac{1}{2}n_b(0)$, so $n = \frac{1}{4}n(0)$. This follows directly from eq. (3.8). After that, relaxation bottlenecked recombination can be shown to give 2nd order decay

$$\frac{dn_b}{dt} = - G\, n_b^2 \qquad (2n_b G = T_1^{-1}) \tag{3.9}$$

(Note that T_1^{-1} is proportional to the density, whereas G is a constant.) To explain a decay of another factor 5, to make up for a total factor 20 relative to the initial density, we arrive at a bound:

$$T_1 \lesssim 12 \text{ sec (at } n = \tfrac{1}{4} \times 5 \times 10^{15} = 1.25 \times 10^{15}/\text{cm}^3)$$

3.5. *Discussion*

We have measured ε_a of H↓ on ^{3}He-^{4}He mixtures. Let us characterize the surface coatings that can be achieved by these mixtures.

^{4}He superfluid films that creep up along metal walls from a pool of liquid, are known to have a thickness d according to ref. 22

$$d = 300/h^{1/3}\ [\text{Å cm}^{1/3}] \tag{3.10}$$

with h the height above the pool. This means for the film thickness in our sample cell, which is 10 cm above the HEVAC bottom, where a pool can form: d = 140 Å. A standard filling with 28 μmol ^{4}He corresponds to 7.7×10^{-4} cm^3 liquid ^{4}He; to cover the 32 cm^2 surface area in the cell with a 140 Å film we need only 4.5×10^{-5} cm^3. So there is really much more ^{4}He than what is needed to form a saturated film; the excess liquid will reside at the HEVAC reservoir.

As ^{3}He is added, this will subsequently move in the following places (we assume that the temperature is low enough to neglect the density of the vapor phase):

1) The surface bound states on top of the ^{4}He density profile will be occupied, until the coverage gets saturated at about one monolayer.
2) The next ^{3}He atoms will dissolve in the bulk ^{4}He; in the cell at T near 0 K up to a concentration 6.4 %, but in the HEVAC at T = 725 mK to much higher concentrations, ~ 40 %.
3) Still more ^{3}He atoms will build up at the surface monolayer. Formula (3.10) is derived by balancing the potential energy in the gravitational field (mgh) against the potential energy from the long range Van der Waals force from the substrate (α/z^3 ; z is the distance from the substrate). If we apply this principle to ^{3}He, we see that an extra layer of ^{3}He can be held on top of a saturated ^{4}He film;

$$\frac{d_{^3\text{He}}}{d_{^4\text{He}}} = \left[\frac{4}{3}\right]^{1/3} - 1 = 0.1 \qquad d_{^3\text{He}} = 14\ \text{Å}$$

   The 'size' (molar volume)$^{1/3}$ of a ^{3}He atom is ~ 3.9 Å , so the extra layer of ^{3}He can be ~ 3 - 4 atomic layers thick.
4) Still more ^{3}He will collect as bulk liquid in a reservoir at the lowest temperature, in this case the cell bottom (fig. 3.11).

It has been shown by Ellis et al.[23] that in thin films (~ 20 - 40 Å) of ^{3}He-^{4}He mixtures phase separation in a layered struction can indeed occur. This gives some confidence in the above model. Since the ^{3}He layer is expected to be about 4 atomic layers thick when enough ^{3}He is introduced to reach stage 3) mentioned before, there is problably only very little difference with a thick pure ^{3}He film as far as the effective potential for a H atom is concerned. We believe our result for ε_a to be representative also for a pure ^{3}He surface. It is therefore interesting to compare with the results of Jochemsen et al.[21] who measured the adsorption energy of H (in zero field) on films of pure ^{3}He. In this closed geometry experiment they do not need the superfluid properties of the film, so they can use pure ^{3}He. They find $\varepsilon_a/k_B = 0.42 \pm 0.05$ [K]. This is somewhat surprising; if one would expect any difference at all, the value for mixtures should be higher than for pure ^{3}He.

Concerning the rapid nuclear relaxation rates, it is now known from later experiments[9,8,10] that these were caused by an impurity effect, i.e. microscopic or macroscopic magnetic particles at the cell walls cause relaxation of the nuclear spin when a single H atom, adsorbed in the 2-D phase, 'collides' with these. In the cell of Sprik et al.[9] great care was taken to keep the cell absolutely free from ferromagnetic

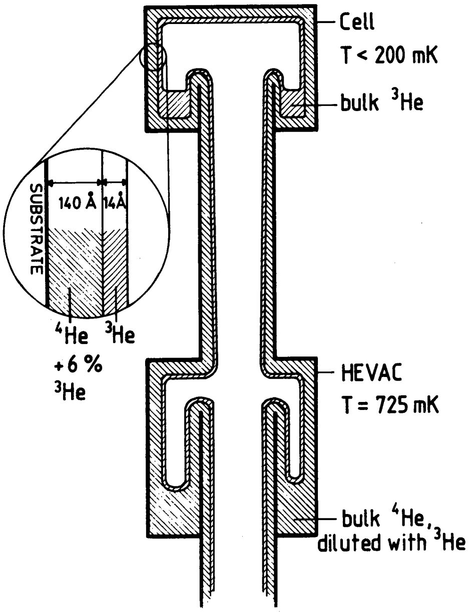

Fig. 3.11.

Schematic distribution of ^{3}He and ^{4}He in Cell and HEVAC.

materials. Even so, with thin helium films there was still an extra impurity relaxation present, which could however be suppressed by working with a larger amount of helium. This is a clear demonstration that we have to do with microscopic impurities in this case; the effect of the thick helium film is to keep the H atoms sufficiently far away from the dipolar fields to suppress relaxation by these field in inhomogeneities. In later experiments[8,9,10] the intrinsically long T_1's predicted by Statt and Berlinsky have indeed been observed, both on ^{4}He and on ^{3}He-^{4}He mixtures ! The situation is more complicated however, because at low temperatures there is also a contribution from dipolar relaxation in binary collisions between H atoms in the 2-D phase.

As an illustration, we finally interpret the rapid $T_1 = 12$ sec found in this experiment (at $T = 0.2$ K, $n = 1.25 \times 10^{15}/\mathrm{cm}^3$) in two simple models for impurity relaxation:

1) H atoms, moving with speed $\bar{v}_2$ in the 2-D phase 'collide' with impurity particles. The impurity particles are of size d and are on fixed sites at the surface; they occur in a concentration n_i. In order for the relaxation to be effective, there is an optimum size for these particles: $d \approx \bar{v}_2 / \omega$ (the reciprocal transient time $\bar{v}_2/d$ must equal the NMR angular frequency). What is observed in the bulk is an effective surface rate $(\frac{1}{T_1})^{\mathrm{eff}}$ defined by:

$$\left(\frac{1}{T_1}\right)^{\mathrm{eff}} = \left(\frac{1}{T_1}\right) \frac{A}{V} \lambda \exp\left(\varepsilon_a/k_B T\right) \tag{3.11}$$

(this is analogous to the effective surface recombination rates defined by eq. (3.4), but we have a 1 body H process here). In this model $\frac{1}{T_1} = n_i \bar{v}_2 \sigma_i$ (independent of the density of H↓), with n_i the concentration of impurities, and $\sigma_i = 2d$ a 2-D cross section. Using $(\frac{1}{T_1})^{\mathrm{eff}} = 1/12$ sec^{-1} we find for the size of the impurity particles $d \approx 8 \times 10^{-7}$ cm or ≈ 80 Å and a coverage $n_i \approx 1.6 \times 10^4$ cm^{-2}. The 80 Å size seems a bit small; a thick helium film should be able to cover these. On the other hand the concentration n_i is very low for microscopic particles; a combination of larger particles and a higher concentration could be just as effective.

2) If there is one 'dirty spot' in the cell where the spins relax with

100 % probability as soon as atoms collide with this surface, then T_1 essentially can be calculated from the average time it takes for an atom to reach this this surface. If this dirty spot has area a, the number of collisions per sec is $\frac{1}{4}\, n\, \bar{v}_3\, a$ and the relaxation rate is $\frac{1}{T_1} = \frac{1}{4}\, n\, \bar{v}_3\, a \,/\, n\, V$. So we can estimate the area of such a spot: $a = 4\, V \,/\, \bar{v}_3\, T_1 = 9 \times 10^{-5}\ \mathrm{cm}^2$. Even a size of order $100 \times 100\ \mu\mathrm{m}^2$ would be enough to explain the rapid T_1.

Both models can give a reasonable explanation; we see that it is important to avoid both macroscopic *and* microscopic magnetic material in a cell.

References of chapter 3

1. I.F. Silvera and J.T.M. Walraven, Phys. Rev. Lett. 44, 164 (1980).
2. I.B. Mantz and D.O. Edwards, Phys. Rev. B20, 4518 (1979).
3. R.A. Guyer and M.D. Miller, Phys. Rev. Lett. 42, 1754 (1979).
4. D.O. Edwards and I.B. Mantz, Journal de Physique 41, C7-257 (1980).
5. I.F. Silvera and V.V. Goldman, Phys. Rev. Lett. 45, 915 (1980).
6. M. Morrow, R. Jochemsen, A.J. Berlinsky and W.N. Hardy, Phys. Rev. Lett. 46, 195 (1981); 47, 455 (1981).
7. A.P.M. Matthey, J.T.M. Walraven and I.F. Silvera, Phys. Rev. Lett. 46, 668 (1981).
8. R.W. Cline, T.J. Greytak and D. Kleppner, Phys. Rev. Lett. 47, 1195 (1981). ε_a/k_B (H↓ on ^{4}He) = 1,01 ± 0.06 K
9. R. Sprik, J.T.M. Walraven, G.H. van Yperen and I.F. Silvera, Phys. Rev. Lett. 49, 153 (1982). ε_a/k_B (H↓ on ^{4}He) = 0.89 ± 0.06 K
10. B. Yurke, J.S. Denker, B.R. Johnson, N. Bigelow, L.P. Lévy, D.M. Lee and J.H. Freed, Phys. Rev. Lett. 50, 1137 (1983). ε_a/k_B (H↓ on ^{4}He) = 1.06 ± 0.04 K
11. I.F. Silvera and J.T.M. Walraven, Phys. Rev. Lett. 45, 1268 (1980).
12. B.W. Statt and A.J. Berlinsky, Phys. Rev. Lett. 45, 2105 (1980).
13. Barocel Model 1173 electronic manometer with 570A-1000T-2A1-V12 head (Datametrics Inc.).
14. T.R. Roberts and S.G. Sydoriak, Phys. Rev. 102, 304 (1956).
15. Matsushita ERC - 18 SGJ, obtained from S.H.E., Maria Theresia Allee 22, D-5100 Aachen, West Germany.
16. D.S. Betts, *Refrigeration and Thermometry below one Kelvin*, (Sussex University Press, 1976) Ch. 7, p. 168.
17. P.M. Berglund, H.K. Collan, G.J. Ehnholm, R.G. Gylling and O.V. Lounasmaa, Journal of Low Temperature Physics 6, 357 (1972).
18. Chrystal and data supplied by Oxford Instruments, Oxford, England. The hyperfine field includes a correction for demagnetization factor for this sample.
19. NBS Special publication 260-62, april 1979.
20. J.T.M. Walraven and I.F. Silvera, Phys. Rev. Lett. 44, 168 (1980).

21. R. Jochemsen, M. Morrow, A.J. Berlinsky, and W.N. Hardy, Phys. Rev. Lett. 47, 852 (1981).
22. J. Wilks, *The properties of liquid and solid helium*, (Clarendon, Oxford 1967) Ch. 14, p. 407.
23. F.M. Ellis, R.B. Hallock, M.D. Miller, and R.A. Guyer, Phys. Rev. Lett. 46, 1461 (1981).

CHAPTER IIII A STUDY OF DOUBLY POLARIZED ATOMIC HYDROGEN BY ELECTRON SPIN RESONANCE

4.1. Introduction

In this chapter we present an extensive description of a study of spin-polarized atomic hydrogen (H↓) by means of electron spin resonance (ESR) in an intense magnetic field[1]. Because the H atom possesses both an electronic and a nuclear magnetic moment ($I = S = \frac{1}{2}$), magnetic resonance seems a very useful detection technique. ESR provides an attractive, direct technique of probing the detailed properties of H↓. H↓ is a gas consisting of atoms in the lower two (electron spin 'down',↓) of the four hyperfine states shown in fig. 4.1 : the ground a- and the b-state, which in the high field limit differ by the projection of the nuclear spin. ESR allows the direct measurement of the population of these two hyperfine levels. In previous experiments this information had to be derived indirectly from density decay measurements using a pressure gauge. A process called relaxation bottlenecked recombination, predicted by Statt and Berlinsky[2], in which the a-state atoms are preferentially depleted from the gas by recombination under conditions of slow nuclear relaxation, enables one to obtain both electron and nuclear spin-polarized, or doubly polarized hydrogen (H↓⤓). The signal strength of two ESR transitions allows the growth of the nuclear polarization to be monitored in time. Moreover a detailed study of the time evolvement of the state densities permits a determination of the microscopic recombination and relaxation rate constants. In conjunction with pressure measurements an ESR study, yielding the density n, can provide information concerning the temperature T of the gas, by making use of the low density equation of state $p = nk_BT$. This is of particular importance in efforts to achieve Bose-Einstein Condensation (BEC), as the large release of recombination energy in combination with a possible serious Kapitza thermal boundary (gas-liquid) resistance can result in large deviations from thermal equilibrium. ESR can also be used as a direct means of observing BEC as proposed by Walraven and Silvera[3]. In an inhomogeneous field the spatial density distribution of H↓ is projected onto the ESR lineshape. With the aid of special magnetic field profiles the characteristic density profile in the Bose condensed state[4] can be observed. In our measurements we demonstrate that ESR in an inhomogeneous field can be used to eject atoms out of the high field region. Such techniques have been considered as a means of injecting a double polarized gas of H into the target region for proton scattering experiments at CERN, or as a means of feeding the accelerator beam itself in an efficient way with polarized protons[5]. Finally, the ESR experiment described here could without modifications be used to study deuterium, D↓. It is of interest to know whether the same process of relaxation bottlenecked recombination can be used to prepare a state of nuclear polarization in D↓. Such a nuclear polarized state would in principle be very attractive for nuclear fusion reactors if the gas could be injected in the plasma[6].

The first experiments on stabilized H↓ were performed with a destructive technique, in which the released energy of recombination was measured calorimetrically. Subsequently more sophisticated measurement techniques have been developed, and considerable progress has been made in the understanding of the processes that determine the lifetime and limiting densities of H↓ samples. A review on these developments is given by Silvera[7]; see also section 1.2 of this thesis. Concerning magnetic resonance: NMR studies of H have been performed in low (6.5 kG) and zero magnetic field at low densities. This has been reviewed by Hardy, Morrow, Jochemsen and Berlinsky[8]. Recently NMR has been introduced as a detection technique for high field (8.3 T) stabilized H↓ at Cornell[9]. In addition to our experiment, low field ESR measurements have been carried out by Mayer, Ridner and Seidel[10], as well as high field work by Statt and Hardy[11].

This chapter is organized as follows. In section 4.2 the relevant theory of ESR in H↓ is discussed. The experimental apparatus is described in section 4.3. In section 4.4 we discuss in some detail the subtle problems encountered and techniques used for measuring ESR lines in H↓. Results of a study of some properties of the H↓ gas are presented in section 4.5.

4.2. Theory of ESR transitions in H↓

The H atom in a static magnetic field, chosen along the z-axis, is described by the Hamiltonian

$$\mathcal{H} = \hbar\gamma_e B S_z - \hbar\gamma_p B I_z + a\vec{I}\cdot\vec{S} \tag{4.1}$$

with $S = \frac{1}{2}$, $I = \frac{1}{2}$. The first term is the electronic Zeeman term; $\gamma_e \equiv g_e\mu_B/\hbar$ with μ_B the Bohr magneton. The second term is the nuclear Zeeman term; $\gamma_p \equiv g_N\mu_N/\hbar$ with μ_N the nuclear magneton and g_N the g-value for a free proton. The third term is the hyperfine interaction with strength a. We shall characterize the spin $\frac{1}{2}$ states by the spin projections : $|m_S,m_I\rangle = |\text{↑⇞}\rangle, |\text{↑⇟}\rangle, |\text{↓⇞}\rangle, |\text{↓⇟}\rangle$. By diagonalizing the matrix of Hamiltonian eq. (4.1) with respect to a basis set of the four product states, one finds the eigenstates and eigenvalues for the energy. The result is shown in fig. 4.1. The eigenstates or hyperfine levels are labeled a,b,c,d in order of increasing energy, and

$$\begin{aligned}
|d\rangle &= |\text{↑⇞}\rangle \\
|c\rangle &= \cos\theta\,|\text{↑⇟}\rangle + \sin\theta\,|\text{↓⇞}\rangle \\
|b\rangle &= |\text{↓⇟}\rangle \\
|a\rangle &= -\cos\theta\,|\text{↓⇞}\rangle + \sin\theta\,|\text{↑⇟}\rangle
\end{aligned} \tag{4.2}$$

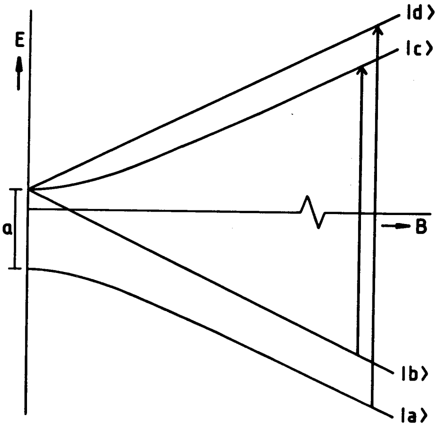

Fig. 4.1.

The hyperfine level diagram of a single H atom in a magnetic field B. The arrows indicate the ESR transitions that are allowed in high field

The wavefunction mixing parameter θ is defined by

$$\sin\theta \equiv \left[1 + \left\{ \frac{\mu^+ B}{a} + \left(1 + \left(\frac{\mu^+ B}{a}\right)^2 \right)^{1/2} \right\}^2 \right]^{-1/2} \tag{4.3}$$

with $\mu^{\pm} \equiv g_e\mu_B \pm g_N\mu_N$. In the limit of high fields, where $\frac{\mu^+ B}{a} \gg 1$ or $B \gg 0.05$ T, this is often approximated by identifying the small parameter ε with $\sin\theta$:

$$\varepsilon = \sin\theta \approx a/(2\mu^+ B) \tag{4.4}$$

so :

$$\begin{aligned} |d\rangle &= \ |\uparrow\text{⇞}\rangle \\ |c\rangle &= \ |\uparrow\text{⇟}\rangle + \varepsilon|\downarrow\text{⇞}\rangle \\ |b\rangle &= \ |\downarrow\text{⇟}\rangle \\ |a\rangle &= -|\downarrow\text{⇞}\rangle + \varepsilon|\uparrow\text{⇟}\rangle \end{aligned} \tag{4.2$'$}$$

The expressions for the energy are :

$$\begin{aligned} E_d &= a/4\ [\,1 + 2\mu^- B/a\,] && \approx a/4 + \mu^- B/2 \\ E_c &= -a/4\ [\,1 - 2\sqrt{1 + (\mu^+ B/a)^2}\,] && \approx -a/4 + \mu^+ B/2 \\ E_b &= a/4\ [\,1 - 2\mu^- B/a\,] && \approx a/4 - \mu^- B/2 \\ E_a &= -a/4\ [\,1 + 2\sqrt{1 + (\mu^+ B/a)^2}\,] && \approx -a/4 - \mu^+ B/2 \end{aligned} \tag{4.5}$$

At the experimental field $B \approx 6$ T some values are: $(E_d - E_a)/k_B = 8.1$ K and $(E_b - E_a)/k_B = 46.5$ mK. Because of the enormous Boltzmann factor $\exp(\Delta E/k_B T)$ it is clear that at temperatures of say $T = 300$ mK, the states 'c' and 'd' cannot be thermally populated. Since H↓ is a mixture of a- and b-state atoms, it is only (electron)spin-polarized to the extent that the mixing parameter ε is small. In finite fields full (electronic and nuclear) spin-polarization can only be realized in a sample which consists of b-state atoms only.

To perform a magnetic resonance experiment we apply a linearly polarized oscillating magnetic field in a direction perpendicular to the static field. The Hamiltonian is then

$$\mathcal{H} = \mathcal{H}_0 + \mathcal{H}_1(t) \tag{4.6}$$

where $\mathcal{H}_0$ is the Hamiltonian of eq. (4.1) and

$$\begin{aligned}\mathcal{H}_1(t) &= \hbar\gamma_e \vec{S}\cdot\vec{B}_\perp(t) - \hbar\gamma_p \vec{I}\cdot\vec{B}_\perp(t)\\ &= 2\hbar(\gamma_e S_x - \gamma_p I_x)B_1\cos\omega t \equiv 2V\cos\omega t \qquad (4.7)\end{aligned}$$

We choose $\vec{B}_\perp$ along the x-direction and it is given, by convention, an amplitude $2B_1$. In large static fields $\mathcal{H}_1(t)$ can be treated as a small perturbation, and standard time-dependent perturbation theory can be used to calculate the transition rates

$$\begin{aligned}W_{i\leftrightarrow f} &= \frac{2\pi}{\hbar}\,|\langle f|V|i\rangle|^2\,\delta(\hbar\omega - |E_f - E_i|)\\ &= B_1^2\,|\langle f|\gamma_e S_x - \gamma_p I_x|i\rangle|^2\,\delta(\nu-\nu_0) \qquad (4.8)\end{aligned}$$

with $\nu_0 = |E_f - E_i|/h$. The transition rates are easily found :

$$\begin{aligned}W_{a\leftrightarrow d} &= \frac{1}{4}B_1^2\,(\gamma_e + \varepsilon\gamma_p)^2\,\delta(\nu-\nu_{a\leftrightarrow d}) \qquad (4.9)\\ W_{b\leftrightarrow c} &= \frac{1}{4}B_1^2\,(\gamma_e - \varepsilon\gamma_p)^2\,\delta(\nu-\nu_{b\leftrightarrow c})\\ W_{a\leftrightarrow b} &= \frac{1}{4}B_1^2\,(\gamma_p + \varepsilon\gamma_e)^2\,\delta(\nu-\nu_{a\leftrightarrow b})\\ W_{c\leftrightarrow d} &= \frac{1}{4}B_1^2\,(\gamma_p - \varepsilon\gamma_e)^2\,\delta(\nu-\nu_{c\leftrightarrow d})\end{aligned}$$

The first two transitions are almost pure electron spin transitions (ESR) and are the subject of this chapter; the last two are nuclear spin transitions (NMR). The ratio $W_{a\leftrightarrow d}/W_{b\leftrightarrow c} \approx 1 + 4\varepsilon\gamma_p/\gamma_e = 1.0000256$ (at $B = 6$ T) can for all practical purposes be taken as one. The transitions d↔b and c↔a, which would mean a simultaneous electron and proton spin flip, are forbidden to first order. If the field $2B_1\cos\omega t$ were directed along the z-axis, the only allowed transition turns out to be a↔c, with

$$W_{a\leftrightarrow c} = \varepsilon^2 B_1^2\,(\gamma_e + \gamma_p)^2\,\delta(\nu - \nu_{a\leftrightarrow c}) \qquad (4.10)$$

This so called longitudinal resonance transition however would be a factor $4/\varepsilon^2 = 2.25\times10^5$ weaker than the transverse ESR transitions of eq. (4.9). The approximate expressions for the relevant transition frequencies are :

$$\begin{aligned}\nu_{a\leftrightarrow d} &\approx \tfrac{1}{2}\, a/h + g_e\mu_B B/h \\ \nu_{b\leftrightarrow c} &\approx -\tfrac{1}{2}\, a/h + g_e\mu_B B/h \end{aligned} \qquad (4.11)$$

The frequencies are those of the free electron, displaced by $\pm\frac{1}{2}\,a/h = \pm\,710$ MHz . Eq. (4.11) breaks down of course in the limit of low B, but by expanding the square roots we see that the error made at $B = 6$ T is only of order $\varepsilon\,\frac{1}{2}\,a/h = 3$ MHz compared to $\nu_{a\leftrightarrow d} = 167$ GHz. At constant field the two transitions are separated in frequency by a/h (this result also holds for the exact expressions in eq. (4.5)). At constant frequency the transitions are separated in field by $a/g_e\mu_B = 506.84$ gauss, but this expression is only valid in the high field limit.

Next we use the transition probabilities (4.9) to calculate the microwave power absorption. In the experiment we will measure the single pass transmission of microwave power in a hydrogen sample with geometry shown in fig. 4.2. The hydrogen atoms are confined in the tube by the static magnetic field gradient which exerts a force on the electron magnetic moments. The density distribution n(z) is schematically indicated in fig. 4.2. Here n(z) represents the density of either the a- or the b-state, n_a or n_b. Axial symmetry is assumed, and we consider

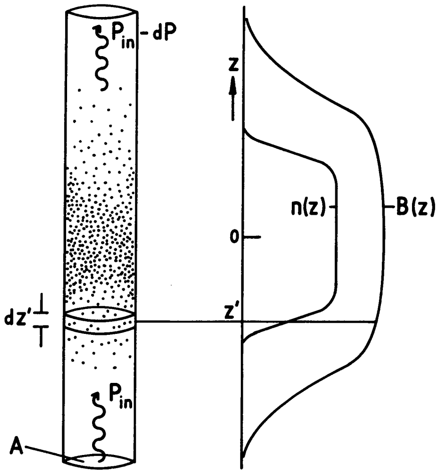

Fig. 4.2.

Geometry of the H↓ *sample used for calculation of the absorption coefficient. The field- and density profiles are also indicated.*

the dependence of n and B on z only. The microwave power is assumed to propagate in the z-direction as a linearly polarized plane wave of amplitude $2B_1\cos\omega t$. The cycle averaged Poynting vector $\overline{\vec{S}} = \frac{1}{\mu_0}\overline{\vec{E}\times\vec{B}} = \frac{c}{\mu_0}4\,\overline{B_1^2\cos^2\omega t} = \frac{2c}{\mu_0}B_1^2$ is the intensity, and the power P_{in} available in the incoming beam relates to the amplitude $(2B_1)$ as

$$P_{in} = \frac{2c}{\mu_0}B_1^2\,A \tag{4.12}$$

where A is the cross sectional area of the tube. Consider first the a→d transition of the atoms in a disk of infinitesimal thickness dz' located at z' . The number of atoms in the a-state in this disk is $n_a(z')\,Adz'$. The power absorbed from the incoming radiation is

$$dP = W_{a\rightarrow d}\,h\nu\,n_a(z')\,A\,dz' \tag{4.13}$$

Since the upper level (d) is not populated there is no (stimulated) emission of radiation. The process is locally described by an absorption coefficient α' (dimension: cm^{-1}) defined by $P_{out}/P_{in} = \exp(-\alpha' dz')$ or $\alpha'(\nu,z') = dP/P_{in}/dz'$. By making use of eqns. (4.9) and (4.12) we find

$$\alpha'(\nu,z') = \frac{\mu_0}{8c}(\gamma_e+\varepsilon\gamma_p)^2\delta(\nu-\nu_{a\rightarrow d}(z'))\ h\nu\,n_a(z')\ dz' \tag{4.14}$$

We want to describe the total effect of one pass of the radiation through the whole sample by a (dimensionless) quantity, the absorption $\alpha(\nu)$ such that $P_{out}/P_{in} = \exp(-\alpha)$; by definition $\alpha(\nu) \equiv \int dz'\,\alpha'(\nu,z')$. Since $\nu_{a\rightarrow d} \approx \gamma_e B/(2\pi)$ and $B(z) \approx B(z') + (\frac{dB}{dz})_{z=z'}\cdot(z-z')$ we can rewrite the argument of the deltafunction in eq. (4.14) :

$$\delta(\nu-\nu_{a\rightarrow d}(z')) = \frac{2\pi}{\gamma_e(\frac{dB}{dz})_{z=z'}}\ \delta(z-z')$$

After integration of α' over the whole sample we get

$$\alpha(\nu) = \frac{\pi\mu_0}{4c}(\gamma_e+\varepsilon\gamma_p)^2\,\frac{h\nu}{\gamma_e}\,\left(\frac{dB(z)}{dz}\right)^{-1}\,n_a(z) \tag{4.15}$$

with z chosen such that B(z) satisfies the resonance condition eq. (4.11).

If there is more than one such value of z, eq. (4.15) should be summed over each of these values. A similar expression holds for the $b \rightarrow c$ transition. The physical picture is that the radiation of a certain frequency is on resonance with atoms in a layer whose thickness is inversely proportional to the gradient of the local resonance frequency. Of course this picture breaks down when $\frac{dB}{dz} = 0$, because the termination of the Taylor expansion for B(z) after the first order term is then invalid. One can get around this difficulty in two ways :

1) There will always be transverse field gradients that will spread out the infinitely high and sharp absorption peak which occurs where an extremum or horizontal inflection point exists in the field profile B(z), and
2) The intrinsic linewidth (T_2^{-1}) is finite instead of being zero as implied by the use of the delta-function in eq. (4.8). Possible sources of line broadening in ESR experiments have been reviewed by Yurke et al.[12]. They consider (possibly motionally narrowed) Doppler shift, spin exchange, interatomic spin dipolar interactions, and radiation damping. The conclusion is that radiation damping will make by far the largest contribution to the linewidth in a CW absorption experiment. This conclusion remains valid, even though their calculation for dipolar linewidth was based on a diffusion model, which is inapplicable for densities $\lesssim 10^{19}/\mathrm{cm}^3$ and should be replaced by a binary collision model[12].

Radiation damping will give a Lorentzian lineshape with FWHM of $2\tau_{RD}^{-1} \approx 2 \times 10^{-12}\ n_i\ [\mathrm{cm}^3/\mathrm{s}]$ with n_i $(i = a,b)$ the density of one hyperfine component. Instead of eq. (4.15) we then have the expression

$$\alpha(\nu) = \frac{\mu_0 h\nu}{4c} (\gamma_e + \varepsilon\gamma_p)^2 \int dz' n_i(z') \frac{\tau(z')}{1 + 2\pi\tau(\nu - \nu(z'))} \quad (4.16)$$

where $\tau = \tau_{RD}$ is a function of z' because it depends on the local density $n_i(z')$. Eq. (4.16) can be used for numerical lineshape simulations. It does not exhibit any divergence for $\frac{dB}{dz} = 0$ as can be seen in the following example. Consider a sample in an ideal homogeneous field, of finite length d. After integration of eq. (4.16) we see that there is a maximum absorption :

$$\alpha_{max} = \frac{\pi\mu_0 h\nu}{4c} (\gamma_e + \varepsilon\gamma_p)^2 \, n_a \, d \frac{\tau}{\pi} \qquad (4.17)$$

In this case of a homogeneous field the absorption coefficient α' (with dimension: cm^{-1}) is a useful quantity :

$$\alpha'_{max} = \frac{\pi\mu_0 h\nu}{4c} (\gamma_e + \varepsilon\gamma_p)^2 \, n_a \frac{\tau}{\pi} \qquad (4.18)$$

This result corresponds, after conversion to Gaussian units, to eq. (3) of Yurke et al.[12]. Their absorption is a factor 2 higher and was apparently taken for the case of circularly polarized radiation.

The conclusion of all this is, that for densities $\gtrsim 10^{15}/cm^3$ and a homogeneous field, one observes a Lorentzian line with a width proportional to the density, but of constant peak height. This however would require an effective field homogeneity $\Delta B/B \approx 2 \times 10^{-9}$ even for the very high density $n_a = 10^{18}/cm^3$. Moreover one would have to work with a very thin sample ($\lesssim 0.1$ mm) in order to prevent the sample from becoming 'optically black' exactly on resonance. In the more realistic situation of our experiment we have $\Delta B/B = 10^{-5}$ in a 1 cm diameter defined spherical volume. This means that eq. (4.15) is applicable. The peak height at the field maximum will be finite, and its height can be estimated as follows: replace $\frac{dB}{dz}$ by $\frac{\Delta B}{\Delta z}$. This implies that the full inhomogeneity $\Delta B = 10^{-5}$ B is encountered over the cross section of the tube. Because of the transverse gradient which has been ignored so far, it does not make sense to think of regions smaller than 1 cm in the z-direction. For B = 6 T and $n_a = 10^{16}/cm^3$ we find $\alpha_{max} = 0.107$ or ~ 11 % power absorption. This of course is only a crude estimate, and measured peak heights cannot be used accurately as absolute measure for the density $n_a(0)$. A better measure in this respect is the integrated absorption $\int\alpha(\nu)d\nu$. Since a resonance line is usually measured by working at constant frequency and using a homogeneous sweep field, we will instead calculate $\int\alpha(B)dB$:

$$\int_{B_2}^{B_1} \alpha(B)\,dB \Big/ \left[\frac{\pi\mu_0 h\nu}{4c\gamma_e} (\gamma_e + \varepsilon\gamma_p)^2\right] = \int_{B_2}^{B_1} \frac{n_a(z)}{\frac{dB}{dz}} \, dB = N_a/A \qquad (4.19)$$

The integrated absorption thus measures the total number of atoms N_a present between two limits z_2 and z_1, which in our case would be the limits of the density distribution.

Returning to eq. (4.15) we see that the spatial density distribution $n_a(z)$ reflects itself in the lineshape $\alpha(\nu)$, however in a complicated way because 1) the relationship between ν and z is non-linear, and 2) the factor $\frac{dB}{dz}$ is involved.

Both objections would disappear when $\frac{dB}{dz}$ can be made constant over a wide range, so that the lineshape (measured either as a function of frequency or of magnetic field) will be an undistorted image of the density distribution. The importance of this lies in the predicted peaking effects in the density distribution of a Bose-condensed atomic hydrogen sample in an inhomogeneous field[3,4,13].

Finally we note that ESR detection of H atoms can be destructive for the sample. c- and d-state atoms (with electron spin 'up') are driven out of the sample cell by the magnetic field gradient. This gives rise to a first order decay process, the time constant given by

$$\tau_{rad}^{-1} = -\frac{1}{N}\frac{dN}{dt} = \frac{\alpha P}{Nh\nu} \approx \frac{\pi\mu_0}{4c}\gamma_e \left(\frac{dB}{dz}\right)^{-1} \frac{P}{Al_{eff}} \qquad (4.20)$$

with N the total number of atoms in the density distribution in a particular hyperfine state, and l_{eff} an effective sample thickness defined by $l_{eff} = \int dz\, n(z)/n(0)$. Note that τ_{rad} is independent of the density. For example, in our system $Al_{eff} \approx 2$ cm^3 and $\Delta B/\Delta z \approx 0.6 \times 10^{-5}$ [T/cm]. At $n = 10^{16}$/cm^3 the maximum absorption $\alpha_{max} = 0.107$, and for $\nu = 156$ GHz and $P = 0.1$ μW, $\tau \approx 200$ sec. Actually the loss of atoms could be twice as large, if the spin-flipped atoms do not escape but condense on the surface of the cell and subsequently recombine into H_2. This will depend in a complicated way on the mean free path in the gas, the sticking coefficient and the recombination rate constant. It is clear that working at a power level $\leqslant 0.1$ μW and/or the use of very short sweeps is necessary to avoid the situation that the measurement technique itself is the dominant decay process.

The numbers calculated above explain our choice of a single-pass absorption cell instead of a tuned cavity: in a reasonably homogeneous magnetic field narrow lines with a ~ 10 % peak power absorption are to be expected, which should be easily detectable. There is thus no need for a high-Q cavity to enhance the absorption, nor is this even desirable since the microwave power in the sample is to be kept at a very low level. A high sensitivity can only be realized by means of a sensitive detector.

4.3. Apparatus

The experiment was carried out in a dilution refrigerator (Oxford Instruments) with a maximum cooling power of 500 μW at 100 mK and an unloaded base temperature of 5 mK. This cryostat has no cryogenic fluids in the lower parts, but has demountable tails as cold radiation shields. This construction makes the experimental space below the mixing chamber easily accessible. The refrigerator was adapted to incorporate a 7.5 Tesla coil with 1 : 10^5 homogeneity. Thermal pinning provisions were made for cooling the hydrogen which is loaded from the bottom, as shown schematically in fig. 4.3. Details will be clarified in additional figures.

To perform ESR we choose for a single pass FIR (far infrared) absorption scheme in which our usual filling geometry could serve, with minor modifications, as light pipe optics to guide the radiation. In this geometry a sample cell is loaded from the bottom through a vertical fill line, the H being produced in a room temperature discharge. The distance between the source (= discharge) and the final H stabilization cell is kept as short as possible, i.e. as short as is compatible with the temperature differences between the various cooling stages. The sample space itself is made rather long so that 94 % of the maximum field is used for magnetic compression of the gas of hydrogen[3,14]. See ref. 15 for a description of this cell and loading system and ref. 7 for a later version, incorporated in a dilution refrigerator. See also fig. 1.6 of this thesis for a schematic figure of the ESR cell. An advantage of the FIR broadband design (as compared to a high-Q cavity) is that it can in principle be operated at any frequency, so it leaves

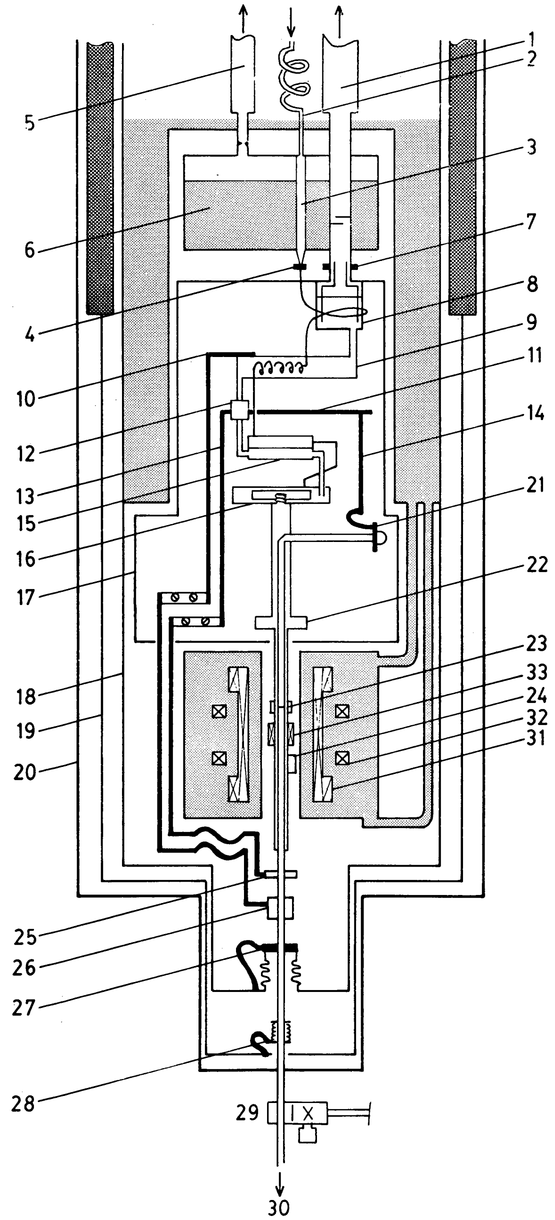

1 ^{3}He pumping line
2 ^{3}He return line
3 ^{3}He condenser
4 flow impedance
5 ^{4}He pumping line
6 ^{4}He pumped bath (1 K Pot)
7 Film burner
8 Still
9 Continuous (spiral) heat exchanger
10 Contact area for HEVAC cooling pole
11 Cold Plate
12 Copper sinter
13 Cooling pole for Thermal Platform
14 Cooling pole for far infrared bolometer
15 Discrete (silver sinter) heat exchanger
16 Mixing Chamber
17 Still temperature radiation shield
18 4.2 K radiation shield
19 77 K radiation shield
20 Outer case
21 FIR bolometer on T-regulated plate
22 Rotatable pressure contact
23 Mylar window
24 Pressure gauge
25 Thermal Platform
26 HEVAC
27 Accommodator
28 77 K Pinning
29 Teflon valve
30 To microwave source
31 7.5 T main coil
32 Quadrupole coils
33 250 g 'switch' coil + sweep coil

Fig. 4.3. Schematic layout of the ESR experiment on atomic hydrogen in the dilution refrigerator.

the freedom to vary the static magnetic field. This can be useful to measure the field dependence of rate constants in decay processes. Our present equipment allows us to work at either ~ 160 GHz, 5.7 T or ~ 200 GHz, 7.1 T. After a single pass transmission through the sample the radiation is guided via a lightpipe to the detector: a FIR bolometer. The importance of a very sensitive detector for a good signal to noise ratio is already discussed at the end of section 4.2. The bolometer was situated as far away as possible from the magnetic field to avoid complications from magnetic field dependence of the sensitivity. It operates at a temperature independent of the hydrogen stabilization cell temperature.

The actual sample cell consists of a tube, 9 x 5 mm diam., of ordinary shelf quality copper (see fig. 4.4). At a height of 35 mm above the field center a mylar vacuum window is sealed with Stycast 1266[16]. To make this window accessible, a demountable joint had to be made which could also provide thermal contact to the mixing chamber. A large diameter (M9 x 1) threaded joint was chosen. Since the joint is in a high magnetic field, we expected that thermal contact would be improved by pressing a thin (<0.1 mm) indium layer between the flat end surfaces of the tubes[17,18] with annular cross sectional area 0.04 cm^2. The performance of this large diameter threaded joint proved to be rather poor: a thermal resistance, linear in 1/T, of $R \equiv \Delta T/P = 580\ 1/T\ [K^2/W]$ was found. (For comparison: this corresponds to an electrical residual resistance $R_0 = 14\ \mu\Omega$). Higher up in the connection to the mixing chamber we chose for a rotatable joint for alignment purposes. Here clean copper surfaces (area ~ 0.11 cm^2), without indium, were pressed onto each other by means of 6 brass M4 screws in a ring. The thermal resistance of this joint was lower than the threaded one by a factor of about 50. The connection to the mixing chamber is a 15 x 9 mm diam. copper tube, surrounding the 9 x 5 mm diam. light pipe. The actual thermal contact is provided by an M6 thread to a piece of copper which is in direct contact with the silver sinter inside the mixing chamber.

On one side of the sample cell, and connected via a 1 mm diam. hole is an indium seal demountable capacitive pressure gauge. This pressure gauge is similar to the one described by Mattheij et al.[19] except that

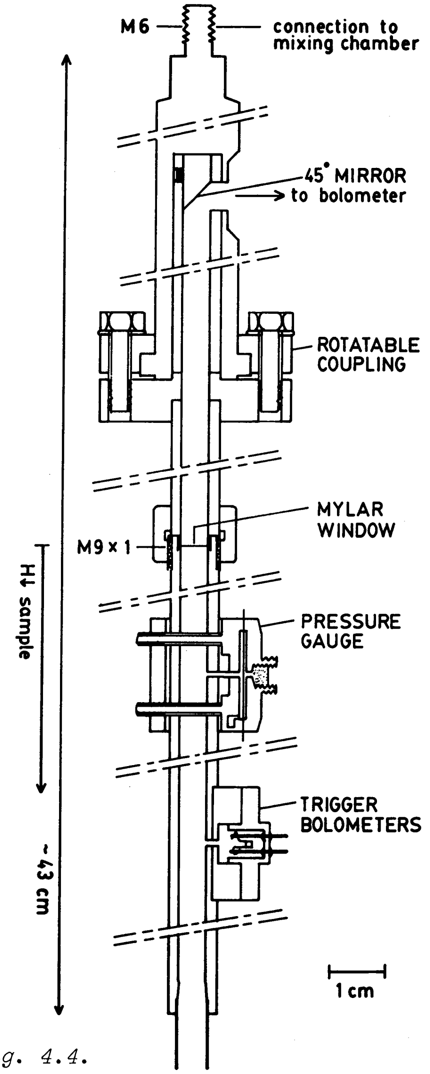

Fig. 4.4.

The hydrogen stabilization cell, showing the light pipe structure and the thermal connection to the mixing chamber of the dilution refrigerator. The sample occupies the volume below the mylar window.

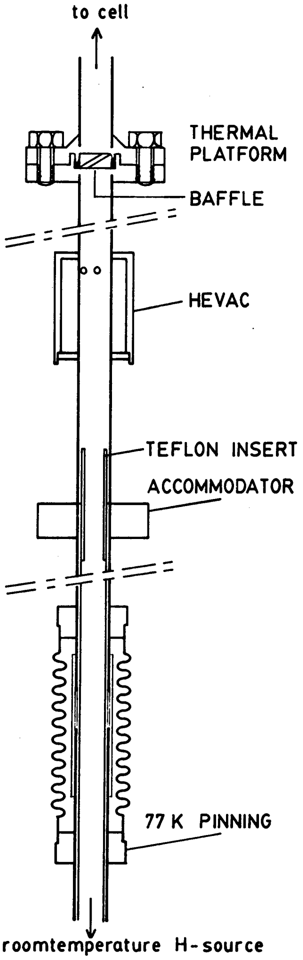

Fig. 4.5.

The lower parts of the hydrogen stabilization system. Teflon tube runs up to the accommodator, where it has a short insert of smaller diameter.

the reference vacuum side is now simply connected to the cryostat's inner vacuum space. The sensitivity is 1.65 pF/Torr and the zero pressure capacitance $C_0 \approx 29$ pF. A small (8.5 mm^3) reservoir was made below the membrane to prevent a bulk amount of ^{3}He from collecting in the pressure gauge in this vertical geometry, which would exert a liquid column height pressure to the membrane much larger than the H gas pressure. Because a small sweep coil was planned in the field center, the pressure gauge had to be positioned with its axis 42 mm below the field center. Even at a temperature as low as 200 mK, the pressure gauge still detects a density $\geq 95\,\%$ of the central density (at $B = 6$ T).

A set of two trigger bolometers[15], used to destroy the H sample was mounted in a separate chamber, connected via another 1 mm diam. hole to the sample space. Instead of carbon (sliced Speer resistors), heavily doped germanium chips were used, to avoid the ferromagnetic impurities which were found to be present in Speer chips.

All parts that are in direct contact with the H$\downarrow$ sample must be free of macroscopic magnetic impurities in order not to spoil the intrinsically very long nuclear spin relaxation time by an impurity effect[20]. This implied the following precautions: electrolytic etching of copper surfaces (removing $\gtrsim 1$ μm of the material); after that only very careful handling with non-ferromagnetic tools; the use of Stycast 1266 exclusively for glueing; the removal of enamel insulation of copper wires and the use of high purity (99.99%) indium for seals.

The HEVAC (Helium Vapor Compressor) and the Thermal Platform (fig. 4.5) serve to absorb the heat load of the refluxing helium vapors. For this purpose the thermal platform has a baffle in the form of a disk, with a 1 mm hole diagonally drilled. This baffle also serves as a cut-off filter for room temperature radiation, to be discussed below. The HEVAC is thermally pinned to the dilute stream of the continuous heat exchanger in the dilution refrigerator. Similarly the thermal platform is connected to the so called Cold Plate, i.e. a copper sinter connection to the dilute stream between the continuous and the first step-heat-exchanger. To realize the thermal pinnings heavy copper connections, 1 cm^2 in cross section and ~ 50 cm long, were needed in series with flexible copper braids. Typical operating conditions were: HEVAC 660 mK and Thermal Platform 570 mK. The measured heat load for these temperatures was 0.45 mW and 0.2 mW respectively.

The accommodator is connected to the 4.2 K tail of the cryostat and operates at 7.5 K. A teflon tube arrangement as shown in fig. 4.5 was used. The idea is to keep the distance between the 'warm' teflon and the cold HEVAC as short as possible, to minimize recombination losses of the H on its way to the stabilization cell. A flux of $\sim 2 \times 10^{14}$ atoms per sec into the cell was realized with this geometry.

All thermometry below 1 K was done with 200 Ω 1/8 W Matsushita carbon resistors[21,22]. These were calibrated against a germanium resistor, which in turn was calibrated with in-situ ^{3}He vapor pressure thermometry. Also 3 fixed points at ~ 100, 160 and 200 mK of an NBS SRM 768 superconducting fixed point device were transferred to this germanium resistor. A very useful property of the Matsushita's is their relatively weak dependence on magnetic field, e.g. at T = 300 mK in 6 Tesla a correction of only + 10 mK with respect to the zero field calibration has to be made.

To generate the microwaves we use a frequency multiplication technique (fig. 4.6). The signal from a Gunn oscillator (Central Microwave Company CME 717 AD ; output ~ 75 mW; voltage tunable from 38.6 to 39.4 GHz) is fed via an isolator and an attenuator to a crossed-guide harmonic generator[23]. This multiplier (Custom Microwave MU-97-37) has a rectangular output waveguide with cut-off frequency 137 GHz, so that only harmonics $n\,f$ with $n \geqslant 4$ are produced. The original Si-crystal was replaced by a chip with an array of GaAs Schottky-barrier diodes (MWT Millimetre Wave Technology VD009). Tungsten whiskers of diameter 25 micron were used. Although this type of diode is in fact a varactor (non-linear capacitor; diode biased in reverse direction) in our mount we cannot make use of the high efficiency of the varactor multiplication principle. The reason is that in a waveguide mount there is no way to provide the necessary 'idler circuits' for this high order ($n \geqslant 4$) multiplication. Highest output power was obtained by using the diode as a rectifier. The diode is self-biasing by using a load resistor (optimized at ~ 2 kΩ) for a few mA of forward current. The power output is estimated to be ~ 10 μW for $4\,f$ and $5\,f$ and lower for higher n, up to

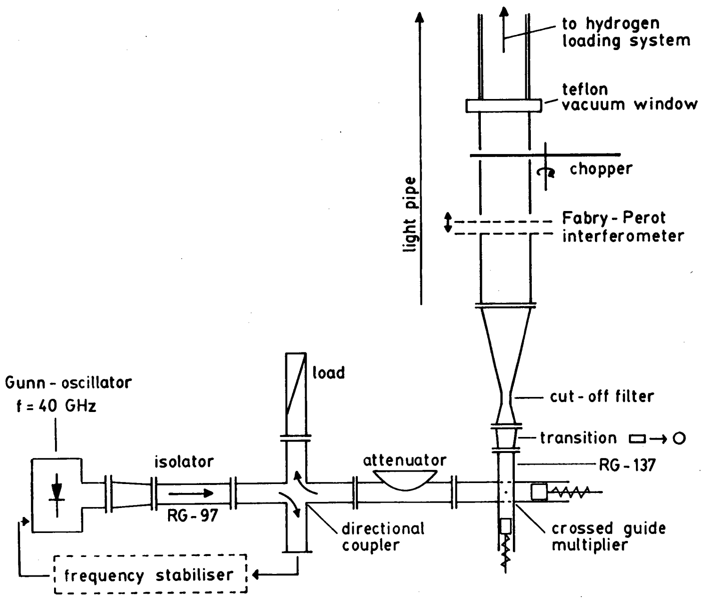

Fig. 4.6. The microwave source. Monochromatic radiation of frequency 160 GHz or higher is obtained by frequency multiplication

n = 11. Most important was the reliability: the mechanical stability of the whiskerpoint-chip contact was excellent and could easily survive several weeks in a pretty rough environment.

Selection of the desired harmonic is achieved by :

1) waveguide cut-off filters, and

2) an in-line Fabry-Perot interferometer in transmission mode.

Immediately after the multiplier a transition from rectangular to circular waveguide was made, providing a cut-off just below $4f$. Four (high pass) cut-off filters were made for the dominant TE_{11} mode in circular waveguide. The filters that remove $4f$, $5f$, or $6f$ consist of a 3 mm long circular 'constriction' combined with small angle tapers. The filter which transmits $4f$ is only a single taper to 5.6 mm exit diameter. The design criterion was $\geqslant 40$ dB attenuation for unwanted harmonics and $\leqslant 0.1$ dB loss for the transmitted frequencies. These filters were electroformed of copper. The tolerance on the diameter of the cut-off section is 0.01 mm.

An additional filter in the form of a Fabry-Perot interferometer (fig. 4.7) was needed to remove the higher unwanted harmonics. The only available control to optimize one particular harmonic and to suppress other ones is the adjustment of the shorting plungers in the waveguides of the multiplier. A tuning procedure by monitoring the power output of the multiplier could lead to errors: one might very well find himself optimizing $5f$ instead of the desired $4f$. The Fabry-Perot acts as a monochromator, and its dial was calibrated using a lamellar grating far infrared interferometer. The peak transmission must be high, and the resolving power can be low; in fact it must be a broadband device with respect to the +/- 1 % tuning range of the Gunn-oscillator. In this Fabry-Perot interferometer[24,25,26] two gold plated nickel meshes with rectangular holes (see fig. 4.7) were used as partial reflectors. The meshes were stretched across two coaxial cylinders, which can move with respect to each other by means of a differential screw mechanism with 1 μm resolution. Flatness and parallellism of the meshes were better than 2 μm. The choice of the grid parameters was an overall compromise between peak transmission, broadband operation and suppression of

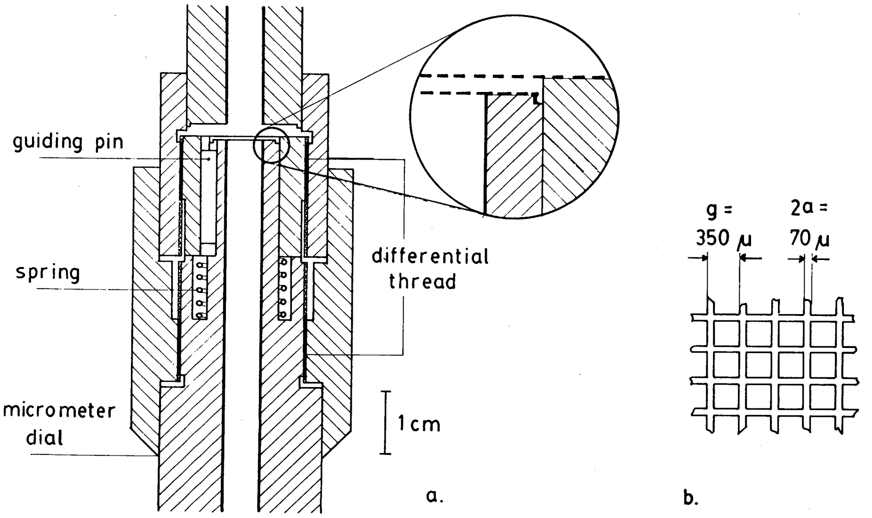

Fig. 4.7. a. Construction of the Fabry-Perot interferometer in light pipe
b. Parameters of the (inductive) mesh.

unwanted harmonics in the range n = 4 - 7. The measured peak transmission at 160 GHz was 41 % and the finesse (in zero order) was 100.

The operation of a Fabry-Perot is usually described with incident plane waves propagating in free space, whereas the radiation here is propagating as guided waves, which may be very different. However, the 5.6 mm diameter circular waveguide is very much oversized, such that for instance at 160 GHz some 23 modes can propagate. Although after the cut-off filter the TE_{11} mode is launched, it is very unlikely that this pure mode structure will be preserved, because any discontinuity (flange coupling etc.) will excite higher modes. In fact, from the observation that the Fabry-Perot has a peak transmission as 'high' as ~ 40 % it can already be concluded that a superposition of many modes, which altogether behave plane wave like, is present. This technique for radiation transport is known as light pipe optics[27], and is frequently used in far infrared equipment. It can be regarded as plane waves bouncing back and forth by reflection from the surfaces.

A -20 dB sample of the Gunn-oscillator signal is fed to a Microwave Systems MOS 3600 stabilizer. This circuit actively stabilizes the frequency of the Gunn-oscillator by phase-locking it to an internal quartz oscillator, or an external frequency synthesizer. The microwave frequency is then stable for $\sim 1 : 10^7$ per hour. The frequency can be modulated at a maximum 500 Hz rate with a modulation depth of ~ 1 MHz.

To detect the microwaves we built a cryogenic far infrared bolometer of the composite type[28]. A sapphire sheet of dimensions 5 x 5 x 0.13 mm has an evaporated NiCr film of $R_\square = 179\ \Omega$, which value rises to $215\ \Omega$ at $T \approx 0.5$ K. This is close enough to the optimum value $R_\square = \mu_0 c/2 = 188.5\ \Omega$ which would give a, frequency independent, power absorption of 50 % . On the other side of the sapphire a chip of doubly doped (InSb) germanium[29] of size $0.6 \times 0.6 \times 1\ \text{mm}^3$ was glued. Two 0.15 mm diam., 23 mm length copper wires were indium soldered to the chip and served as heat link to the 'bath'. The bath is actually a copper plate which is weakly coupled to the dilution refrigerator's Cold Plate. The bolometer plate is actively regulated at a temperature of 0.45 K by a simple proportional controller. The measured electrical NEP (Noise Equivalent Power) of the bolometer was $\sim 10^{-13}\ [\text{W/Hz}^{\frac{1}{2}}]$ at f = 500 Hz.

The noise was 1/f -like, apart from apparently strong mechanical resonances in the range of a few Hz. The measured time constant was 0.5 msec, which allows very rapid modulation up to ~ 500 Hz without excessive loss of sensitivity. The measured electrical responsivity was 1.1×10^6 V/W. A cold (4.2 K) load resistor, consisting of four 1MΩ metal film resistors (SFERK3 RS63Y) in series was used. The main advantage of the composite bolometer for this experiment is the 50 % power absorption even for wavelengths in the millimetre range, as compared to single element bolometers which are only weakly absorbing at this extreme far infrared. As a filter to cut off room temperature radiation in the visible and near infrared, which would degrade the bolometer's performance, we use a low pass FLUOROGOLD filter, sandwiched between layers of black polyethylene. It is located in the Thermal Platform and is cooled by a superfluid helium film. It cuts off at 40 cm^{-1} (1200 GHz).

The use of light pipe in most of the system may suggest an efficient transmission. For example, an elementary calculation in the bouncing wave picture[27] gives, for a 1 m long german silver pipe of 5.6 mm diam. at a frequency 160 GHz, a transmission of ~ 70 %. In practice the transmission from the waveguide cut-off filters to the bolometer is estimated to be $\lesssim$ 1 %. The large losses could reasonably be explained by separate measurements of the transmission of some of the imperfections in the light pipe, such as reflection from windows, interruption of the light pipe over ~ 6 mm (in the teflon valve), etc. The teflon tube inside the 'warm' part of the hydrogen fill line gave a large loss: ~ 50 % over only a 10 cm length.

To summarize the properties of the microwave part of this experiment: we have a hybrid system which combines a high resolution, monochromatic source, with the quasi-optical techniques known from broadband far infrared spectroscopy.

Our main magnetic field is produced by a 7.5 T max. superconducting magnet. The full width of the field profile between the half-value points is 21 cm. The homogeneity is better than 1 : 10^5 in a 1 cm diameter spherical volume around the symmetry center. A small superconducting coil was added directly outside the H sample cell; this produces a ~ 250 Gauss field. By reversing the current one can quickly switch between the two hyperfine transitions in the hydrogen ESR spectrum. A third small coil is added to facilitate rapid sweeps of only a few gauss. Both coils are designed to preserve the homogeneity of the main magnetic field, however only in the central 1 cm volume. To prevent excessive eddy current heating, which would destroy the sample, the current reversal in the 250 gauss coil had to be done slowly. This was realized by the power supply system indicated in fig. 4.8.

A set of quadrupole coils (item 32 in fig. 4.3) of large diameter were wound on the main coil. They can provide a field gradient of max. 0.05 T/cm. Together with the main field a $\frac{dB}{dz}$ constant to within 5 % over an 8 cm length results. This almost linear gradient field may serve for the measurement of an H density profile as proposed in section 4.2; however it was not used in this experiment.

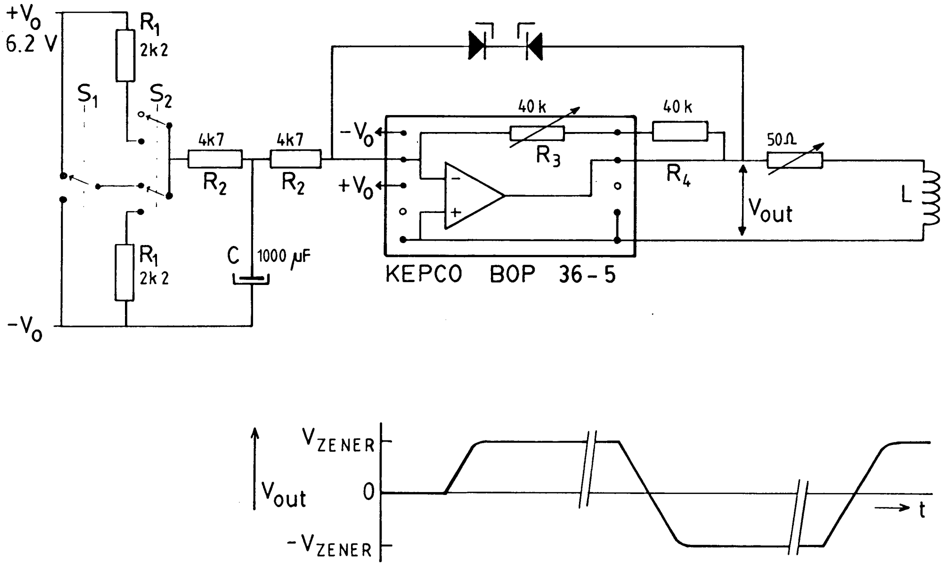

Fig. 4.8. The circuit that can reverse (S_1) *and swith on/off* (S_2) *the current in a coil* L *with controllable* dV_{out}/dt.

$$\left|\frac{dV_{out}}{dt}\right| = \frac{V_0}{\tau} \cdot \frac{R_3 + R_4}{R_2} \quad \textit{with} \quad \tau = \frac{R_1 C}{2} \; .$$

4.4. ESR measurement techniques for H↓

A number of methods are available for registration of the resonance lines. An obvious one is to sweep the microwave frequency; however the microwave power detected at the FIR bolometer varies extremely rapidly with frequency. This is known to originate from the setting up of standing waves between any two discontinuities in the waveguide which act as partial reflectors. Even though precautions were taken to avoid as much as possible these discontinuities, many oscillations were observed within the +/- 1 % frequency tuning range. This makes sweeping the frequency at constant magnetic field very unattractive, so we tune the frequency to a broad maximum in power, and stabilize it there.

As a second method we can use the small sweep coil to apply an additional field with a triangular waveform. The main coil is set into persistent mode at a field which is a few gauss off resonance. Under favorable conditions The ESR absorption lineshape could be displayed in one single sweep, but usually signal averaging was employed on a Nicolet 1174. Repetition rates ranging from < 1 Hz up to 50 Hz were used, depending on the amplitude of the sweep. The upper limit is set by the response time of the bolometer and the amount of distortion in the lineshape that is considered acceptable. The average of 128 sweeps for the $b \rightarrow c$ transition for a sample density $> 10^{16}/\mathrm{cm}^3$ is shown in fig. 4.9. Each sweep of 0.2 sec duration consists of a ramp up and down, peak-peak excursion 20 gauss, of which only the part with the positive slope is used. Total measurement time is 26 sec. The ripples in the line are not associated with noise, but present reproducible fine structure which must all be caused by the (axial and transverse) magnetic field profile. Achievement of such an excellent signal-to-noise was possible only at high densities, and at the expense of loss of part of the sample because of the destructive action of ESR.

The peculiar lineshape relates to the behavior of the field gradient $\frac{dB}{dz}$ as described in section 4.2. The axial field profile, as measured by the manufacturer of the main coil is shown in fig. 4.10A. The two peaks in the ESR line originate from the sample regions where $\frac{dB}{dz} = 0$. Apart from the region around $z = 0$, there is a second region at $z = + 19$ mm

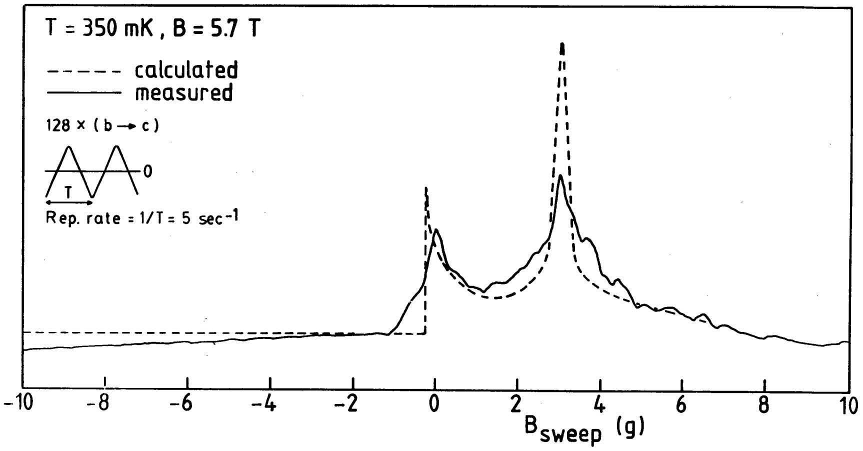

Fig. 4.9. Lineshape of the b → c transition, observed (———) by sweeping the magnetic field and performing signal averaging of the FIR bolometer signal. A lineshape (- - - -) calculated from the known field profile is also shown.

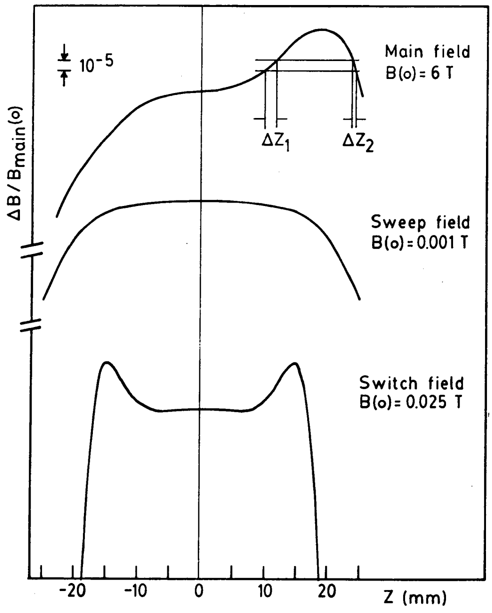

Fig. 4.10.

A. Axial field profile of the main field, as measured with D_2O NMR.

B. Profile of the sweep field (simple solenoid), same scale as A.

C. Profile of the 'switch' field (solenoid with extra compensating windings on its ends).

where the field has an (unintended) maximum which is, at B = 5.7 T, 3.35 gauss higher than the central region. This agrees reasonably with a measured splitting between the two peaks in fig. 4.9 of 3.03 gauss. In fig. 4.9 we also plot a lineshape, predicted from the known field profile by taking the absorption proportional to $(\frac{dB}{dz})^{-1}$ and adjusting the integrated intensity. The difficulty of the diverging $(\frac{dB}{dz})^{-1}$ is avoided by performing a discrete summation over contributions from sample 'slices' of thickness Δz_1 and Δz_2, chosen such that all atoms within these satisfy the resonance condition in intervals of fixed ΔB (see fig. 4.10A), and smoothing the result by hand. The predicted line is much narrower than observed; also the infinitely steep edge corresponding to the absolute field maximum is not observed. The differences are likely to be caused by the radial field gradients which are not taken into account in this strictly 1-dimensional model. No attempt was made to improve this model for the following reasons :

1) A complete off-axis field map is not available. All we know is that along a 5 mm radius circle in the $z = 0$ plane the field varies by $\sim 3 \times 10^{-5}$. So there is no cylindrical symmetry and $\frac{\partial B}{\partial \rho}$ cannot be calculated from $\frac{\partial B}{\partial z}$.
2) The field of the sweep coil is not 'flat' on a wide enough range on the z-axis. In fig. 4.10B is also plotted the field of the sweep coil on the same relative scale for a maximum field of 10 gauss. This implies that the resultant field profile will change during the sweep, i.e. the lineshape is changing while it is scanned. The sweep coil however is designed to have sufficient homogeneity in the center, so that the central peak in the ESR line would be unaffected. Only the position of the secondary line and the shape of the wings could change. (This design criterion was only marginally satisfied, however.)

An effect related to this is that the 250 gauss coil, which is used to switch between the two transitions $a \rightarrow d$ and $b \rightarrow c$, also changes the field profile and thus the lineshape. The field of the 250 gauss coil is plotted in fig. 4.10C, again on the same scale. The resulting total field for the two situations is seen in fig. 4.11. The coil has compensating windings on its ends, which improve the central homogeneity but strongly complicate the field around $z = \pm 15$ mm. No attempts to predict lineshapes from fig. 4.11 have been made, since there would be in each case 3 or more secondary lines, the position of which would be very sensitive for small alignment errors of the 250 gauss coil with respect to the main coil.

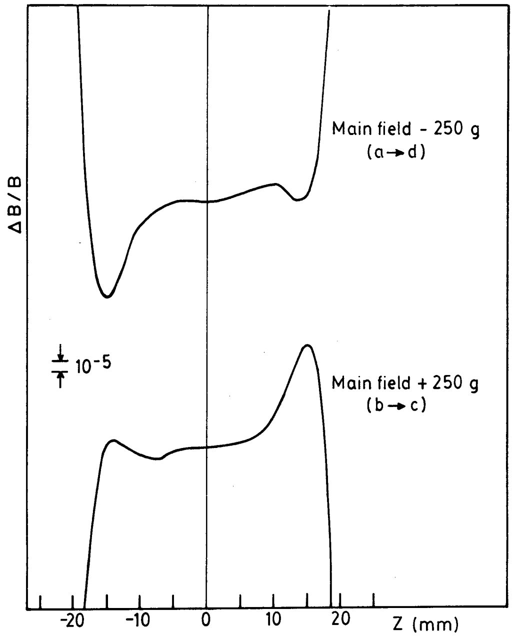

Fig. 4.11.
Field profile of the 250 gauss switch coil, added to or subtracted from the main field. The scale is the same as in fig. 4.10.

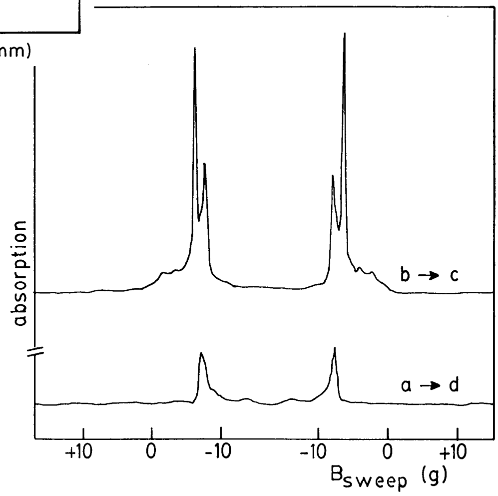

Fig. 4.12. Lineshapes of the a →d and b →c transitions when using the 250 gauss switch coil. Conditions same as in fig. 4.9, but with a wider field sweep.

The experimental lineshapes observed by switching the field by ± 250 gauss and sweeping with a symmetric up-down ramp of the sweep coil are shown in fig. 4.12. The large difference between the $a \rightarrow d$ and the $b \rightarrow c$ transition was not anticipated; this difference cannot even be explained qualitatively on the basis of the field profiles in fig. 4.11. It was expected that, since the homogeneity of the central 1 cm region is not affected by the 250 gauss coil, there would always be a very sharp line coming from the atoms in this central 1 cm, although there would be wings and/or secondary lines coming from regions outside the central 1 cm. However, in reality the line is not all that sharp, and in the case of $a \rightarrow d$ even the double peak structure is completely absent. The broadening, apparently caused by transverse field gradients, makes it impossible to tell which part of the line comes from the central 1 cm sample length. As a consequence, in order to use the intensities of the $a \rightarrow d$ and $b \rightarrow c$ transitions to establish the relative population of the a- and b-state, one has to do either of the following things :

1) Use the integrated intensity $\int \alpha \, dB$; this represents the total number of atoms in the distribution.
2) Calibrate in some way the peak heights of the two different lineshapes for a sample of known composition.

Use of the integrated intensity method is difficult, because the lineshape is known to have a low but very broad wing on one side, which cannot be measured accurately due to low frequency noise. This noise, probably due to mechanical resonances of the bolometer suspension, is much larger than the random 1/f-noise, and results in a 'wavy' baseline on the signal averager. Moreover, these signals usually do not cancel each other in multisweep averaging due to a coherence with the repetition of the magnetic field sweep. The example in fig. 4.9 behaves rather decent in this respect, but it is not typical. The origin of this cross-talk to the bolometer was not examined in detail, but it is believed that a slight movement occurs at the moment of the current reversal in the sweep coil, exciting the bolometer into vibration.

Before proceeding we will introduce one other feature, namely the option of measuring the derivative of the line by applying a rapid sinusoidal frequency- or field modulation. If no true derivative signal is required, a modulation amplitude comparable to the linewidth may be chosen for maximum signal. This enables phase-sensitive detection of the bolometer signal in a narrow bandwidth with the advantage of suppression of the spurious low frequency noise. Frequency modulation was chosen; the crystal reference oscillator could be modulated at a frequency of max. 500 Hz and an amplitude such that a peak to peak frequency deviation 4 - 6 MHz relative to 160 GHz was obtained, while the whole stabilization chain remained locked for long term stability. An offset signal on the bolometer may now occur as frequency modulation also leads to amplitude modulation if the central frequency is not adjusted to a local maximum in the transmission curve. Magnetic field modulation was not succesful. This can be explained by a skin depth of only 0.39 mm for $f = 500$ Hz in the highly conducting copper at low temperature. A penetration of only 0.006 in the 2 mm thick cell walls would result.

In order to measure n_a and n_b we must develop a calibration procedure, as we have seen that the integrated intensity method will not work. We require a sample of reproducible n_a/n_b concentration ratio. Since H↓ samples are subject to decay this is best done in a steady state situation. We used a constant filling flux, rather low, so that the heat of recombination can be dealt with and the temperature of the cell is under control. n_a and n_b will be constant after a long time; as for $n = n_a + n_b$, this was checked with the pressure gauge. For the actual calibration we tune the main field exactly on one of the lines; we use a symmetric triangular sweep of a few gauss only and make sure that the line is swept about midway at zero current, so that the contribution of the sweep coil to the field profile is minimum. This procedure is repeated for the other line. Both transitions were observed to have the same lineshape indeed, and the ratio n_a/n_b is measured. Next the main field is set to a value in between the previous two values and the 250 gauss coil is used in either polarity to switch between the transitions. The lineshapes are different now, but since we are still measuring the same steady state sample, a correction factor is known now for converting peak signal ratios to density ratios n_a/n_b. This procedure was followed for the measurements in fig. 4.15, to be described in section 4.5. Intensity is the peak to peak value of the strongly overmodulated (FM) 'derivative' signal. The accuracy of such a calibration factor is rather disappointing: ± 10 %. This is caused by the following :

1) The total time needed is about half an hour and it is difficult to maintain constant steady state conditions for such a long time.
2) Every calibration will become outdated in about the same time, since the main field appears to drift with a speed of ~ 3 gauss/hr. This is because of the finite L/R time constant of the superconducting coil in persistent current mode. The sweep coil will have to compensate for the lost field with an offset; the insufficient homogeneity of the sweep coil however will gradually change the lineshape. The effect is illustrated in fig. 4.13 on a somewhat exaggerated scale: the field sweep is 40 gauss peak-peak.

All told it means that for accurate results the 250 gauss coil cannot be used at all and the sweep coil only for very narrow, well centered sweeps. For all quantitative results the sweeping and switching must be done with the main field. This is a serious handicap: the magnet cannot be used in persistent mode. When the switch is 'open' the finite shunt resistance introduces an L/R time constant that makes it difficult to produce constant slope triangular waveform sweeps. The cycle time

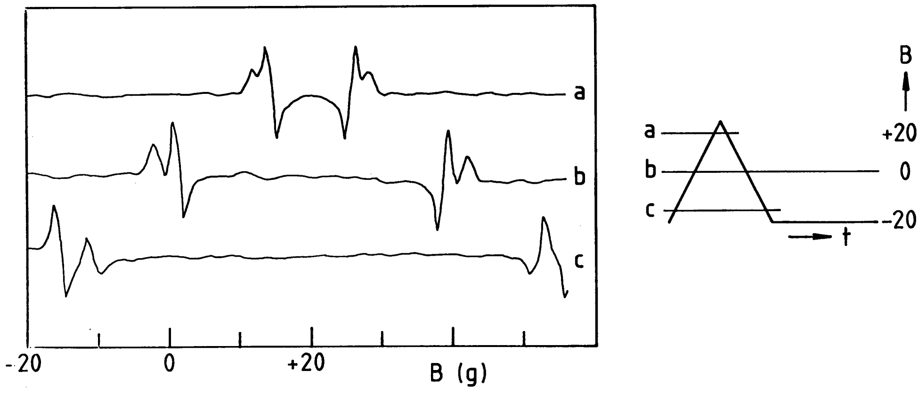

Fig. 4.13. Derivative lineshapes of the $b \rightarrow c$ transition for three different settings of the main field. In case ⓑ the field of the sweep coil is almost zero when the line is swept; this is the best approximation of the 'true' lineshape of the main field only.

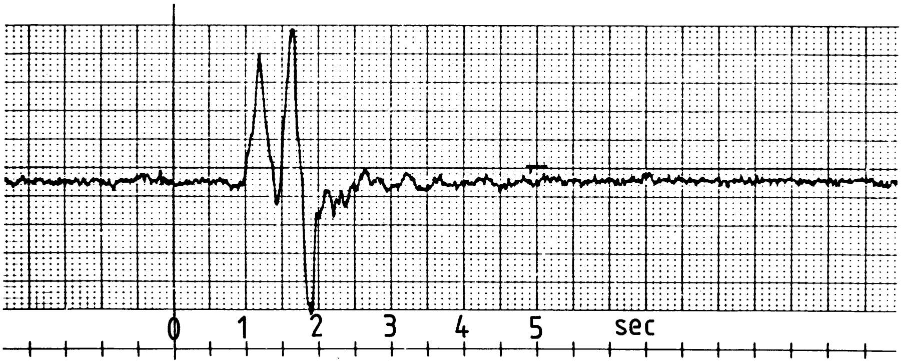

Fig. 4.14. The b → c transition measured with frequency modulation, single sweep with main field. $T = 310$ *mK,* $B = 5.7$ *T,* $n_b = 4.5 \times 10^{15}/cm^3$*. This corresponds to the best signal/noise data points in the analysis of fig. 4.17.*

needed to measure both the a → d and the b → c transition one time each turned out to be ~ 100 sec, compared to 20 sec for the same procedure with the 250 gauss coil.

In fig. 4.14 is shown the lineshape observed when studying a sample under decay with this main field sweep + frequency modulation technique. The lines are swept through in about 1 sec. To compare with fig. 4.9 we must keep in mind that the latter is a multisweep averaged line. In addition the signal to noise in fig. 4.14 is lower than in fig. 4.9 by a factor ~4 because the 39 GHz Gunn-oscillator malfunctioned and was replaced by a klystron with a little less power output, so that the harmonic power at 4·39 GHz fell to $\sim\frac{1}{4}$. A density of $6 \times 10^{13}/\mathrm{cm}^3$ could be detected in these 1 sec sweeps with a signal/noise ratio of one.

4.5. *Results*

As the most important result we present the measurement shown in fig. 4.15. Here we plot the signal strength of the a → d and the b → c transition, measured alternatively with ~ 10 sec intervals. We use frequency modulation, a main field sweep, the ± 250 gauss coil for switching and a calibration procedure as outlined in section 4.4. The signal strength is proportional to the density n_a and n_b of the atoms

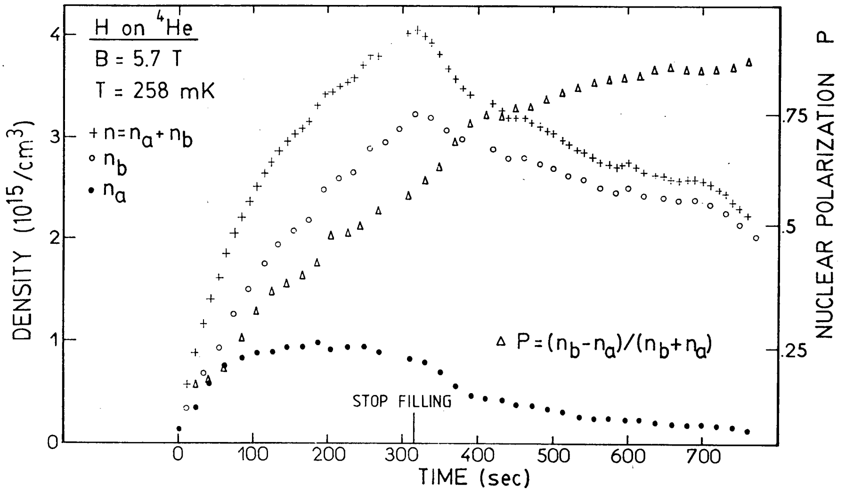

Fig. 4.15. The density of atoms in hyperfine states a and b during the loading and decay of a sample, and the nuclear polarization P.

in hyperfine states a and b. By interpolation the curve which gives the total density is constructed, and by comparing this with the pressure gauge recording the density scale is established. From fig. 4.15 we have a very direct and convincing demonstration of the principle of relaxation bottlenecked recombination[2]. Although there was already indirect evidence for this process[30,20], this represents the most direct and clear demonstration of the time evolution to the double polarized state. We make the following observations from fig. 4.15 and a number of other measurements made under various conditions :

- By extrapolating the tangents to the n_a and n_b curves to $t = 0$ we see that the initial filling fluxes for a- and b-state atoms are equal. The density increases linearly with time and there is no recombination yet;
- When recombination sets in the density of the a-state atoms grows less rapidly than that of the b-state atoms. This is caused by the preferential recombination of the a-state atoms;
- n_a saturates after a while, and so does n_b but much later. Both saturation levels are proportional to the square root of the incoming flux of cold H atoms;

- When the filling flux is switched off, n_a quickly reduces to a very low value by recombination. This effect is not too dramatic in fig. 4.15, because during the long filling n_a was already much smaller than n_b;
- After removal of most of the a-state atoms a different time scale for the density variations sets in. Although the loss process is still recombination, the time scale is set by the nuclear spin relaxation, which converts b- into a-state atoms.

The nuclear polarization $P \equiv (n_b - n_a)/(n_b + n_a)$ is also plotted. It is seen that no steady state situation had been established yet at the time of the beginning of the decay. No effort was made to obtain the highest possible accuracy for this 'demonstration', but instead the objective was to collect as many data points as possible in one single run.

The destructive action of the ESR transitions is illustrated in fig. 4.16. At $t = 0$ a steady state situation with a constant filling flux already exists. At ① the microwave radiation is switched on, exactly tuned on resonance for the $b \rightarrow c$ transition, and with maximum incident power. At ② the radiation is switched off and the density recovers. A time constant $\tau_{rad} \approx 100$ sec for exponential decay is estimated, consistent with microwave power $P_{in} \approx 0.2\ \mu W$ (eq. (4.20)). A similar but less dramatic result is obtained when sweeping the magnetic field over a range just a little more than the line width. Each sweep of ~ 0.5 sec

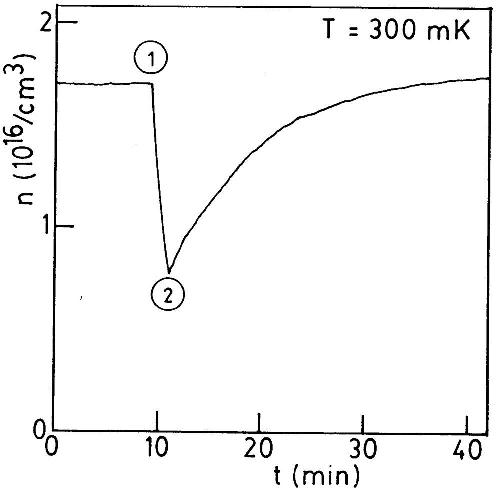

Fig. 4.16.

Partial destruction of a sample as measured with the pressure gauge by strong irradiation of the b → c transition.
① power on, ② power off.

destroyed ~ 0.25 % of the density n_b. When measuring densities etc. substantially lower powers or off-resonance conditions were used so that the measurement did not measurably affect the density.

Now that ESR has made it possible to observe the density of atoms in the a- and b-state independently, a number of further properties of H↓ can be measured. The rate equations that describe the time evolution of the density, modified to include the effect of ESR transitions, are[2,20]

$$\frac{da}{dt} = \frac{\Phi_a}{V} - \frac{a}{\tau_{esc}} - \frac{a}{\tau_{rad}} - 2K^e_{aa}a^2 - K^e_{ab}ab - G^{ie}_s(a-b) - (G^e_s + G_V)(a+b)(a-b)$$

$$\frac{db}{dt} = \frac{\Phi_b}{V} - \frac{b}{\tau_{esc}} - \frac{b}{\tau_{rad}} - K^e_{ab}ab + G^{ie}_s(a-b) + (G^e_s + G_V)(a+b)(a-b) \qquad (4.21)$$

Here we write $n_a = a$, $n_b = b$. Φ_a and Φ_b are the filling fluxes. τ_{esc} is the time constant for thermal leakage from the cell. An extra term for loss of atoms by ESR transitions is included with τ_{rad} given by eq. (4.20). During decay Φ_a, $\Phi_b = 0$ and to a good approximation we can take $\tau_{esc} = \infty$, $\tau_{rad} = \infty$. G^{ie}_s is the effective $a \leftrightarrow b$ nuclear relaxation rate constant due to the interaction of adsorbed H↓ atoms with the magnetic impurities in the cell walls. $G^{ie}_s = G^i_s\ A/V\ \lambda\ \exp(\varepsilon_a/k_BT)$ with G^i_s the intrinsic rate, $\lambda = \sqrt{(2\pi\hbar^2/mk_BT)}$ is the thermal de Broglie wavelength, and A/V the surface area to volume ratio of the sample cell. G^e_s and G_V are the relaxation rate constants for intrinsic (H↓ - H↓ interaction) relaxation on the walls and in the gas phase; $G^e_s = G_s\ A/V\ \lambda^2\ \exp(2\varepsilon_a/k_BT)$. These rates have been studied and discussed elsewhere[30,20,9] and will be eliminated from the equations; they are not discussed in the present context. $K^e_{aa} = K_{aa}\ A/V\ \lambda^2\ \exp(2\varepsilon_a/k_BT)$ and K^e_{ab} are the effective recombination rate constants for surface recombination. Recently Sprik et al.[20] have measured these constants using a pressure gauge technique, and measurements at Cornell[9] using a similar method but extended with strong NMR irradiation to equalize the population of the a- and b-state, have provided additional information on the temperature dependence of these constants. In ref. 20 the result $\gamma \equiv K_{aa}/K_{ab} = 2.23 \pm 0.25$ was found. Some criticism was made concerning this work suggesting the possibility of non-thermodynamic equilibrium arising from Kapitza resistance to the transport of recombination energy from the gas to the copper walls of the cell. We shall deal with the Kapitza resistance shortly. Here we develop a direct technique of measuring γ using ESR and a pressure gauge during decay of the gas. After adding the equations (4.21) and defining $n \equiv a+b$ and $P' \equiv b/a$ (population ratio) we have :

$$-\frac{(1+P')^2}{2n^2}\frac{dn}{dt} = K^e_{aa} + K^e_{ab}\cdot P' \tag{4.22}$$

The idea is to measure P' with ESR and n and $\frac{dn}{dt}$ with the pressure gauge ($n = p/k_BT$). In principle one could even do without the pressure gauge and use n and $\frac{dn}{dt}$ from ESR also. A plot of $Y = -\frac{(1+P')^2}{2n^2}\frac{dn}{dt}$ vs. P' is expected to give a straight line with slope K^e_{ab} and intercept K^e_{aa}, from which the ratio K_{aa}/K_{ab} can be determined. Some nice features of this method are :

- The nature of the nuclear relaxation processes need not be known, since all relaxation terms drop out. Even if the very non-specific impurity surface relaxation would be the dominant process, the method could still work. Of course, in the limit of very fast relaxation one would always have P' very close to 1; only the average $K = (K_{aa} + K_{ab})/2$ is then measured.
- When enough microwave power is available, the b → c transition could be 'pumped' to create ratio's $P' < 1$. The c-state atoms would be ejected from the cell by the field gradient, or recombine, depending on conditions. Also the a → d transition could be pumped to increase P'.
- The pressure gauge does not have to be calibrated; a scale factor in n and $\frac{dn}{dt}$ does not influence K_{aa}/K_{ab}.
- In contrast to the method of Sprik et al.[20], this method is not limited to low densities and a very narrow temperature range. Their method relies upon the assumption of equal initial densities a and b (which is valid only for very short loading times) and the neglect of relaxation with respect to recombination: $G^e \ll K^e$. Since at low densities the impurity relaxation ($\propto n$) tends to dominate the intrinsic G_V and G^e_s ($\propto n^2$), and because of the different temperature dependence of G^{ie}_s ($\propto \exp(\varepsilon_a/k_BT)$) and K^e ($\propto \exp(2\varepsilon_a/k_BT)$) this

condition is only fulfilled for low temperature (225 - 300 mK). On the other hand, the temperature may not be so low that recombination is fast and occurs already during the few seconds of loading. The present method may be applied at any temperature and would be suited to measure a possible temperature dependence of K_{aa}/K_{ab}.

The result of a series of 4 runs at $T = 310$ mK and $B = 5.7$ T are presented in fig. 4.17A. An unweighted least squares fit yields the line such that $K_{aa}/K_{ab} = 2.4$, supporting the results of ref. 20 and 9. However, there is a considerable scatter in the data points and one would have to take into account error bars and the associated weights. The largest source of error is the uncertainty in P' because of the low a-densities. Also the error in $\frac{dn}{dt}$ from the pressure gauge could be important since it is very sensitive for small drifts of the baseline. As for the error in P', this propagates in Y. The error bars are thus tilted over an angle $\theta = \arctan[2Y/(1+P')]$ (Y measured in units 10^{-18} $cm^{-3}s^{-1}$). A few examples of error bars are indicated in fig. 4.17A. Since $2Y \approx 1 + P'$, the angle is ~ 45°. A correct procedure is to rotate the coordinate system over 45°, perform a linear least squares fit (including weight factors $\propto 1/(\Delta P')^2$) and transform the parameters of this line back to the original coordinate system. When this is done we find $K_{aa}/K_{ab} = 10 \pm 2$. The line with the smaller slope, $K_{aa}/K_{ab} = 8$, is plotted in fig. 4.17A; it does not seem very plausible. This is because the weight factors are $1/(\Delta P')^2 \propto \frac{(a)^4}{b^2(\Delta a)^2} \propto a^4$ so that very low weight is attributed to the points with higher P'. Moreover, the whole treatment of weights relies upon the random statistical distribution of errors. There is clear evidence that a systematic effect is present in the evolution of single runs that renders such a statistical weighting of errors as meaningless. This can be seen in fig. 4.17A (solid circles), which are plotted separately in fig. 4.17B. A least squares straight line fit to this run would give a negative K_{aa} ! Most runs tend to behave like this when analyzed separately. We are forced to conclude that K_{aa}/K_{ab} is somewhere in the range 2 - 8, in agreement with earlier determinations of Sprik et al.[20] and the Cornell group[9]. A broader range of P' would certainly improve the situation, as would a better

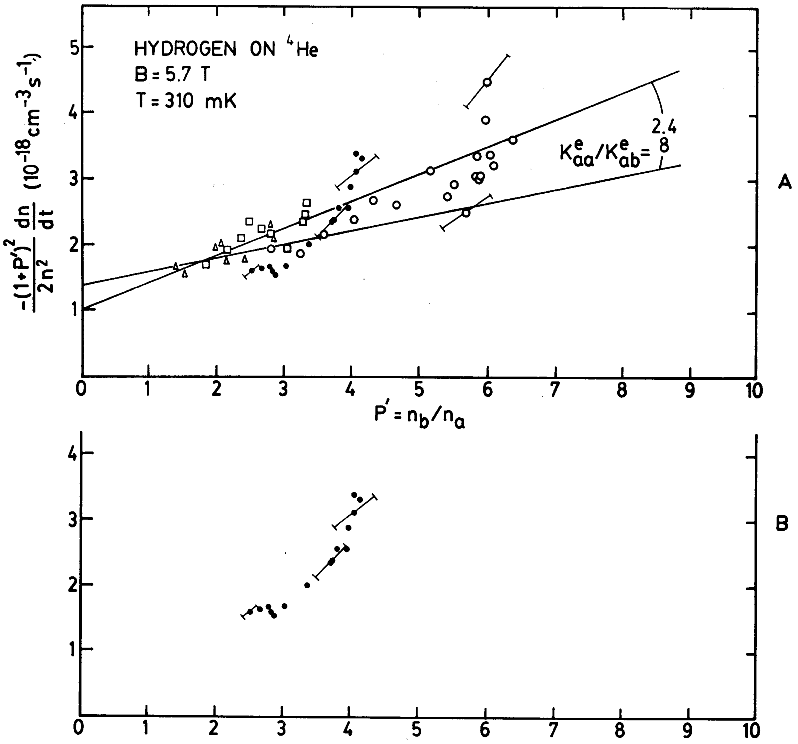

Fig. 4.17 A. Data used for determining the ratio K_{aa}/K_{ab} *of recombination rate constants, including error bars for some typical points. Data of four different runs are presented.*

B. One of the decays of A., showing a systematic effect not visible in the compilation of four runs.

signal/noise in the ESR signals. Two limitations during this experiment that prevented us from doing a detailed analysis of this subject were: the inability to switch quickly between the a → d and b → c transition as explained in section 4.4, so that potentially valuable data points in the beginning of a decay were missed, and the lack of sufficient microwave power due to replacement of our Gunn-oscillator with a klystron. We have tried to pump one of the transitions to increase P' or alternatively to create $P' < 1$; this was not succesful because of lack of power. Apparently in this experiment impurity surface relaxation was not sufficiently suppressed, since the spontaneously acquired nuclear polarization P is nowhere near the spectacularly high values of Sprik et al.[20] : $P_{max} = 99.8\,\%$ corresponding to $P' = 1000$. A thicker ^{4}He film was tried but this did not allow the sample cell to cool much below 300 mK. It then becomes very difficult to work in a wide temperature range, because on the other hand a field $B = 5.7$ T offers insufficient magnetic compression of the sample. At $T > 300$ mK the density distribution (eq. (1.7)) extends into the thermal platform region, which may not be free from magnetic impurities. H atoms can diffuse in a reasonable time to this point, where they quickly relax their nuclear spins. These measurements were terminated by technical problems. We intend to improve them in the future with improved apparatus.

Returning to the K_{aa}/K_{ab} determination : it is also possible to fit the rate equations (4.21) directly to the observed a(t) and b(t) once a density scale factor is known from the pressure. A computer program was available that numerically solves the two equations simultaneously, taking into account 1st order relaxation G_s^{ie}, 2nd order relaxation G_V and G_s^e and 2nd order recombination with $K_{aa}^e \neq K_{ab}^e$. All parameters had to be varied by hand (the intrinsic relaxation rates are known in principle, but the effective values are still very sensitive for the exact temperature). It was found that e.g. the run of fig. 4.17B could be described equally (un)satisfactorily with K_{aa}/K_{ab} ranging from 3 - 5. The dynamic range in n_b/n_a was insufficient. However, the method in principle is very powerful when more frequently sampled and more accurate ESR data is available. As compared to fitting the total density curve alone, much more information is available for these multi-parameter non-linear fits.

Using our techniques it is possible to measure directly the gas temperature and compare it to the cell wall temperature, which could differ due to the Kapitza resistance. From the simultaneous measurement of pressure p and (relative) density n by ESR, we can check whether T is constant by application of the ideal gas law. This is not a trivial point, since during the decay of a hydrogen sample the energy of recombination is released at the surface and transferred to the gas and the helium film. The gas could be warmer than the cell walls because of two Kapitza resistances in series (gas-liquid, liquid-copper). Moreover the H↓ gas temperature may be gradually changing as the number of recombinations decreases. This would have serious consequences for the analysis of all the decay curves that have been used previously to determine rate constants and adsorption energies, and especially for the method of determination of K_{aa}/K_{ab} of Sprik et al.[20] because these all rely on the conversion of pressure into density. In fig. 4.18 the proportionality of pressure and density is demonstrated. Heating effects would be $\propto n^2$ and would show up as a systematic upward curvature at the higher end of the line. This is not observed, at least for densities up to $\sim 6\times10^{15}/\mathrm{cm}^3$. This is a little bit lower than the highest density used in ref. 20 for K_{aa}/K_{ab} determination. More information of this kind for higher densities and lower temperatures is obviously needed. Note that the ESR signals are not measured relative to the incident power, so that slow drifts in power are important. These are responsible for the slight deviations from a straight line. Fig. 4.18 is composed of data from two runs taken immediately after each other. Other runs, taken some hours later, also give straight lines but of different slope. (For the determination of P′ in fig. 4.17 such slow drift is unimportant.)

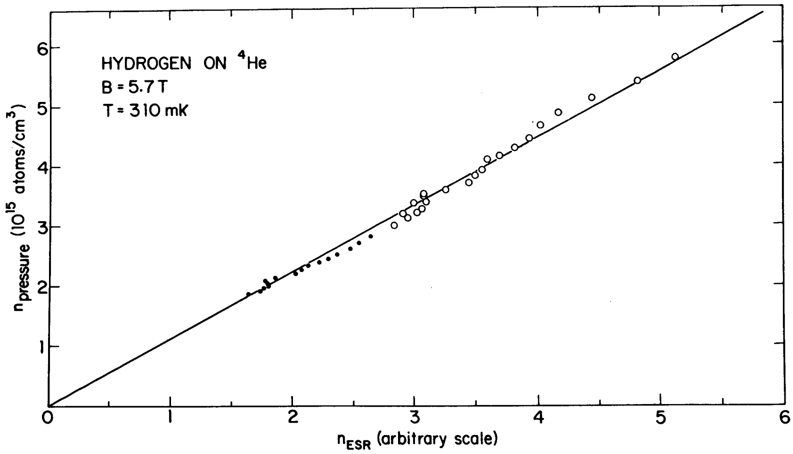

Fig. 4.18. A linear relation between pressure and density, proving that the temperature of the H↓ gas is constant, and in equilibrium with the cell walls.

No attempt has been made yet to employ the quadrupole coils to generate a field gradient to measure the density profile as described in section 4.2. Typically $\frac{dB}{dz} = 0.05$ T/cm would be used over 8 cm length, so the line would be 0.4 T wide ! Such a large gradient is needed to produce a reasonable change in the density at e.g. $T = 0.3$ K according to eq. (1.7). This implies that the height of the line would be a factor ~ 1000 lower than for the $1 : 10^5$ homogeneous magnet. No proper frequency or other modulation technique was available to measure such a weak, broad line at the presently current H↓ densities.

4.6. Suggestions for improvements

As suggestions for further improvements to refine the measurements described in this chapter we would like to mention : a better design of sweep- and switch coils (homogeneous over a larger range) or a better system to sweep the main field, for example a system with flux coupling by a superconducting transformer[31]. Additionally a smaller decay rate for the persistent current in the main coil by improving the wire joints would be useful. The signal to noise ratio can presumably be improved by making a heavier thermal link from the FIR bolometer mounting plate to the Cold Plate of the dilution refrigerator, so that the bolometer operates at a lower temperature with increased responsivity. More microwave power in the cell, with the same source, could be obtained by using a better light pipe or waveguide system, separate from the H fill line.

References of chapter 4

1. G.H. van Yperen, I.F. Silvera, J.T.M. Walraven, J. Berkhout, and J.G. Brisson, Phys. Rev. Lett. 50, 53 (1983).
2. B.W. Statt and A.J. Berlinsky, Phys. Rev. Lett. 45, 2105 (1980).
3. J.T.M. Walraven and I.F. Silvera, Phys. Rev. Lett. 44, 168 (1980).
4. V.V. Goldman, I.F. Silvera and A.J. Leggett, Phys. Rev. B24, 2870 (1981).
5. T. Niinikoski and L. Dick, private communication.
6. R.M. Kulsrud, H.P. Furth, and E.J. Valeo, and M. Goldhaber, Phys. Rev. Lett. 49, 1248 (1982); Physics Today, august 1982, p. 17.
7. I.F. Silvera, Physica B+C 109 & 110, 1499 (1982).
8. W.N. Hardy, M. Morrow, R. Jochemsen and A.J. Berlinsky, Physica B+C 109 & 110, 1964 (1982).
9. B. Yurke, J.S. Denker, B.R. Johnson, N. Bigelow, L.P. Lévy, D.M. Lee, and J.H. Freed, Phys. Rev. Lett. 50, 1137 (1983).
10. R. Mayer, A. Ridner, and G. Seidel, Physica 108 B+C, 937 (1981).
11. B.W. Statt and W.N. Hardy, private communication.
12. B. Yurke, D. Igner, E. Smith, B. Johnson, J. Denker, C. Hammel, D. Lee and J.H. Freed, J. Phys. (Paris) 41, C7-177 (1980). A binary collision model (BCM) must be used; $(T_{2,ESR}^{-1})^{BCM} \propto n\sqrt{T}$, whereas they use a diffusion model: $(T_{2,ESR}^{-1})^{Diff} \propto n^2/\sqrt{T}$. For $n \lesssim 6 \times 10^{20}\ T\ [K^{-1}cm^{-3}]$ the binary collision rate is dominant, but still the effect is negligible compared to radiation damping: $(T_{2,ESR}^{-1})^{BCM} \approx 10^{-3}\ \tau_{RD}^{-1}$.
13. D.A. Huse and E.D. Siggia, J. Low Temp. Phys. 46, 137 (1982).
14. R.W. Cline, D.A. Smith, T.J. Greytak, and D. Kleppner, Phys. Rev. Lett. 45, 2117 (1980).
15. I.F. Silvera and J.T.M. Walraven, Phys. Rev. Lett. 44, 164 (1980).
16. I.F. Silvera, Rev. Sci. Instrum. 41, 1513 (1970).
17. M. Deutsch, Cryogenics 19, 273 (1979).
18. M. Suomi, A.C. Anderson, B. Holstrom, Physica 38, 67 (1968).
19. A.P.M. Matthey, J.T.M. Walraven, and I.F. Silvera, Phys. Rev. Lett. 46, 668 (1981).

20. R. Sprik, J.T.M. Walraven, G.H. van Yperen, and I.F. Silvera, Phys. Rev. Lett. 49, 153 (1982).
21. S. Saito and T. Sato, Rev. Sci. Instr. 46, 1226 (1975).
22. S. Kobayasi, M. Shinohara, and K. Ono, Cryogenics 16, 597 (1976).
23. J.G. Baker, in *Spectroscopic Techniques for far infra-red, submillimetre and millimetre waves*, ed. D.H. Martin (North Holland Publishing Company, Amsterdam 1967).
24. R. Ulrich, K.F. Renk and L. Genzel, IEEE Transactions on Microwave Theory and Technique MTT 11, 363 (1963).
25. R. Ulrich, Infrared Physics 7, 37 (1967).
26. E.A.M. Baker and B. Walker, J. Phys. E. 15, 25 (1982).
27. R.C. Ohlmann, P.L. Richards and M. Tinkham, Journal of the Optical Society of America, vol. 48, 531 (1958).
28. N.S. Nishioka, P.L. Richards and D.P. Woody, Applied Optics 17, 1562 (1978).
29. H.D. Drew and A.J. Sievers, Applied Optics 8, 2067 (1969). We thank Dr. A.J. Sievers for kindly supplying us with this material.
30. R.W. Cline, T.J. Greytak, and D. Kleppner, Phys. Rev. Lett. 47, 1195 (1981).
31. G.F. Spencer, P.W. Alexander, and G.G. Ihas, Cryogenics 22, 167 (1982).

SUMMARY

This thesis deals with some experiments in (gaseous) spin-polarized atomic hydrogen (H↓), a field which only very recently has been made accessible to experiments. One uses the expression 'stabilized' atomic hydrogen, meaning that by choosing suitable conditions one can suppress the tendency of atoms to recombine into H_2 molecules, such that the lifetime of the atomic state is extended by many orders of magnitude. However the suppression of recombination is not perfect. Research is focused at the study of processes that determine the decay rate of H↓ samples, with the ultimate goal of preparing samples of sufficiently high density and at low enough temperature to observe experimentally the behavior of the (degenerate) quantum gas. ESR (Electron Spin Resonance) appears to be a very suitable measurement technique to study the properties of H↓. This work describes the introduction of ESR as detection technique, and the first results of an experiment in H↓ using this technique.

The thesis is divided in four chapters. Chapter 1 supplies some information on the theoretical aspects that motivate the research on atomic hydrogen: H↓ is presented as an extreme example of a weakly interacting quantum fluid, and it is compared to the known quantum liquid helium (^{4}He). Also the experimental techniques used to stabilize atomic hydrogen are briefly mentioned here. A short historical review is given which pictures the progress which has been made during only a few years in the understanding of the decay processes and in the achievement of still higher sample densities. This chapter serves to place the material discussed in the next three chapters in a framework.

Chapter 2 gives an overview of calculations of the nuclear spin relaxation time (T_1) in H↓. Electron-spin polarized hydrogen consists of atoms in two hyperfine states (a and b), of which one (a) has a small a admixture of the 'wrong' electronic spin; as a consequence atoms in this state can recombine relatively fast. Atoms in state b are much more stable among themselves. The transition between these states (b → a) is a nuclear spin relaxation process; the relaxation time can be very long (hours) in a dilute gas and as a consequence it can determine the

lifetime of a H↓ sample. This chapter discusses the existing literature concerning the calculation of this very important relaxation time, along with a few extensions, and with emphasis on the relatively simple but remarkably accurate so called 'excluded volume' model. An important conclusion is that by comparison of the theory with existing experimental data on the relaxation rate, the very first, and also very elegant, experimental proof has been given of the fact that hydrogen atoms behave as indistinguishable particles, in this case as (composite) bosons.

Chapter 3 presents an extensive description of an experiment performed to find out whether hydrogen atoms at very low temperatures (down to ~80 mK) will condense on surfaces covered by a film composed of a mixture of ^{3}He and ^{4}He. This was shown to occur indeed, and from the temperature dependence of the effective surface recombination rate the adsorption energy of H↓ on these surfaces could be determined. Also described are the first attempts to demonstrate the influence of a long nuclear spin relaxation time (T_1) on the decay of a sample, (initially) with a negative result. This can be explained by rapid relaxation caused by magnetic impurities; large values for T_1 have been confirmed indeed in later experiments.

Chapter 4 is an extensive description of ESR as measuring technique. For this purpose a special hybrid spectrometer was built, by combining high resolution microwave techniques with the advantages of broadband quasi-optical techniques known from far infrared spectroscopy. By determining the relative intensity of two transitions in the ESR spectrum one can measure the population of the two hyperfine states (a and b) as a function of time during the decay. This offered for the first time a direct and very convincing demonstration of the fact that the so called doubly polarized state (all atoms in state b) is stable on a timescale set by the b → a nuclear spin relaxation, and that this doubly polarized state is created spontaneously by recombination during the first phase in the decay of a sample consisting of atoms in both the a- and b-state.

SAMENVATTING

Dit proefschrift behandelt enkele experimenten met (gasvormig) spin-gepolariseerd atomair waterstof (H↓), een materie die pas zeer onlangs experimenteel toegankelijk is gemaakt. Men spreekt van 'gestabiliseerd' atomair waterstof, waarmee bedoeld wordt dat door het kiezen van geschikte condities de neiging tot H_2 molecuulvorming onderdrukt kan worden zodat de levensduur van de atomaire toestand met vele orden van grootte kan worden verlengd; echter de onderdrukking van recombinatie is niet volkomen. Het onderzoek richt zich op de bestudering van de aard van de processen die de vervalsnelheid van een H↓ sample bepalen, met als uiteindelijk streven de realisering van samples van voldoend hoge dichtheid en bij voldoend lage temperatuur om het gedrag van het (gedegenereerd) quantum gas experimenteel te kunnen bestuderen. ESR (Electron Spin Resonantie) blijkt een buitengewoon geschikte meettechniek ter bestudering van H↓. Dit werk beschrijft de introductie van ESR als detectie techniek en de eerste resultaten van een experiment aan H↓ met deze techniek.

Het proefschrift is ingedeeld in vier hoofdstukken. In hoofdstuk 1 wordt enige informatie verschaft over de theoretische aspecten die het onderzoek aan atomaire waterstof motiveren: H↓ wordt gepresenteerd als extreem voorbeeld van een zwak wisselwerkende 'quantum fluid', en wordt vergeleken met de reeds bekende quantum vloeistof helium (^{4}He). Tevens wordt kort ingegaan op de experimentele technieken die gebruikt worden om atomair waterstof te stabiliseren. Er wordt een kort historisch overzicht gegeven van de vooruitgang die in enkele jaren tijds is geboekt in het begrijpen van de vervalsprocessen en het opvoeren van de maximale sampledichtheden, waardoor de materie behandeld in de volgende drie hoofdstukken in een kader wordt geplaatst.

Hoofdstuk 2 geeft een overzicht van berekeningen van de kernspin relaxatietijd (T_1) in H↓. Electron-spin gepolariseerd waterstof bestaat uit atomen in twee hyperfijntoestanden (a en b); één van die twee toestanden (a) heeft een kleine bijmenging van de 'verkeerde' electron spin, zodat atomen in die toestand relatief snel kunnen recombineren. Atomen in toestand b zijn onderling veel stabieler. De overgang tussen deze twee toestanden (b → a) is een kernspin relaxatie proces; de relaxatietijd kan in een zeer ijl gas lang zijn (uren) en derhalve de levensduur van een H↓ sample bepalen. Dit hoofdstuk geeft een bespreking van de bestaande literatuur over berekening van deze zeer belangrijke relaxatietijd, aangevuld met enkele uitbreidingen, en met het accent op het betrekkelijk simpele maar opmerkelijk nauwkeurige zgn. 'excluded volume' model. Een belangrijke conclusie is dat door vergelijking van theorie en reeds bestaande metingen van de relaxatie snelheid het eerste, en tevens zeer elegante, experimentele bewijs is geleverd dat watersofatomen zich als ononderscheidbare deeltjes, in dit geval als (samengestelde) bosonen gedragen.

Hoofdstuk 3 geeft een uitvoerige beschrijving van een experiment waarin is nagegaan of waterstofatomen bij zeer lage temperatuur (tot ca. 80 mK) uitcondenseren op oppervlaktes gevormd door een film bestaande uit een mengsel van ^{3}He en ^{4}He. Dit blijkt inderdaad het geval te zijn, en uit de temperatuurafhankelijkheid van de effectieve oppervlakte-recombinatie snelheid kon de adsorptie energie van H↓ op deze oppervlakken bepaald worden. Tevens worden beschreven de eerste pogingen om de invloed van een lange kernspin relaxatietijd (T_1) op het verval van een sample aan te tonen, met (aanvankelijk) negatief resultaat. Dit kan verklaard worden door snelle relaxatie door magnetische onzuiverheden; in latere experimenten is de lange T_1 wel bevestigd.

Hoofdstuk 4 beschrijft uitvoerig de introductie van ESR als meettechniek. Voor dit doel is een speciale hybride spectrometer gebouwd, die hoge resolutie microgolftechnieken combineert met de voordelen van breedband quasi-optische technieken bekend uit de ver infrarood spectroscopie. Door bepaling van de relatieve intensiteit van twee overgangen in het ESR spectrum kan de bezetting van de twee hyperfijntoestanden (a en b) als functie van de tijd gedurende het verval gemeten worden. Hiermee is voor het eerst direct en op overtuigende manier aangetoond dat de zgn. dubbelgepolariseerde toestand (alle atomen in toestand b) stabiel is op een tijdschaal die bepaald wordt door b → a kernspin relaxatie, en dat deze dubbelgepolariseerde toestand spontaan ontstaat door recombinatie tijdens de eerste fase van verval van een sample bestaande uit atomen in zowel de a- als b-toestand.

NAWOORD

Bij het afsluiten van dit proefschrift wil ik graag allen bedanken die aan de uitvoering van dit onderzoek een bijdrage hebben geleverd.

In de eerste plaats denk ik hierbij aan mijn promotor, Prof. Ike Silvera. Door zijn buitengewoon inspirerende optreden en zijn zeer intensieve begeleiding zijn mogelijkheden geopend waarvan ik het bestaan niet had kunnen vermoeden. Een groot deel van mijn wetenschappelijke vorming heb ik aan hem te danken.

Met genoegen zal ik terugdenken aan de vele leerzame adviezen op het gebied van experimentele fysica die ik heb gekregen van Jook Walraven, en de intensieve samenwerking bij latere experimenten. Voor het theoretisch gedeelte van mijn proefschrift heb ik dankbaar gebruik gemaakt van de kennis van Ad Lagendijk, die steeds bereid was om voor mij onbegrijpelijke details én hoofdlijnen uit te leggen. Ook denk ik daarbij aan Victor Goldman.

Jaap Berkhout wil ik bedanken voor zijn continue stroom van bijdragen aan het slagen van de experimenten. De grondige manier waarop hij zich in álle aspecten van het onderzoek heeft gestort was mij een waar genoegen. Ook Tom Kerkhoven en John Brisson wil ik danken voor hun aandeel in de experimenten.

Samen met mijn collega-promovendi in de atomaire waterstof Stijn Mattheij en Rudolf Sprik, en Kauko Salonen, is dan ongeveer het beeld compleet van de groep mensen waarmee ik in telkens wisselende samenstelling op een zeer plezierige en vruchtbare manier heb mogen samenwerken.

Otto Höpfner heeft het overgrote deel van de technische realisering van de experimenten verzorgd. Zijn vakkundig en betrouwbaar instrumentmakerswerk, en de zeer flexibele manier waarop hij de vaak moeilijke projecten heeft aangepakt waren van onschatbare waarde.

Daarnaast wil ik nog bedanken Ruud Scheltema en de vele andere instrumentmakers die in de loop der tijd technische bijdragen hebben geleverd. Bert Zwart zorgde voor snelle hulp bij vacuum problemen en Nico Jonker en Herman Pothoven zorgden voor een onafgebroken stroom van vloeibare helium en stikstof. Ton Riemersma en Hugo Schlatter zorgden in een pijlsnelle aktie voor de foto's in dit proefschrift.

Alle medewerkers tot zover niet met name genoemd wil ik bedanken voor de vele direkte en indirekte bijdragen, en voor de plezierige sfeer op het Nat Lab.

Henk Dijkerman uit Utrecht wil ik bedanken voor het uitlenen van microgolf apparatuur toen onze eigen apparatuur het liet afweten, en Thijs de Graauw van ESTEC voor daadwerkelijke hulp op het gebied van frequentie-vermenigvuldigingstechniek.

Ik denk ook aan mijn ouders, voor de stimulering van mijn wetenschappelijke interesse, en voor hulp bij het vervaardigen van het manuscript.

Tenslotte wil ik Rita bedanken voor haar buitengewoon belangrijke steun en liefde in tijden van voorspoed en van teleurstellingen, en voor de vele opofferingen in de huiselijke sfeer.